Michele Caruso

Design of Fully-Integrated High-Resolution Radars in CMOS and BiCMOS Technologies

Versione modificata della tesi di dottorato depositata a norma di legge

Questa versione non include la sezione riguardante il design di building blocks per Phased Array Radar

2016

Università degli Studi di Padova
Dipartimento di Ingegneria dell'Informazione

Design of Fully-Integrated High-Resolution Radars in CMOS and BiCMOS Technologies

Tesi di: Michele Caruso

Scuola di Dottorato in Ingegneria dell'Informazione
Indirizzo in Scienza e Tecnologia dell'Informazione
Ciclo XXVI

Supervisore:
Prof. Andrea Neviani

Direttore della Scuola:
Prof. Matteo Bertocco
Coordinatore di Indirizzo:
Prof. Carlo Ferrari

To my family

"It can't rain all the time"

- The Crow

ACKNOWLEDGEMENTS

I would like to begin this thesis acknowledging some people that sustained me during the PhD. First of all, I would like to thank Prof. Andrea Bevilacqua, one of my two supervisors. He guided me during my experience at the university and always inspired me with his endless knowledge. Then I would like to thank my second supervisor, Prof. Andrea Neviani, for his patience, attention to details, sapience and kindness. I could never imagine two supervisors better than them.
I spent six months at Infineon Technologies, in the design center in Villach. Here I would like to thank Mr. Marc Tiebout for his competence, for his suggestions and for every discussions we had together (technical or not). It has been a pleasure to work with you. In the same context, I would like to thank Marc's colleagues: Franz Dielacher, Koen Mertens, Stefano Lenuzza and many others. I also would like to thank Infineon Technologies for letting me work in the design center in Villach.
Then, I would like to acknowledge Matteo Bassi for being a great friend and a perfect fellow. We worked for more than two years together and we had a lot of fun. Thanks for the great time we spent in the U.S. and for showing me a lot of new stuff. I'll miss you, I know...but I hope we will have other opportunities to work together again.
Within the ICARUS lab, I would like to thank Fabio Padovan for being a good friend and a good fellow. We also spent a lot of time together (both in Padova and in Villach) and it was a pleasure to meet him during my PhD.
Among the girls I know, I would like to thank Valentina Giliberto for her kindness and simplicity. She is one of my best friends, and I give her my best wishes for her new life.
Outside the university context, I want to acknowledge my parents for supporting me in everything I do, even when they do not fully agree with me. I'm lucky to have you two as parents. Then I would like to thank my sister, Patrick and, especially, my lovely niece Giulia.
Last, but not least, I would like to thank Vanessa for loving me and supporting me in the last eight years. We had a great time together, and I am pleased to spend with you the rest of my life...and remember: *"It can't rain all the time"*.

Padova, 31st December 2013 M. C.

ABSTRACT

The RADAR, acronym that stands for RAdio Detection And Ranging, is a device that uses electromagnetic waves to detect the presence and the distance of an illuminated target. The idea of such a system was presented in the early 1900s to determine the presence of ships. Later on, with the approach of World War II, the radar gained the interest of the army who decided to use it for defense purposes, in order to detect the presence, the distance and the speed of ships, planes and even tanks.

Nowadays, the use of similar systems is extended outside the military area. Common applications span from weather surveillance to Earth composition mapping and from flight control to vehicle speed monitoring. Moreover, the introduction of new ultrawideband (UWB) technologies makes it possible to perform radar imaging which can be successfully used in the automotive [24, 31] or medical field [11].

The existence of a plenty of known applications is the reason behind the choice of the topic of this thesis, which is the design of fully-integrated high-resolution radars.

The first part of this work gives a brief introduction on high resolution radars and describes its working principle in a mathematical way. Then it gives a comparison between the existing radar types and motivates the choice of an integrated solution instead of a discrete one.

The second part concerns the analysis and design of two CMOS high-resolution radar prototypes tailored for the early detection of the breast cancer. This part begins with an explanation of the motivations behind this project. Then it gives a thorough system analysis which indicates the best radar architecture in presence of impairments and dictates all the electrical system specifications. Afterwards, it describes in depth each block of the transceivers with particular emphasis on the local oscillator (LO) generation system which is the most critical block of the designs. Finally, the last section of this part presents the measurement results. In particular, it shows that the designed radar operates over 3 octaves from 2 to 16GHz, has a conversion gain of 36dB, a flicker-noise-corner of 30Hz and a dynamic range of 107dB. These characteristics turn into a resolution of 3mm inside the body, more than enough to detect even the smallest tumor [30].

SOMMARIO

Il RADAR, acronimo per RAdio Detection And Ranging, é uno strumento che sfrutta le proprietá elettromagnetiche della materia per rilevare l'eventuale presenza e distanza di oggetti non conosciuti. L'idea di un simile dispositivo fu presentata per la prima volta nei primi anni del 1900 per determinare la presenza di navi in avvicinamento. Solo dopo qualche anno, con l'avvicinarsi della seconda guerra mondiale, cominció la vera e propria ricerca e sperimentazione. Inizialmente, infatti, il radar venne utilizzato prettamente in ambito militare per rilevare la presenza, la distanza e la velocitá di navi, aerei e carri armati nemici.

Ai giorni nostri, invece, il concetto di radar viene esteso ben al di fuori dell'ambito militare. Infatti é possibile trovare soluzioni per applicazioni che spaziano dalla mappatura del terreno alla sorveglianza delle condizioni metereologiche e dal controllo del traffico aereo all'individuazione della velocitá dei veicoli. Inoltre, l'introduzione di nuove tecnologie a larga banda (UWB), rende possibile la generazione di immagini radar le quali possono essere sfruttate con successo sia in ambito medico [11] che automotive [24, 31].

L'esistenza di un'infinitá di applicazioni conosciute legata all'estrema versatilitá dei radar é la motivazione che mi ha spinto a focalizzare il mio lavoro sull'analisi e la progettazione di radar integrati ad alta risoluzione.

La prima parte di questa tesi dá una breve introduzione circa i radar ad alta risoluzione e ne descrive il principio di funzionamento ricavandone le principali equazioni. Essa mette inoltre a confronto le varie tipologie di radar motivando la scelta di un radar integrato rispetto ad una soluzione a componenti discreti.

La seconda parte, invece, tratta l'analisi e la progettazione di due prototipi di radar CMOS ad alta risoluzione destinati alla rilevazione preventiva dei tumori al seno. Dopo una breve spiegazione delle motivazioni che stanno alla base di questo progetto, viene effettuata un'accurata analisi di sistema la quale permette di scegliere l'architettura meno sensibile alle non idealitá del ricevitore. Successivamente viene data una descrizione dettagliata di ogni singolo circuito che constituisce il ricetrasmettitore, con particolare enfasi alla generazione delle frequenze la quale costituisce il blocco piú critico dell'intero sistema. Infine, l'ultima sezione di questa seconda parte, presenta i risultati di misura sia per quanto riguarda la caratterizzazione elettrica che per quanto riguarda gli esperimenti di imaging. In particolare, sará possibile notare che il radar opera su una banda di 3 ottave da 2 a 16GHz, ha un guadagno di conversione di 36 dB, una flicker-noise-corner di 30Hz ed un range dinamico di 107dB. Tali caratteristiche si traducono in una risoluzione di 3mm nel corpo umano, piú che sufficiente per rilevare anche il piú piccolo tumore [30].

CONTENTS

LIST OF FIGURES

LIST OF TABLES

Part I

RADAR OVERVIEW

1

INTRODUCTION TO RADAR SYSTEMS

The RADAR, acronym that stands for RAdio Detection And Ranging, is a particular type of systems that is able to detect the presence of objects. In principle, it was largely developed to satisfy the needs of the military for surveillance and weapon control [53]. Nowadays, however, its use is extended beyond the military context. Applications span from the safe travel of aircraft, ships and spacecraft to the weather surveillance. Other applications include medical imaging, car security, crash prevention and many others.
This chapter briefly introduces the radar system. It describes its principle of operation and gives a short insight on the equations that underlie its correct operation. Finally the last section gives a description of the major different types of radars.

1.1 DESCRIPTION AND WORKING PRINCIPLE

The working principle of a Radar system is relatively simple, even though its realization is not, in general. It consists of radiating electromagnetic energy and detecting the backscatter from reflecting objects (targets). From the received signal, informations about the target are retrieved. The range, i.e. the distance between the generating antenna and the target, is obtained from the time-of-flight and the wave propagation velocity in the medium. The angular location, instead, is retrieved by means of a directional antenna while the target velocity is retrieved due to the Doppler effect caused by the relative motion between the target and the radar antenna.
The resolution is one of the most important parameters of a radar system. The resolution can be obtained in range, in angle or both. The range resolution, usually called slant-range resolution, is the resolution along the direction of the wave propagation and is directly related to the bandwidth of the transmitted pulse. The larger the bandwidth, the higher the resolution. The angular resolution is related to the electrical dimension of the antenna. The larger the antenna, the higher the resolution. However, a high angular resolution can be obtained without using large antennas by means of the Synthetic Aperture approach (Sec. 1.6.3).
A simple block diagram of a conventional radar is shown in Fig. 1. The radar signal, which is usually a short pulse or a repetition of short pulses, is amplified by a power amplifier and transmitted by means of an antenna. The power amplifier must feature

large bandwidth and flat gain along with a high efficiency. The output power is determined by the the maximum desired range and by the receiver sensitivity. Short-range applications usually use integrated power amplifiers whose output a power in the order of milliwatts (car radar examples are [18, 63]). There are, however, applications that demand a larger output power, even in the order of kiloWatts, or more (long-range applications like weather surveillance, flight control, etc.).
The duplexer allows to share a single antenna for both receiver and transmitter side. It must show a low insertion loss and a high isolation between TX output and RX input. This allows to protect the LNA input from the large amount of transmitted power and avoids the saturation of the receiver. The duplexer is generally a circulator or a hybrid coupler. Nevertheless, it may be replaced by a simple switch in applications where TX and RX don't work in the same time slot.
The task of the antenna is to irradiate the output power of the PA and receive the reflected energy from the target. In principle it was directive and mechanically steered, hence it concentrated the power in the desired direction into a narrow beam. Recently, the same result is obtained by means of a phased array architecture without the need of mechanically moving the antenna.
The receiver captures and elaborates the backscattered signal. It is composed by a low noise amplifier and a downconversion stage. Not to impair the received signal with the noise, the LNA must feature a high gain with a low noise figure. In addition, it must show a well defined input impedance in order to match the antenna. The downconversion stage provides a translation of the received spectrum toward lower frequencies. This makes the analog-to-digital conversion and the post processing operation simpler. Depending on the system characteristics and specifications, the downconverted frequency may be zero (direct conversion architecture) or an intermediate frequency IF (this is the case of the super-heterodyne architecture). Finally, a baseband amplifier adapts the signal to the input range of the ADC while providing anti-alias filtering.

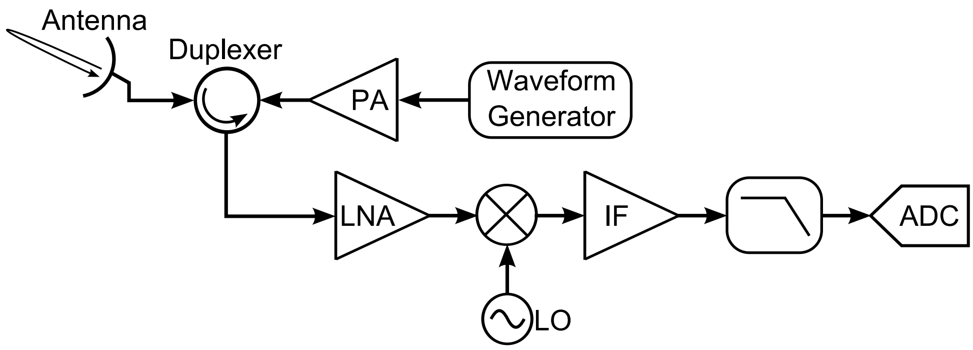

Figure 1: Simple block diagram of a conventional radar system.

1.2 IMPORTANCE OF AN INTEGRATED SOLUTION

During the World War II, the radar development increased and radars were used for defence purposes, to detect the presence, distance and speed of ships, planes and tanks. They were also used for missile guidance and tracking. Each of these applications, therefore, was related with long-range detection. As a consequence the required output power had to be high, even in the order of kilowatt. This, together with the relatively old employed technology, made the system heavy, bulky and expensive. However, it was not an issue since, usually, a single transceiver with a large antenna was mounted on ships or control towers. Later on, radar applications have been extended outside the military area, for weather surveillance, flight control, astronomy, etc. Huge parabolic antennas were used to increase the antenna gain and directivity and, sometimes, they were mounted on mobile supports that increased even more the total dimension. As a consequence, even in this case, the relatively large radar active circuit's dimension was not an issue.

Nowadays, the number of different radar applications is getting larger. New short-range applications are emerging, for example in the automotive, industrial or biomedical field. Unlike standard long-range applications, here the dimension of the radar circuit is fundamental. As an example, in a single car one may found several different radars, each used for different functions: crash prevention, adaptive cruise control, parking assistance, blind-spot detection, etc. A complete fully-integrated radar allows to reduce the system physical dimension and the implementation cost. The absence of external components, moreover, increases the robustness of the system as well as its reliability. The need of an integrated solution becomes evident in those systems based on the phased array architecture. Here, the total system is composed by N transceivers connected to an antenna array. Since the antennas spacing is related to the wavelength of the transmitted signal, a spacing of few centimeters is needed if the frequency of the signal is in the order of few GHz. Here, the use of integrated radars is mandatory to avoid long RF interconnections between antennas and radar circuits. However, short-range radar applications are not the only which can benefit from the technology scaling. Recently, in fact, fully integrated long-range applications have been presented [3].

To conclude, the availability of fully-integrated radars is seen as a need in today's applications. An integrated circuit allows to reduce both system dimension and cost while increasing the overall performances.

1.3 RADAR EQUATION

As explored in the introduction, the radar was invented for the detection and ranging of unknown targets. Modern high-resolution radars provide additional features like ground mapping, target recognition and, more recently, imaging capabilities. Nonetheless, the basic equation that describes the received backscatter power as a function of system parameters is always the same.

Consider Fig. 2 which shows the radar operating concept. The transmitted and received signals are in general considered to be generated and received from two different antennas placed in two different positions. A free-space propagation is considered, hence no multipath or reflection occurs (except the reflection introduced by the target). Additionally, we assume that the target is small enough to be uniformly illuminated by the transmitted beamwidth and its dimension along the direction of the wave propagation is small as compared with the pulse duration. The power density incident to a target at range R_t from the transmitting antenna is

$$s_t = \frac{P_t G_t}{4\pi R_t^2} \left[\frac{W}{m^2}\right], \tag{1}$$

where P_t is the transmitted power and G_t is the transmitting antenna gain. At this point, the target scatters the incident power in all directions, including back to the transmitting and receiving antennas. The power density that reach the receiver is

$$s_r = \frac{P_t G_t G_r \lambda^2 \sigma}{(4\pi)^3 R_t^2 R_r^2} \left[\frac{W}{m^2}\right], \tag{2}$$

where G_r is the receiving antenna gain, R_r is the target range with respect to the receiver, λ is the wavelength and σ is the radar cross section (RCS) of the target. This term, that will be better explained in Sec. 1.4, determines the amount of incident power that the target scatters back to the antenna. In a monostatic radar, where the antenna is the same for TX and RX, $G_t = G_r = G$ and $R_t = R_r = R$, thus

$$s_r = \frac{P_t G^2 \lambda^2 \sigma}{(4\pi)^3 R^4} \left[\frac{W}{m^2}\right]. \tag{3}$$

The ability of the radar to detect the received backscatter, and thus the target, depends on the receiver sensitivity. The sensitivity itself depends on the noise figure of the system, on the bandwidth of the received signal and on the needed SNR that allows a correct detection. Hence, a common form for the range equation written as a function of the input SNR of the system is

$$R = \left[\frac{P_t G^2 \lambda^2 \sigma}{(4\pi)^3 k T_e \beta (S/N)_{in} L}\right]^{\frac{1}{4}}, \tag{4}$$

where the quantity kT_e is the noise power density at the antenna terminals, β is the signal bandwidth and L is a factor that takes into account all the radar losses.

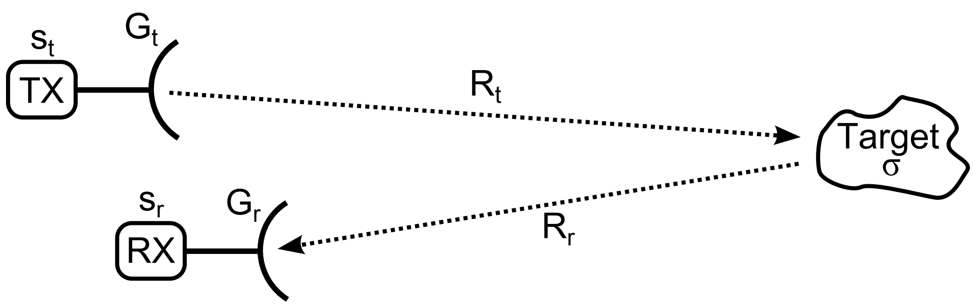

Figure 2: Derivation of the radar equation.

1.4 RADAR CROSS SECTION

A radar is able to detect or identify an unknown object because it is a source of backscattered signal. A quantification of this echo is, therefore, mandatory for a correct design of the system. For this purpose, the target is described as an effective area called radar cross section (RCS). To better understand its meaning, consider Fig. 3 that shows a monostatic radar placed at the center of an imaginary sphere whose surface contains the target. The target RCS is the cross-sectional area on the sphere's surface which isotropically re-radiates toward the receiver the same amount of power that would have radiated the target [62]

$$\sigma = \frac{\mathit{Equivalent\ isotropically\ scattered\ power}}{\mathit{Incident\ power\ density}} = \frac{4\pi R^2 s_e}{s_i}, \tag{5}$$

where R is the sphere radius ($R >> \lambda$), s_i is the incident power density and s_e is the echo power density at the radar. Notice that the radar cross section must be calculated in the far field. This makes the RCS independent on the target range. Another well used definition of the RCS is

$$\sigma = \lim_{R \to \infty} 4\pi R^2 \frac{|E_e|^2}{|E_i|^2}. \tag{6}$$

that inherently defines the RCS in the far field. Additionally, since the electric field $|E_e|$ at the receiver antenna decays with R, Eq. 6 shows the independence of the radar cross section from the target range.
The target RCS is often measured relative to that of a conducting sphere. The radar cross section of a sphere with radius a is equal to its cross-sectional area πa^2. Unlike the echo of the sphere, however, which is independent of the viewing angle, the echoes of more complex targets vary significantly with the orientation.

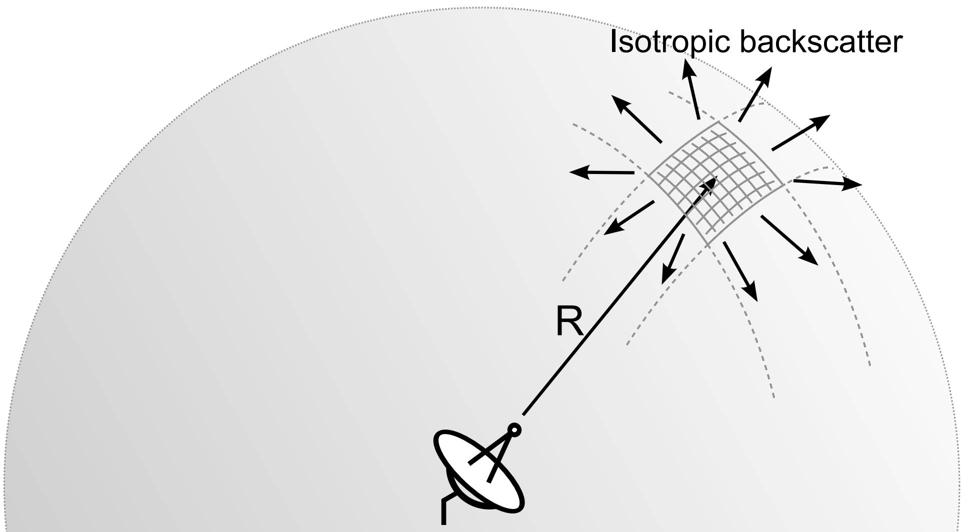

Figure 3: Explanation of the radar cross section concept.

1.5 RESOLUTION

The definition of the radar resolution is not unique. We can refer to the range resolution or angular resolution. Leveraging the Doppler effect, the radar allows moreover to determine the speed of moving targets. Thus, the Doppler resolution is another measure of the system resolution.
The radar range resolution, called slant-range resolution, can be defined as the ability to resolve point targets that are separated in range from the radar. An intuitive way to obtain the range resolution is explained as follows. Consider two targets located at ranges R_1 and R_2, corresponding to time delays t_1 and t_2, respectively (Fig. 4). At first,

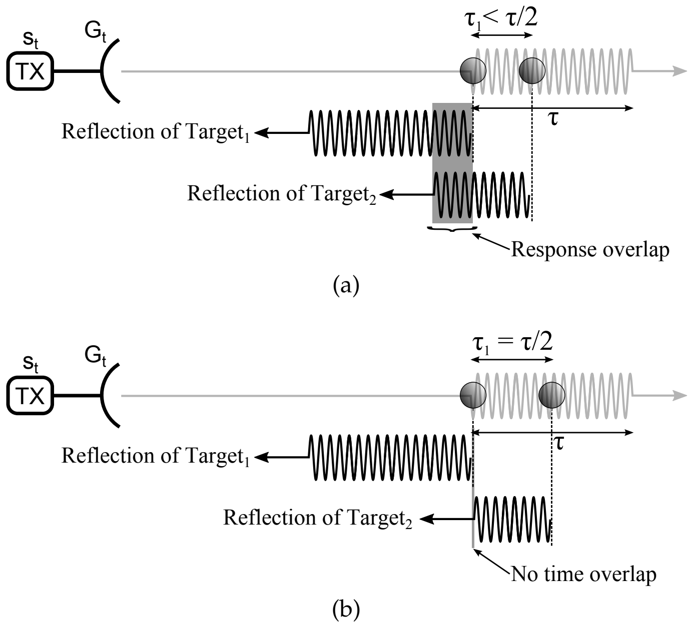

Figure 4: Radar range resolution. Overlap between backscattered signals when the target are placed too close to each other (a) and minimum relative distance which allows a correct detection of the two objects (b).

assume that they are separated by $v\tau_1$, where $\tau_1 < \tau/2$, τ is the pulse width and v the wave propagation velocity. In this case, when the tail edge of the pulse begins to be reflected by the first target, a large amount of scatter is already available from the target number 2, Fig. 4(a). Thus, the response of the two targets overlap and cannot be separated in the time domain. Consider now the case where the target separation is $v\tau/2$ (Fig. 4(b)). In this case, when the tail edge of the pulse strikes the first target, the early-time reflection of the second approaches the first target. Hence, a separation of $v\tau/2$ is the minimum one that allows a time separation of the reflected pulses. In other words, the minimum resolution of the system is

$$\Delta_{r_s} \approx \frac{v\tau}{2} = \frac{v}{2B}, \tag{7}$$

where B is the pulse bandwidth, which is approximately related with the pulse duration as $\tau = 1/B$. As suggested by Eq. 7, in order to achieve fine range resolution one must minimize the pulse width. This causes a reduction of the average transmitted power (for a fixed peak power) and the inability of detecting targets placed at very long distances. However, a technique called "pulse compression" (not described in this introduction) allows to obtain a very high range-resolution without decreasing the signal duration. Hence it allows both high resolution and long range detection.

The Doppler resolution is the ability of a radar to resolve the target radial velocity. The Doppler frequency produced by a single point target at radial velocity v_i is

$$f_D = \frac{2v_i}{\lambda} = \frac{2f_0 v_i}{v}, \tag{8}$$

where $f_0 = v/\lambda$, $f_0 >> f_D$ is the radar carrier frequency. The Doppler resolution is fundamentally related to the system characteristics. In today's radar, the baseband signal is converted to the digital domain by means of an ADC. In this case, an exact analogy with the range resolution is obtained

$$\Delta f_D = \frac{1}{T}, \tag{9}$$

where T is the time-domain length of the transmitter pulse. As opposed to the range resolution case, a better Doppler resolution is obtained by long pulses.
In addition to what has been presented in this section, another definition of resolution is available in a conventional radar. The angular resolution, is determined by the radiation pattern of the antenna and is defined as the beamwidth of the mainlobe. In a polar plot of the antenna radiation pattern, the beamwidth is usually defined as the angle between the two points where the magnitude of the radiation pattern decreases by 3dB with respect to the peak power.

1.6 Radar classification

Radars are often classified by the types of waveforms they use. We can also distinguish between Continuous Wave (CW) and Pulsed Radars.
This section describes the similarities and differences of the most well-known radar types.

1.6.1 *Pulsed Radar*

Pulsed radar is one of the most well-known type of radars. This name arises from the type of transmitted signal: a pulse or, more generally, a train of pulses. The target range is extracted from the two-way time delay between the transmitted and received signal. As a consequence, the range-resolution increases with a decrease of the pulse duration, or equivalently, with an increase of the pulse bandwidth. The target speed, instead, can be extracted from two consecutive range measurements or using the pulse Doppler technique.
The pulse repetition frequency (PRF) is a critical design parameter: a low PRF results in a large unambiguous range (i.e. the maximum distance that can be resolved without spatial ambiguity) but a poor average transmitted power; on the other hand, a large PRF allows a high average transmitted power but decreases the maximum unambiguous range.

1.6.1.1 *Radar Equation for Pulsed Radar*

The range equation of Eq. 4 does not take into account the nature of the transmitted signal. It is thus valid for both pulsed and continuous-wave radars. Sometimes, however, can be useful to adapt the radar equation on the actual system being considered. The radar equation for a pulsed radar, derived from Eq. 4, is

$$R = \left[\frac{\hat{P_t} \tau' G^2 \lambda^2 \sigma}{(4\pi)^3 k T_e (S/N)_{in} L} \right]^{\frac{1}{4}}, \tag{10}$$

where $\hat{P}_t$ is the peak power and τ' is the pulse width.

1.6.2 *Continuous Wave Radar (CW)*

As the name suggests, continuous wave (CW) radars transmit and receive continuous waveforms. As a consequence, the average transmitted power may be relatively high even with a medium peak output power. This simplifies the output stage and makes it more reliable. Additionally, it allows a long-range operation even with solid-state components. Depending on the nature of the continuous waveform, we can distinguish between unmodulated CW and modulated CW radars. This section gives a short insight on these two categories and explains advantages and disadvantages of both.

1.6.2.1 *Unmodulated Continuous Wave Radar*

Unmodulated continuous wave radars transmit and receive signals which may be considered to be pure sinewaves. The small bandwidth of the output signal allows to reduce interference problems with other systems. This also makes the downconversion simpler since it does not need a large IF bandwidth.
The spectrum of an unmodulated CW radar echo from stationary targets is at f_0, i.e. the frequency of the transmitted signal. Conversely, if the target is moving with respect to the radar, the received signal results shifted by the Doppler shift f_D

$$f_D = \frac{2f_0 v_i}{v}, \tag{11}$$

where v_i is the relative speed between target and radar, f_0 is the frequency of the transmitted signal and v is the wave propagation velocity in the medium. As a consequence of this frequency shift, the main advantage of a unmodulated CW radar is the ability to handle, without velocity ambiguity, targets at any range and with any velocity.
Due to the signal characteristics, a unmodulated continuous wave radar is not capable to measure the target range, except with a very low maximum unambiguous range. Sometimes, however, small AM or FM modulation is employed to give a rough indication of the range.

1.6.2.2 *Frequency Modulated Continuous Wave Radar*

As explained in Sec. 1.6.2.1, an unmodulated CW radar allows a simple and accurate recognition of the target velocity but it does not allow to measure its range, except with a maximum unambiguous range in the order of the wavelength of the transmitted signal. This issue can be resolved adding a modulation scheme on the transmitted signal. Frequency modulated continuous wave radars, for example, use sinusoidal waveforms whose frequency is changed according to a modulation signal. Since, in practice, the frequency cannot be continually changed in one direction, a periodic modulation is normally used. Fig. 5(a) shows an example of a transmitted (solid line) and received (dashed line) signal backscattered from a stationary target. The signal is supposed to be a triangular LFM (linear FM) waveform. The modulation, however, does not need to be triangular; it may be sinusoidal, saw-tooth, etc. The rate of frequency change $\dot{f}$ is

$$\dot{f} = 2f_m \Delta f, \tag{12}$$

where Δf is the total frequency variation. The beat frequency f_b, defined as the difference between transmitted and received frequency, is

$$f_b = \Delta t \dot{f} = \frac{2R}{\nu}\dot{f}, \tag{13}$$

where R is the target range. Hence, the target range R is obtained from

$$R = \frac{\nu f_b}{4 f_m \Delta f}. \tag{14}$$

When the target is moving with a radial velocity ν_i, the received signal experiences a frequency shift due to the Doppler effect. As visible in Fig. 5(b), the Doppler shift term adds or substracts from the beat frequency during the negative or positive slope of the modulated signal. Calling f_{bu} and f_{bd} the minimum and maximum beat frequency, it follows that

$$f_{bu} = \frac{2R}{\nu}\dot{f} - \frac{2\dot{R}}{\lambda}, \qquad f_{bd} = \frac{2R}{\nu}\dot{f} + \frac{2\dot{R}}{\lambda}, \tag{15}$$

where $\dot{R}$ is the target range-rate, i.e. the target velocity along a direction connecting the radar with the target. Similarly, we can obtain

$$R = \frac{\nu}{4\dot{f}}(f_{bu} + f_{bd}) \qquad \dot{R} = \frac{\lambda}{4}(f_{bd} - f_{bu}). \tag{16}$$

Thus, modulated continuous wave radars allow to retrieve both target range and velocity (range-rate).

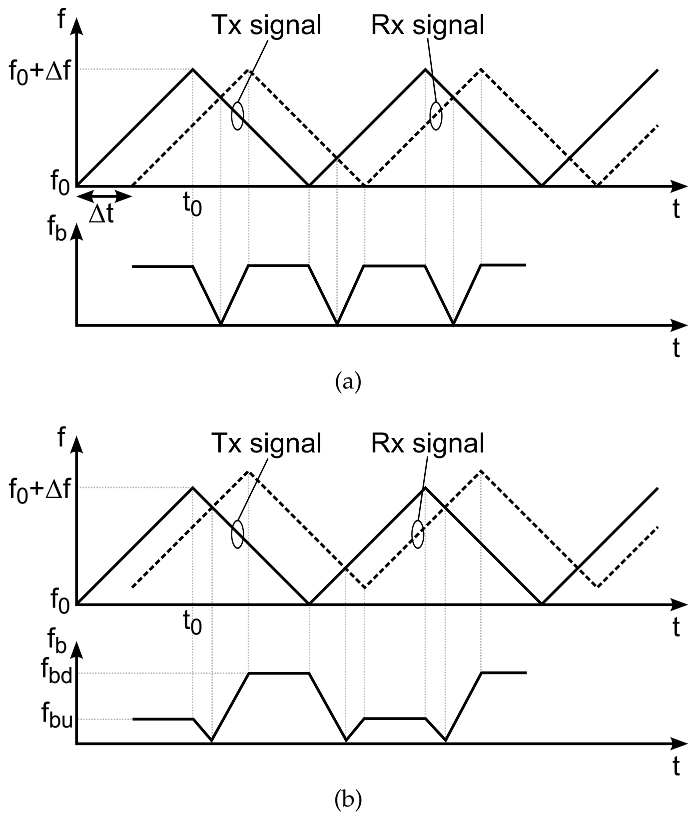

Figure 5: Transmitted and received LFM signals when the target is stationary (a) or not (b).

1.6.2.3 *Radar Equation for Continuous Wave Radar*

Like in Sec. 1.6.1.1, a radar equation for continuous wave radars is derived here. Although this implementation uses continuous waveforms, and thus infinite in length, usually the data processing is made in the frequency domain by means of an ADC and a FFT. Since the FFT process cannot handle infinite length data sets, the downconverted signal is windowed after the ADC conversion. Hence, the radar equation adapted for CW radars is

$$R = \left[\frac{P_{CW} T_{win} G^2 \lambda^2 \sigma}{(4\pi)^3 k T_e (S/N)_{in} L L_{win}} \right]^{\frac{1}{4}}, \tag{17}$$

where P_{CW} is the continuous wave output power, T_{win} is the length of the window used in computing the FFT and L_{win} is a loss term associated with the windowing process.

1.6.3 *Synthetic Aperture Radar (SAR)*

Synthetic aperture radars (SAR) are specifically used to generate a high-resolution image of the illuminated volume. They allows to obtain fine resolution in both slant range and cross range without using large antennas. Slant-range resolution is the resolution along the line-of-sight direction. It depends on the bandwidth of the transmitted pulse. Cross-range resolution, instead, refers to resolution transverse to the radar's line-of-sight along the surface being mapped and depends on the aperture of the antenna. The larger the aperture, the finer the resolution.

A synthetic aperture radar takes advantage of the relative motion between the radar and the target to obtain a large antenna (synthetic) aperture using a single small antenna. In fact, as depicted in Fig. 6, for each radar position, the transceiver transmits a short pulse, processes the backscattered signal from the target and saves the results in a memory. Finally, a high resolution image of the illuminated volume is obtained by post-processing all the measured data. Even though a single antenna is used at a time, the synthetic antenna array behaves like a real antenna array having the same dimension. A similar behavior is obtained by moving the target instead of the radar, leading to an Inverse Synthetic Aperture Radar (ISAR).

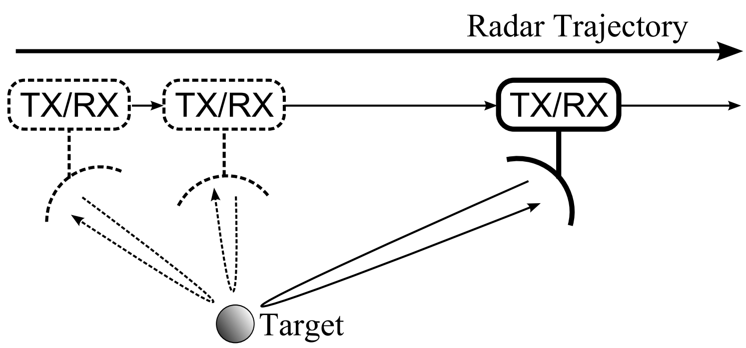

Figure 6: Principle of operation of a synthetic aperture radar (SAR).

1.6.3.1 *Stepped Frequency SAR*

As already explained, a synthetic aperture radar allows to obtain a fine resolution both in slant (Δr_s) and cross (Δr_c) range by illuminating the target from many view points. A larger pulse bandwidth corresponds to an improvement in both resolutions.
The echo signal from an illuminated target is usually observed in the time domain to obtain the desired target range. However, any signal can be described either in the time or frequency domain. In fact, a short RF pulse transmitted at a fixed pulse repetition frequency (PRF) can be defined as a Fourier series of steady-state frequency components with a frequency spacing equal to the radar's PRF [62]. Lets now see how does it work. In the TX side, the transmitted signal is a single tone stepped in frequency in order to cover the desired bandwidth (see Fig. 7). In the RX side, the I and Q components of the backscattered signal are measured and stored in a memory. As a result, a synthetic time domain pulse can be retrieved from the stored measurements by means of an IFFT. The main advantage of this implementation is that it removes the requirements for both wide instantaneous bandwidth and high sampling rate by sampling nearly-steady-state signals. Additionally, it allows to increase the resolution by generating stepped-frequency signals covering a wider bandwidth.

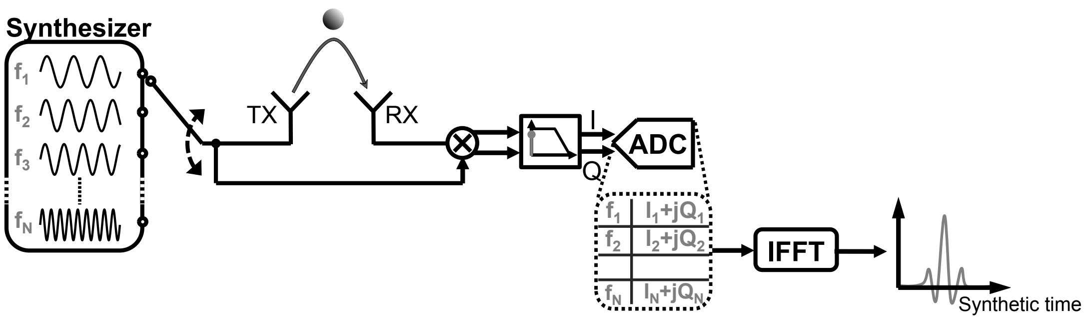

Figure 7: Principle of operation of a Stepped Frequency radar. A direct-conversion receiver is assumed.

1.6.4 *Phased Array Radar*

A phased array radar is composed by an array of N transceiver each connected to one element of an antenna array. The peculiarity of these type of systems relies on the possibility of changing the phase of the transmitted/received signal in each path. This possibility translates into a number of advantages. First, the antenna pattern can be changed, hence incrementing the antenna gain and directivity. Second, the output SNR increases and also the dynamic range. Third, the equivalent isotropic radiated power (EIRP) increases, thus a smaller output power is required for the single power amplifier. These advantages (and others) make the phased array architecture an interesting solution for a high performance radar.

Part II

ANALYSIS AND DESIGN OF AN INTEGRATED HIGH-RESOLUTION RADAR FOR BREAST CANCER DIAGNOSTIC IMAGING IN 65NM CMOS

2 INTRODUCTION

In the last few years, microwave radar imaging has been intensively investigated for medical purposes. Among the many examples of biomedical applications, the detection and early diagnosis of breast cancer has seen an increase of interest[20, 40, 50, 67, 51, 52, 35, 23, 19, 21, 47].

Breast cancer is the most common non-skin-related malignancy among female population. In the United States more than 180 thousand new cases are diagnosed and more than 40 thousand women die from this disease each year [46]. Fig. 8(a) shows the age-adjusted incidence rate per 100000 people grouped by cancer site [29]. Breast cancer is by far the most incident tumor, with an incidence of at least twice that of any other types of tumors. An early prevention is the key factor in order to deliver long-term survival to patients. A 5-years survival rate of only $\approx 20\%$ is recorded if the tumor is detected in a metastasized stage, as highlighted in Fig. 8(b). On the other hand, more than 98% cure rates are possible if the cancer is detected in its first stage.

The mammography, consisting of an X-ray image of the compressed breast, is the most common imaging tool for the detection of non-palpable tumors [46]. However, ionizing radiations together with breast compression lead discomfort in patient treatment. Additionally, more than $10-30\%$ tumors are missed by the mammography due to the presence of dense glandular tissue around the tumor, absence of microcalcifications in the early stages and location too close to the chest wall or underarm. Moreover, a large number of false-positive are diagnosed, leading to a more invasive test to assess the real absence of malignancies.

Ultrawideband (UWB) microwave imaging is an attractive alternative. It leverages the contrast of dielectric proprieties between benignant and neoplastic tissues at microwave frequencies to identify the presence of significant scatterers [38]. Fig. 9 shows the permittivity and conductivity of normal and malignant breast tissues. It is worth to notice that, compared with X-ray, a permittivity ratio as large as $1:6$ between different tissues is observed at microwave frequencies. The general concept is to illuminate the breast with an ultra wideband (UWB) pulse and collect the backscatter. From the shape and the time of arrival of the reflected pulse, information on the position and size of the scatterer are retrieved. By performing a set of measurements over different antenna positions, and by processing the obtained data in a digital beam focusing fashion, a high-resolution image

of the dielectric properties of the breast tissues can be derived.
Microwave imaging is a valid alternative to the usual mammography. The high dielectric contrast between healthy and malignant tissues at microwave frequencies makes the detection simple and reliable. These features, together with the fact that the breast does not need to be compressed, lead to a more rapid and comfortable patient examination: appropriate for a mass screening program.

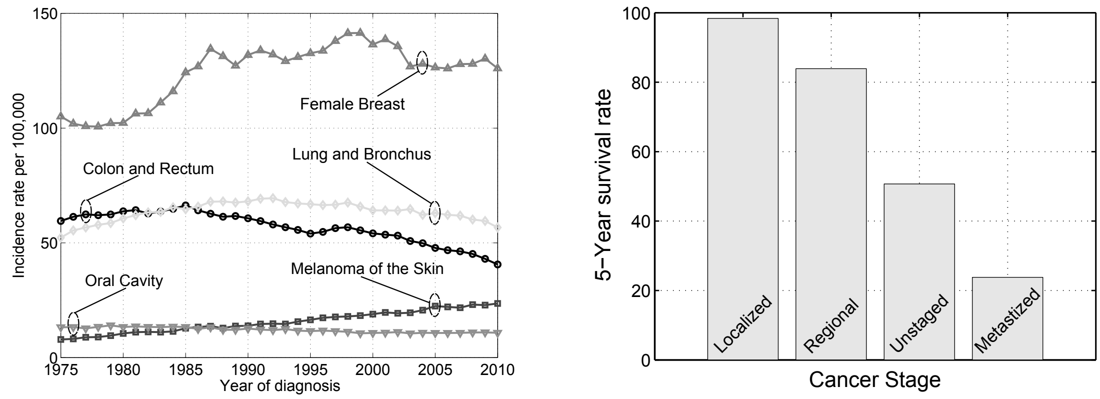

(a) (b)

Figure 8: Age-adjusted cancer incidence rates grouped by cancer site [29] (a) and 5-year survival rate with respect to the breast cancer stage [29] (b).

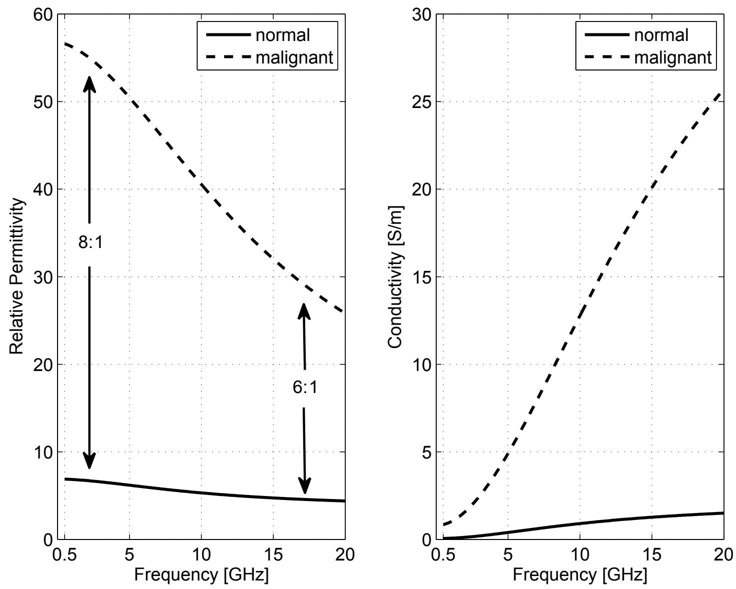

Figure 9: Cole-Cole model of the relative permittivity and conductivity of normal and malignant breast tissues.

2.1 MOTIVATIONS

Several works on microwave imaging reported over the past years show the feasibility of this technique [20, 21, 9, 34, 43, 44, 25]. Actually, the imaging system presented in [36] has demonstrated excellent results compared to X-rays and it is undergoing clinical tri-

als. As visible in Fig. 10, the patient lies in a prone position on a special examination bed while her breast extends in a hemispherical hole, of about 17cm diameter, filled with coupling liquid for better matching. The walls of the hemispherical hole are covered with a highly-dense 60-element slot antenna array connected with an external 8-port Vector Signal Analyzer (VNA) which allows 15 simultaneous S-parameter measurements in the $4-8$GHz range. The interface between antennas and VNA is made possible by an electromechanical RF switch matrix, whose size is at least three times the one of the antenna array. The whole system, composed by PC, VNA, antenna array and switch matrix, is mounted on a hydraulic trolley to ease the transportation. The presence of a highly-dedicated laboratory instrument (VNA), common to each work which reports experimental data, makes the diagnostic tool bulky and expensive. Further, the presence of costly switch matrix and high-frequency rigid-cables limits the maximum number of antennas and introduces losses, limiting the overall performance. Additionally, the limited number of simultaneous measurements increases the examination time resulting in a lower image resolution due to the patient movement [26].
As a matter of fact, the development of custom hardware is seen as a critical need by the microwave imaging community in order to improve the performance and reduce the size and cost of the system [47]. A dedicated integrated circuit can be tailored to cover the specific wide bandwidth required by medical imaging, while achieving very large dynamic ranges. The miniaturization carried about by system integration allows to envision an antenna array made of modules in which each antenna is directly assembled together with the radar transceiver chip. A switching system is therefore avoided along with any high-frequency interconnects. Only signals at low frequencies are to be distributed to the array elements. At the same time, having a transceiver for each antenna removes any limitation on the number of simultaneous measurements that can be performed. As a result, a more compact, higher performance, and lower cost system can be obtained: ideal for an early detection or post-treatment surveillance of the breast cancer.

(a) (b)

Figure 10: Microwave breast cancer imaging system developed by the University of Bristol [36] (a) and patient under examination [34] (b).

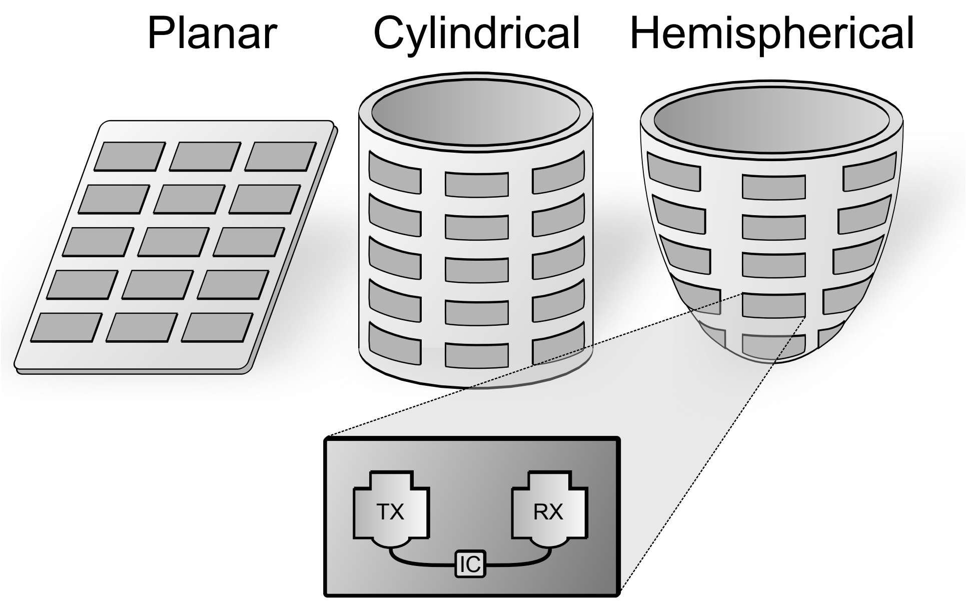

Figure 11: The three different antenna array configurations that can be used to scan the breast in a radar imaging system. Below, the envisioned imaging module made of the CMOS radar transceiver and the two wideband patch antennas.

2.2 SYSTEM OVERVIEW

As clarified in the previous section, the availability of a full-custom integrated circuit is a need for the intended application. It allows to reduce both cost and dimension, and reduces drastically the examination time. As reported in [26], in fact, the examination time plays a fundamental role in order to obtain high resolution images. A longer measurement time increases the probability of patient movement. Even the change in the blood pressure or temperature leads to approximative results.

In the microwave imaging tool proposed in this thesis, the patient's breast is positioned in front of an antenna array whose antennas are directly connected to a dedicated transceiver (Fig. 11). At a time, ideally, one transceiver transmits an ultra-wideband pulse while the others receive the backscattered signal from the breast. However, as will be better detailed out in Sec. 2.3, the combination of high resolution and large demanded dynamic range makes the implementation of the transceiver in the time-domain difficult. This problem can be circumvented by adopting the stepped-frequency continuous-wave approach (Sec. 1.6.3.1), where the UWB time domain pulse is synthetically generated starting from a set of measurements performed in the frequency domain. This operation, repeated for each antenna, can be done both in a monostatic or multistatic fashion. After all measurements are done, a $3-D$ electromagnetic characterization of the volume around the antenna array can be retrieved.

The patient position leads to different possible antenna array configurations [20]. A planar arrangement can be used to scan the naturally flattened breast when the patient lies in a supine position. On the contrary, a cylindrical or hemispherical array allow to scan the breast when the patient lies in a prone position and her breast extends through a hole in the examination bed. Among the three possible configurations, the hemispherical one is preferred because it allows the imaging from many view angles and the prone position reduces the motion effects due to patient breathing [26].

2.3 CONSTRAINTS MAPPING AND SYSTEM CHALLENGES

The continuous scaling of CMOS technologies has led to the development of plenty of new wireless standard and devices. Words like GSM, LTE, WiFi or Radar are widely used and are going to be used even more in the next few years. A complete understanding of the interaction between electromagnetic waves and human body has become a need to evaluate the potential hazard of RF radiations. In the case of biomedical application such as hyperthermia and radiometry for cancer treatment and detection, it is, moreover, a prerequisite to ensure the correct operation of the system. As a consequence, more and more papers report measurement data or fitting models on the electromagnetic proprieties of different human body tissues [38, 32, 37].

The electromagnetic properties of the breast tissues have been studied over more than 10 years. A Cole-Cole model of the relative permittivity and conductivity of normal and malignant tissues as a function of frequency is plotted in Fig. 9. This allow us to perform a finite-difference time-domain (FDTD) electromagnetic simulation to investigate the wave propagation inside the breast tissues. The simulation setup is as follows. A continuous wave source is applied to an ideal isotropic cylindrical antenna placed $1\mathrm{cm}$ away from a $2\mathrm{mm}$-thick skin layer. A $4\mathrm{mm}$ diameter tumor is inserted inside the numerical breast phantom at a distance ranging from 3 to $10\mathrm{cm}$ from the skin. The transmitted wave bounces back at the interface between adipose-dominated breast tissue and tumor while being collected by the generating antenna. The choice of tumor size and depth below the skin surface is supported by medical studies which show that smallest tumors are in the order of $9-10\mathrm{mm}$ [30] and the depht of a typical nonlactating human breast is in the order of $4\mathrm{cm}$ [15]. Additionally, almost 50% of all breast tumors occur in the quadrant near the armpit, where the breast is less than about $2.5\mathrm{cm}$ deep [48].

Fig. 12 plots the EM-simulated attenuation of the transmitted signal through the antenna-skin-antenna and antenna-tumor-antenna paths at different tumor positions. It is worth to notice the large difference between the two paths. The received signal is dominated by the skin reflection, which is large and quite constant over the entire frequency range. On the contrary, the tumor backscatter experiences a large loss and dispersion. This implies the need of a transceiver with a dynamic range in excess of $100\mathrm{dB}$ and the use of an ADC with a resolution of more than 17 bits. The use of matching liquids to reduce the air-to-skin reflection has been explored [26, 25]. However, the use of such liquids complicates the system and the almost unavoidable presence of air gaps hampers the correct imaging operation.

The radar resolution is directly related to the bandwidth of the transmitted pulse, regardless of how it has been generated. The higher the bandwidth, the shorter the pulse duration and hence the higher the resolution. The slant-range resolution Δ_{r_s} of an N-antenna array radar, i.e. in the direction of wave propagation, is proportional to the inverse of the pulse bandwidth according to

$$\Delta_{r_s} \approx \frac{v}{2B}, \tag{18}$$

where B is the signal bandwidth and v is the wave propagation velocity through the medium. Notice that the slant-range resolution is totally unrelated with the antenna array geometry and the center frequency of the transmitted signal. On the other hand the cross-range resolution Δ_{r_c}, i.e. in the direction parallel to the antenna array, is [28, 27]

$$\Delta_{r_c} \approx \frac{R}{l}\frac{v}{B}, \tag{19}$$

where R is the target range and l is the real or synthetic aperture of the antenna array (Fig. 13).
Since the smallest tumors reported in the literature are in the order of $9-10\text{mm}$ [30, 45], a sub-centimeter resolution is preferred. A resolution of $3-4\text{mm}$, also adequate for the intended application, requires a total bandwidth of $13-16\text{GHz}$ and an antenna aperture of about twice the expected tumor target range. Such a large bandwidth together with the large demanded dynamic range required to correctly process the skin and tumor backscatter makes a pulsed radar implementation difficult. A simpler and more reliable architecture uses the Stepped-Frequency Continuous-Wave approach, which allows for an instantaneous narrow noise bandwidth and a very high dynamic range. In this case, continuous waves at different frequencies covering a bandwidth $B = f_{max} - f_{min}$ are transmitted and received. A synthetic time-domain pulse can then be retrieved by means of an Inverse Fast Fourier Transform (IFFT). Calling Δf the frequency step of the system, the maximum unambiguous range R_{max}, i.e. the maximum solvable range without spatial aliasing, is

$$R_{max} = \frac{v}{2\Delta f}. \tag{20}$$

Thus, a frequency step of $\Delta f = 90\text{MHz}$ ensures a maximum unambiguous range of 0.55m, more than enough for this application.
To summarize, the combination of a total bandwidth of 14GHz and an antenna array aperture $\geqslant 10\text{cm}$ result in a total resolution (both Δr_s and Δr_c) of 3mm inside the breast. The choice of the lower and upper frequency of 2 and 16GHz, respectively, maximize the signal penetration inside the body and minimize the dynamic range requirement due to the high attenuation of the tumor backscatter.
As highlighted by Eq. 18 and Eq. 19, the resolution of the system is a function of the signal bandwidth and array aperture only. No direct influence on the number of antennas are observed. However, the signal-to-clutter ratio, and thus the image quality, are significantly improved by a highly dense antenna array [27, 28]. Unfortunately, when using a commercial VNA as a transceiver, its limited port count makes the use of a big RF switch matrix necessary to interface the antenna array to the instrument. This makes the system big, expensive and, moreover, introduces additional losses which limit the performance. On the other hand, the proposed integrated transceiver can be connected to each antenna, avoiding any high-frequency interconnects. This increases the performance and reduces the implementation costs, making this architecture ideal for a cost-effective solution for follow-up post-treatment cancer surveillance.

2.4 IMAGE RECONSTRUCTION ALGORITHM

After IFFT post-processing, the output of a measurement with an N-antenna array and integrated SFCW radar transceivers (or a commercial VNA) is, assuming a monostatic configuration for simplicity, a set of time-domain waveforms. The early-time content

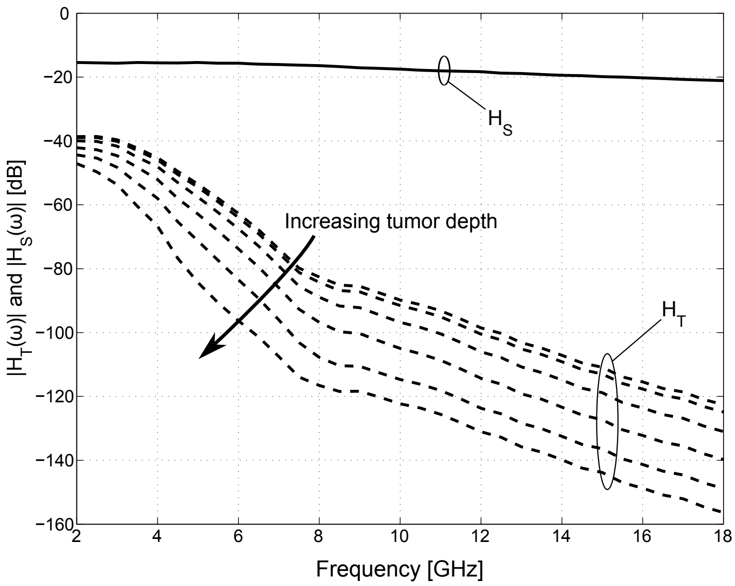

Figure 12: Antenna-Skin-Antenna ($H_S(\omega)$) and Antenna-Tumor-Antenna ($H_T(\omega)$) path attenuation for tumor depth ranging from 3 to 10cm below the skin surface. The antenna is placed 1cm away from the skin.

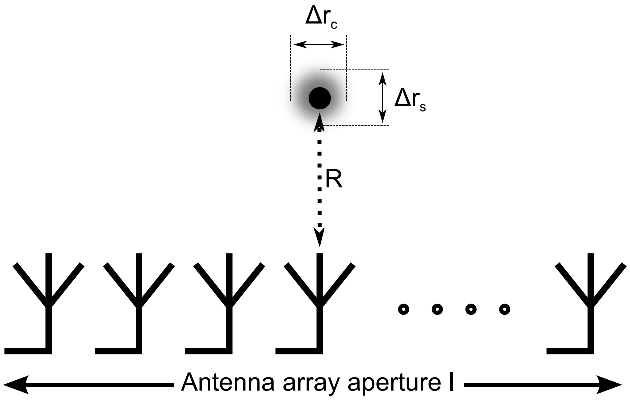

Figure 13: Typical arrangement of a N-antennas array radar showing slant and cross range resolution.

of each waveform is dominated by the large skin reflection while the late-time content contains the tumor backscatter and clutter signal. Since the skin response has a much larger amplitude with respect to the tumor response, the early-time content needs to be removed without corrupting the useful tumor signal. As proposed in [40], a calibration signal can be generated for each antenna by averaging the time response of any other antenna. In this reference signal, the skin reflection remains dominant while the tumor backscatter is reduced to negligible levels. This signal is then subtracted from the raw data, resulting in N calibrated waveforms containing only the tumor response and clutter signals. It is clear that this calibration procedure is effective as long as each antenna has the same distance from the skin. If this is not the case, more sophisticated algorithms have been presented to estimate the correct distance and efficiently remove the skin content [9, 65, 64].

The image creation can then be based on a simple delay-and-sum algorithm [54, 41]. This simple algorithm consists of calculating the intensity of each pixel by properly focusing the received signal on the pixel coordinates. First, taking into account the different electromagnetic proprieties of the different materials (air, skin and adipose-dominated breast tissue), the round-trip time $\tau_i(x, y, z)$ from the i-th antenna to the pixel of coordinates (x, y, z) is calculated. The time-domain signals $I_i(t)$ are then time shifted by the calculated round-trip time $\tau_i(x, y, z)$. In this way, the information on the considered pixel embedded in the various time-domain signals is aligned in time to the point $t = 0$. Finally, the intensity $I(x, y, z)$ of the pixel of coordinates (x, y, z) is calculated by coherently summing the contribution of all the antennas

$$I(x, y, z) = \left[\sum_{i=1}^{N} I_i(\tau_i(x, y, z)) \right]^2 . \tag{21}$$

By iterating the presented procedure for each pixel of the image, a high-resolution 2-D or even 3-D dielectric map of the inner breast can be obtained [20, 41].

2.5 SYSTEM ANALYSIS

2.5.1 *Possible System Architectures*

Based on the motivations explained in Section 2.1, we investigate the design of a low-cost fully-integrated CMOS transceiver which can be connected to each antenna of a N-antenna array and performs monostatic or bistatic measurements. Leveraging the stepped-frequency approach (c.f. Sec. 1.6.3.1, 2.3.), each IC generates a set of continuous waveforms and receives the backscattered signal from the breast. Afterwards, an external high-resolution ADC samples the low-frequency output of each transceiver and a digital processing step allows to obtain a high resolution 3-D image of the target. In the whole system, the transceiver plays a fundamental role since it must feature both large bandwidth and a very high dynamic range.

The correct system operation relies on the overall performance of the transceiver. As a consequence, care need to be taken to select the proper architecture. This section summarizes the results obtained in [6] by comparing two well-known transceiver architectures, i.e. Direct Conversion and Super Heterodyne, in terms of image quality and signal-to-clutter ratio. With the aid of a realistic behavioral model, the performance of both are evaluated in presence of the major circuit impairments like gain variation, noise, linearity and I/Q phase imbalance. Finally, the most robust and performing architecture is selected for the design of the proposed transceiver and the circuit specifications are derived based on the application requirements.

Fig. 14 shows the block diagrams of a conventional Direct Conversion and Super Heterodyne transceiver tailored for microwave radar imaging. In a direct conversion setup, a Phase Locked Loop (PLL) generates all the quadrature signals in the total bandwidth while driving both mixer and output power amplifier (PA). A TX antenna directly connected to the PA irradiates each stepped frequency waves and a RX antenna receives the backscatter from the illuminated volume. For simplicity, the antennas are supposed to be isotropic, though the comparison still holds if the antennas have constant gain over a suitable beamwidth to cover the breast surface. Furthermore,the use of two separate antennas is not a limiting factor. A similar behavior can be obtained interfacing a single-antenna to the transceiver by means of a TX/RX switch, a circulator or a directional coupler. The receiving antenna is then directly connected to a Low Noise Amplifier (LNA)

which ensures high gain featuring a low Noise Figure (NF). The down-conversion stage is implemented by a quadrature mixer having PLL and LNA outputs as inputs. Since both the received and the LO signals have the same frequency, the baseband signals (I and Q) are at DC. Finally, the mixer output is low-pass filtered and digitalized by an external ADC. Notice that the presence of the baseband filter ensures a reduction of the high-frequency spurs and acts as a anti-alias filter for the analog-to-digital converter.
In a super heterodyne scheme, a PLL feeds the PA with a stepped frequency signal covering the entire system bandwidth. With the same antenna configuration like in the direct conversion case, the reflection of the breast is received and amplified by the ultrawideband LNA. The real difference between super heterodyne and direct conversion relies on the down conversion approach. A two-step quadrature downconversion is performed to a low intermediate frequency (IF). Notice that to enable possible hardware reuse, the two intermediate frequencies need to be chosen carefully. The high needed resolution requires, moreover, a low second IF frequency. Finally, the baseband signal is low-pass filtered before being digitized.
The most evident difference between the two architectures is the system complexity. The main issue with the frequency generation in the super heterodyne architecture is that all the employed LOs have to be coherent, that is they have to display a fixed and well known phase relationship when the baseband signal is sampled. This condition is, on the other hand, guaranteed in the direct conversion transceiver, as the same LO is shared between transmitter and receiver.
Since the proposed transceiver is intended to operate in a screened medical environment, the available spectrum is supposed to be free of spurs or blockers. This relaxes I/Q requirements for the super heterodyne. However, the presence of a large "in-band" interferer, i.e. the skin reflection, may cause distortion both in super heterodyne and direct conversion due to I/Q phase mismatch.

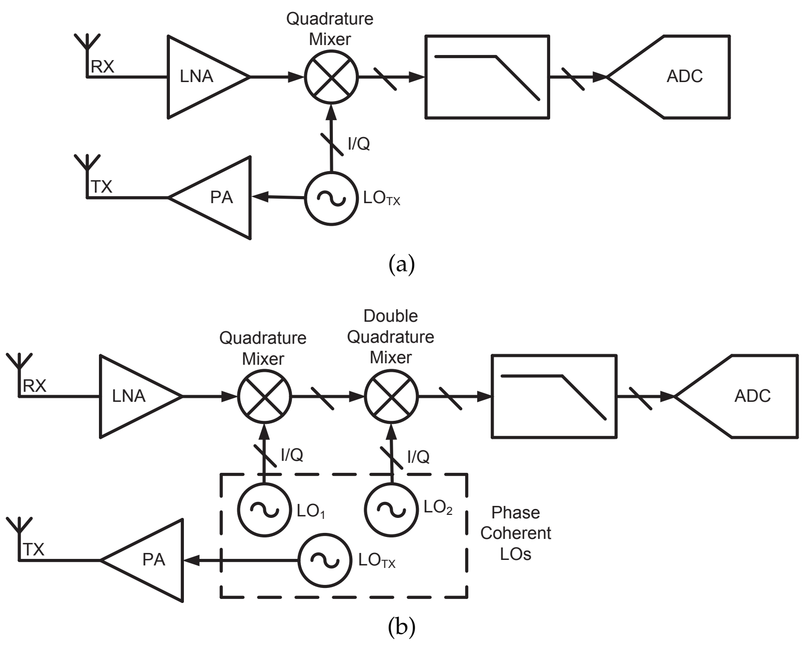

Figure 14: Block diagrams of the two UWB transceiver architectures. Direct Conversion (a) and Super Heterodyne (b).

2.5.2 *Impact of Impairments*

This section gives a short insight into the most critical circuit impairments for a transceiver tailored for breast cancer diagnostic imaging and their negative effects on the reconstructed image. Then, the most reliable and robust architecture is chosen to develop the radar transceiver.

2.5.2.1 *Gain*

Gain flatness specifies how much the conversion gain varies over the desired bandwidth. It takes into account the whole TX/RX path, including variations in the TX/RX antenna gain. Although the gain variation introduces distortion on the processed waveforms, the system shows a good robustness towards a ripple in the gain. Even a peak-to-peak ripple of $3\mathrm{dB}$ does not impair the radar performances too much, yielding a negligible level of degradation on the image quality [6].
Mismatch or process spread in the fabrication of both transceiver IC and antennas may result in a systematic gain variation over the antenna array. This contributes to deteriorate the tumor response thanks to the less efficient skin removal. However, as anticipated in Section 2.4, a more sophisticated algorithm for the skin estimation and removal can be adopted. Additionally, a calibration of the gain mismatches of each transceiver can be carried out, limiting the negative effects of the reconstructed image.

2.5.2.2 *Noise*

The impact of noise on the image quality is assessed by evaluating the time-domain waveforms processed by the transceiver. Fig. 15 shows the IFFT amplitude of the total and tumor-only backscatter from the breast. The simulation is referred to the central array's transceiver with a set of realistic parameters and impairments. Although the signal experiences a very high attenuation along the antenna-tumor-antenna path, the system shows a high robustness with respect to the thermal noise. This is due to the SFCW approach, that allows for a narrow baseband bandwidth while preserving the total UWB characteristic. Moreover, the IFFT operation leads to an intrinsic processing gain that allows the tumor enhancement with respect to the noise floor.
The high robustness to the noise is appreciated especially in the direct conversion case, where the baseband spectrum extends to DC and the high flicker noise contribution of MOS transistor is not negligible. Due to the SFCW approach the flicker noise is sampled at each frequency step f_k and is folded thanks to the sampling operation, resulting in a wideband white noise contribution [16]. In this scenario, a very low flicker noise is needed, especially for a direct conversion architecture.

2.5.2.3 *Linearity*

As discussed in Section 2.5.1, the radar operation is assumed to be performed in a screened medical environment, i.e. without other signals except those generated by the transceiver. Therefore, the linearity requirement seems to be less critical since no intermodulation between interferers occurs. However, the large magnitude of the skin reflection can excite the non-linearities of the system yielding a saturated response. Assuming to transmit a $-15\mathrm{dBm}$ tone, the maximum expected skin reflection is on the

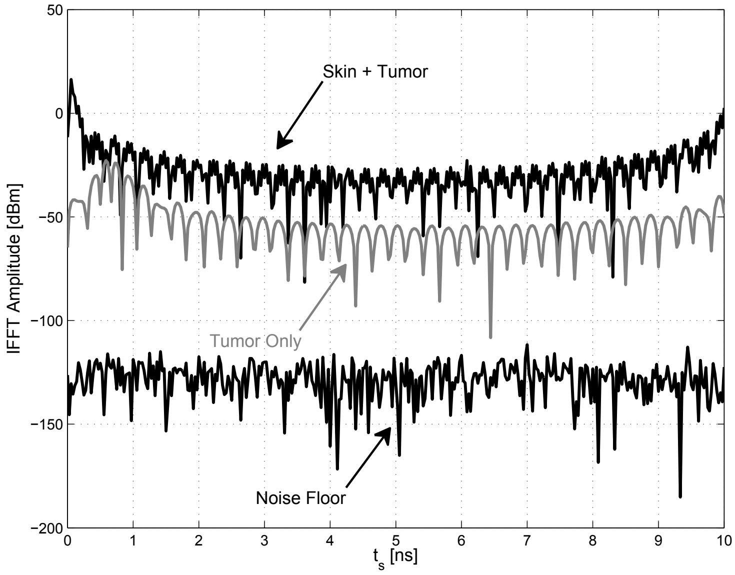

Figure 15: IFFT amplitude of the processed backscatter from the total breast and the tumor only. Plot refers to the central antenna in the antenna array configuration with a tumor depth of 3cm and a skin-antenna distance of 1cm. Other relevant system parameters are: $P_{TX} = -15\text{dBm}$, conversion gain = 40dB, NF = 10, baseband bandwidth = 100kHz, IIP2 = 20dBm, $P_{1dB} = -30\text{dBm}$ and ADC resolution of 18bit. Flicker noise, phase noise and phase mismatch are neglected.

order of −33dBm. Hence, to guarantee a correct operation, the 1dB compression point is set to be $\geqslant -30\text{dBm}$, both for direct conversion and super heterodyne.

Additionally to odd-order distortion, even-order intermodulation is a critical impairment in a direct conversion architecture [49]. In this scenario, however, the imaging procedure makes the transceiver more robust against second-order distortion. This depends to the fact that most of second-order distortion is due to the skin reflection which is common to all the antennas in the array. Thus, it is effectively removed by the calibration algorithm. Fig. 16 shows a simulation of the RMS error between two processed signals, one ideal and one affected by second-order distortion, before and after the skin calibration. The plot is normalized to half-LSB of a 18bit ADC with a 2V input range. As shown, the RMS error of the signal obtained after the calibration algorithm is more than one order of magnitude smaller than that before the calibration. To conclude, the contribution of second-order distortion is negligible for values of IIP2 greater than 10dBm.

2.5.2.4 *Phase-related inaccuracies*

A correct image reconstruction relies on the ability of the system to recover the phase of the backscattered signal. Hence, transmitted and received LO signals have to be coherent, i.e. they must exhibit a well know phase relationship. In this sense, phase inaccuracies, such as quadrature error, mismatch and phase noise, are critical impairments for a proper receiver operation.

The signal received at each antenna consists on the sum of two terms: the first is the skin backscatter and the second is related to the small reflection of the tumor. The presence of phase inaccuracies leads to two contributions of distortion, that are weighted by the antenna-skin-antenna $|H_S|$ and antenna-tumor-antenna $|H_T|$ transfer function, respectively. Remembering from Fig. 12 that $|H_S|$ is more than 20dB larger than $|H_T|$, the

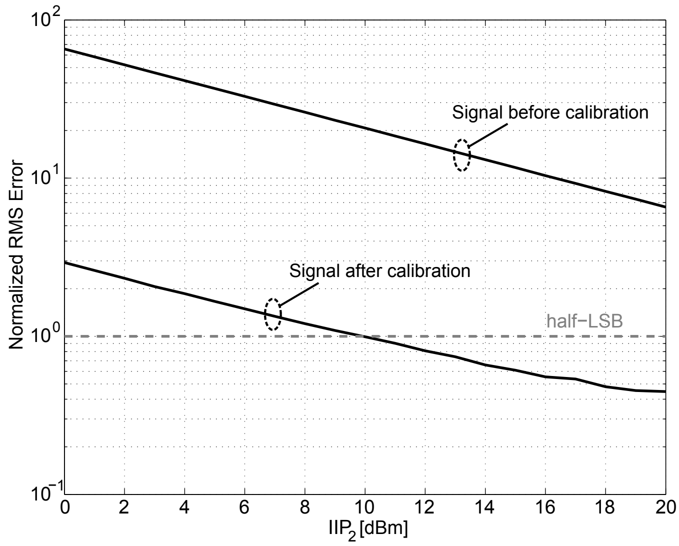

Figure 16: Comparison between the RMS error before and after the calibration algorithm. The plot is normalized to half-LSB of a 18bit ADC with 2V input range and the simulation refers to the central antenna in the antenna array configuration with a tumor depth of $3\mathrm{cm}$ and a skin-antenna distance of $1\mathrm{cm}$.

net distortion is dominated by the term relative to skin reflection. The larger the phase inaccuracies, the larger the distortion. Since the set of phase inaccuracies is different for each receiver connected to the antennas, the skin content response is different as well. This results in a non perfect skin calibration together with the inability to correctly enhance the tumor response.

Let's now consider the total phase inaccuracies as a sum of common mode ψ_{CM} and differential mode ψ_{DM} terms (see Fig. 17). Simulations show that constant values for $\psi_{CM,DM}$ do not impair the reconstructed imaged that much. In this case, only the tumor position is not well evaluated.

In general, however, common-mode and differential-mode phase mismatches are supposed to be frequency-dependent and uncorrelated between the different transceivers in the antenna array. To better capture this effect, ψ_{CM} and ψ_{DM} are modeled as gaussian variables with zero mean and variance $\sigma^2_{\psi CM}$ and $\sigma^2_{\psi DM}$, respectively. In this case, a larger variance $\sigma^2_{\psi CM}$ and $\sigma^2_{\psi DM}$ corresponds to a lower tumor amplitude and a larger clutter. Fig. 18 shows a simulation of the errors introduced by phase mismatch for different values of their standard deviation. To better appreciate the magnitude of such errors, the plot is normalized to half-LSB of a 18bit ADC with 2V input range. It is straightforward to note that the error increases rapidly with an increase in $\sigma_{\psi CM,DM}$, and its magnitude is confined in one half-LSB only for phase deviations smaller than few degrees.

The random I/Q phase mismatch is not the only phenomenon that affects the image quality. The synthesizer's phase noise (PN) also acts as a source of errors. Since I and Q signals are supposed to be generated from the same VCO, the phase noise behaves like common-mode I/Q inaccuracies.

To summarize, constant and frequency-independent phase errors are not critical for the tumor detection since they introduce only an error on the evaluation of the tumor position. On the other hand, frequency-dependent phase mismatches and phase noise are critical even for small values of their variance. They enhance the clutter level with respect to the tumor response, leading to a possible failure in the detection of the neoplastic tissue.

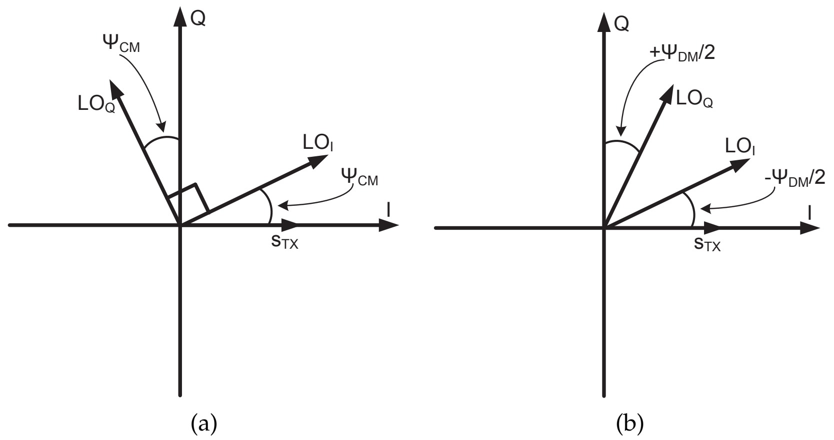

Figure 17: Phase inaccuracies of quadrature LO signals: (a) common-mode phase error and (b) differential-mode phase error.

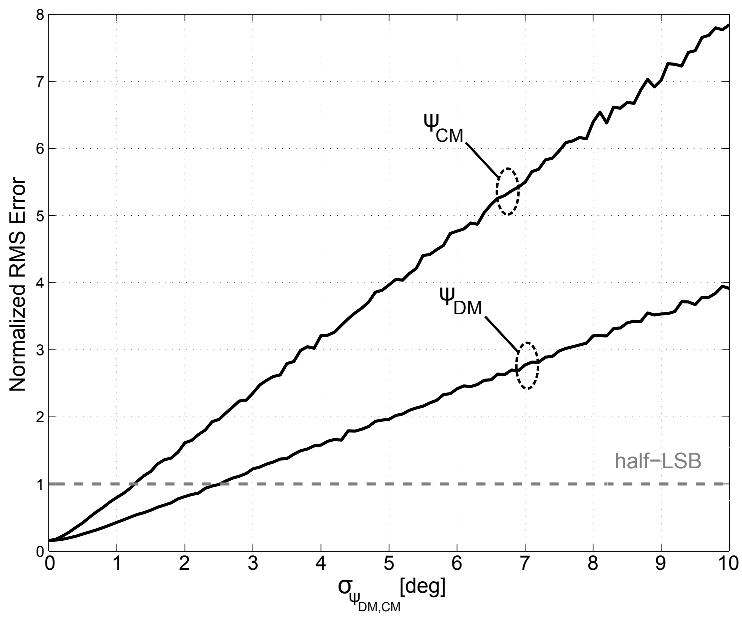

Figure 18: Normalized RMS error introduced by phase inaccuracies versus their standard deviation $\sigma_{\psi CM}$ and $\sigma_{\psi DM}$. The plot is normalized to half-LSB of a 18bit ADC with 2V input range and the simulation refers to the central antenna in the antenna array configuration with a tumor depth of 3cm and a skin-antenna distance of 1cm.

2.5.3 *Architecture Comparison*

In this section, the performance of the two different architecture, i.e. direct conversion and super heterodyne, is compared by generating a simulated tumor image with the same set of impairments. The quality of the reconstructed image is quantified by means of the signal-to-clutter ratio (SCR), defined as the average intensity of the image in the area where the tumor is located over the average intensity of the image elsewhere

$$\mathrm{SCR} = \frac{\sum\limits_{(x,y)\in A_T} I(x,y)/A_T}{\sum\limits_{(x,y)\in A_T^C} I(x,y)/A_T^C} \tag{22}$$

where A_T is the area containing the target and A_T^C is its complementary area. Fig. 19 (a) and (b) show the reconstructed image of a 4mm-diameter target obtained with a direct conversion and a super heterodyne architecture, respectively. With the set of system parameters and impairments presented in Tab. 1, the image SCRs are 17.8dB for the direct conversion and 14.5dB for the super heterodyne. This highlights the robustness of the first architecture with respect to the second one.
To conclude, direct conversion and super heterodyne architectures for SFCW breast cancer detection are compared. The most critical impairment affecting the reconstructed image is the I/Q phase inaccuracies, including the phase noise of the LOs. For this reason, the super heterodyne transceiver seems to be less robust against phase mismatch since it performs two downconversion, each of which introduces errors in the processed signal. Only when the phase errors of the second downconversion are neglected the two architectures show comparable performances. However, even in this case, a direct conversion architecture is preferable due to its simpler implementation that avoids the use of multiple coherent LOs.

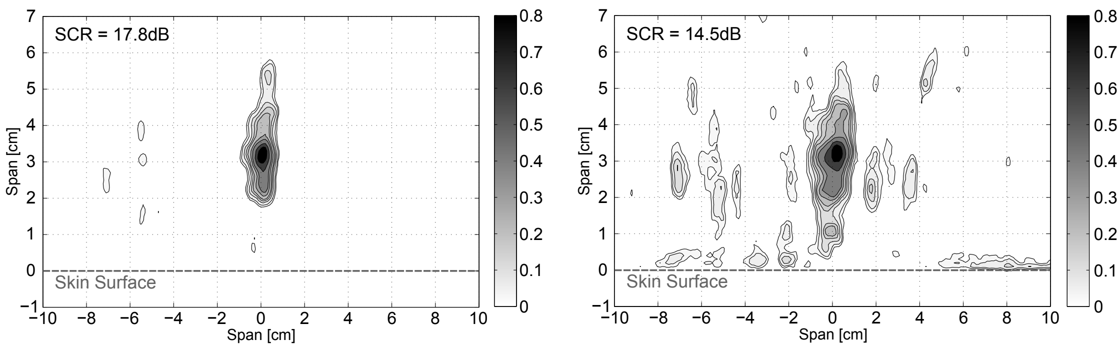

(a) Direct Conversion (b) Super Heterodyne

Figure 19: Reconstructed target image with the two architectures and the same set of system parameters and impairments as in Tab. 1.

2.5.4 *Constraints Mapping Summary*

One of the most challenging system specification arises from the breast tissue properties. The high attenuation at microwave frequencies along with the high reflection experienced by an electromagnetic wave at the air-skin interface, result in a large demanded dynamic range in excess of 100dB. The operating bandwidth is obtained directly from the required imaging resolution of 3mm inside the breast. A bandwidth from 2 to 16GHz accommodates both the high demanded imaging capabilities and the high attenuation at higher frequencies. A similar bandwidth together with the need of a very high

Table 1: Set of System Parameters and Impairments

TX Power	-15dBm
Conversion Gain	40dB
Gain Ripple	3dB
1dB Compression Point	-30dBm
IIP2	20dBm
Noise Figure	10dB
Baseband Bandwidth	100kHz
Phase Inaccuracies	$\sigma_{\psi_{CM,1,2}} = \sigma_{\psi_{DM,1,2}} = 1.5°$
Phase Noise	-110dBc/Hz@1MHz offset

dynamic range are difficult to address with a pulsed radar architecture. Thus, a Stepped Frequency Continuous Wave radar approach is chosen. The narrow instantaneous bandwidth of this radar allows for a very high dynamic range while preserving the UWB characteristic of the system.

Another specification related to the dynamic range is the ADC resolution. An effective ADC resolution in excess of 17bit is required to handle both the tumor response and the skin backscatter. Since commercial high-resolution ADCs don't have a very high bandwidth, the baseband frequency needs to be low. This, together with the results highlighted in Section 2.5.3, makes the direct conversion architecture the best candidate for this application.

Without loss of generality, setting the transmitted power to -14dBm, the high skin reflection sets the minimum $P_{1\text{dB}}$ of the receiver to -34dBm. Moreover, the weak tumor response around -134dBm (c.f. Fig. 12) sets the maximum allowable noise figure to 10dB with a noise bandwidth of 1KHz (that of the ADC).

The most critical impairments of a direct conversion receiver are the DC offset, the flicker noise and the second-order distortion. In the proposed system, the DC offset is calibrated out as discussed in Section 5.2.3.2 while the flicker noise is mitigated adopting the chopper stabilization technique. The IIP2 is specified to be greater than 10dBm as discussed in Section 2.5.2.3.

The real resolution of the reconstructed image depends strongly on the phase inaccuracies of the system. To this regard, the requirement on the I/Q phase mismatch of the local oscillator is specified to be less than $1.5°$ over the entire bandwidth (c.f. Section 2.5.2.4). This is the most challenging specification of the entire transceiver.

3 TRANSCEIVER DESIGN

This chapter describes the design of two IC prototypes, named SKuRAD1 and SKuRAD2 (Fig. 20), tailored for breast cancer diagnostic imaging. As compared to similar circuits, the presented system addresses some design challenges. First of all, it operates from S to Ku band, thus covering 3 octaves. Second, the large backscatter of the skin acts as an in-band interferer that coexists with the weak tumor echo. This calls for a large instantaneous dynamic range. Then, since the imaging process is essentially based on phase measurement, the quadrature error and phase noise have to be as small as possible and constant over the whole bandwidth. Finally, the narrow baseband introduced by the Stepped Frequency approach requires an ultra-low fliker noise corner.
The first prototype, SKuRAD1, consist of the complete direct conversion receiver. It is composed by a wideband LNA, a linearized transconductor, a current-mode passive mixer and a chopped TIA as the baseband conditioning circuit. The quadrature LO signal is generated by a reconfigurable frequency divider by $1, 2$ or 4 starting from an external signal that spans the higher octave. For testing purposes, SKuRAD1 contains, moreover, a first version of the VCOs that will be implemented in SKuRAD2. The author's main contribution include the design of the programmable frequency divider, the design of the input test buffer used to feed it with an external signal and the design of the output test buffer used to verify the correct operation of the divider in the frequency range of interest. The second prototype, SKuRAD2, is the complete radar transceiver. It essentially contains the same receiver as in SKuRAD1 (with minor changes in the signal path) with an improved version of the frequency divider. Then an integer-N PLL generates all the signals in the higher octave and a harmonic-rejection output buffer drives the output antenna. The author's main contribution for this IC include the re-design of the improved frequency divider as well as the design of the harmonic rejection output buffer.

3.1 THE CHOICE OF THE TECHNOLOGY

The target of this work is the realization of an ultrawideband radar tailored for the breast cancer diagnostic imaging. As stated in the previous sections, the microwave characteristics of the human body together with the required resolution for this application, results

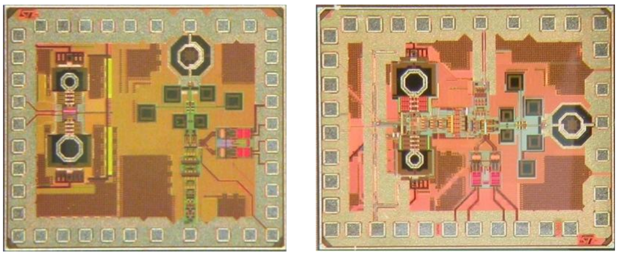

(a) SKuRAD1 (b) SKuRAD2

Figure 20: Microphotograph of SKuRAD1 and SKuRAD2.

in a 14GHz bandwidth and a very high demanded dynamic range. To achieve these performances, the system must feature a flat conversion gain in a very large bandwidth and must exhibit a low noise figure. A low flicker noise is also important to avoid to corrupt the desired DC signal. The most stringent specification, however, is the maximum tolerable I/Q phase mismatch of 1.5° over the entire bandwidth.

As will be presented later in this chapter, the proposed LO generation chain is made of a PLL that covers the higher octave ($8 - 16$GHz) followed by a programmable frequency divider which can divide by 1, 2 or 4 and generates the quadrature signals over the entire 3 octaves. The programmable frequency divider is definitively the most critical block of the design. It must be fast enough to cover with margin the higher octave and to accurately generate the quadrature signals.

A 65nm CMOS technology is used in this design as it features an adequate f_T to enable the operation of the circuits in the band of interest.

3.2 RECEIVER - SKURAD1

This section describes the design of the first integrated circuit, named SKuRAD1, tailored for breast cancer diagnostic imaging. Its block diagram is shown in Fig. 21. To amplify the weak tumor backscatter, it uses a wideband LNA followed by a linearized transconductor. Then a current-mode passive mixer downconverts the signal while a chopped Transimpedance Amplifier (TIA) drives an external $\Sigma\Delta$ ADC. The quadrature LO signal in the $1.75 - 15$GHz range is obtained by means of a programmable frequency divider by $1, 2$ or 4 (named DQG) which is fed by an external signal in the $7 - 15$GHz range. An input test buffer interfaces the external LO input signal with the frequency divider and an output test buffer allows to verify the correct operation of the DQG. The last two blocks are used only for test purposes.

3.2.1 *Low Noise Amplifier (LNA)*

The Low Noise Amplifier is the first stage of the receiver chain. It must provide good input matching and high gain while featuring a low Noise Figure. Due to the instantaneous narrow bandwidth of the Stepped Frequency approach, more than one LNA architecture is possible. One of them can use a set of switchable narrowband LNAs centered at different frequencies. This solution can be very simple but it occupies a large area. Another solution can use a single reconfigurable narrowband LNA, but in this case the presence of an additional tuning line makes the design less robust and difficult.

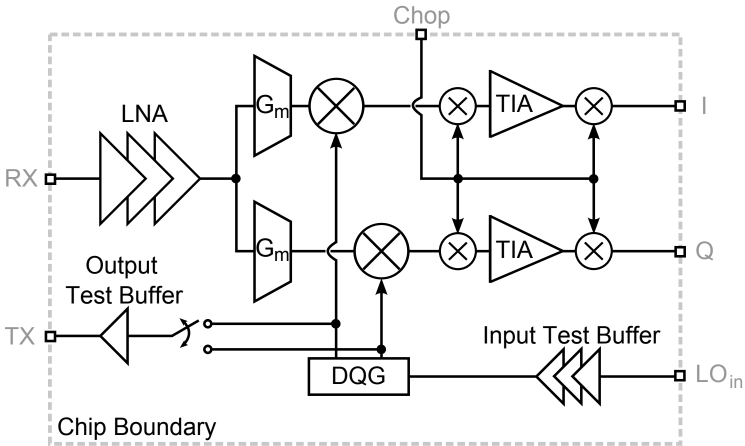

Figure 21: SKuRAD1 block diagram.

The proposed solution uses a cascade of three sections to instantaneously cover the entire bandwidth. The first stage is responsible for input matching and noise figure. Since a reactive input matching network is not recommended due to the high fractional bandwidth and the relatively low lower frequency, a noise cancelling approach is used. This solution allows to decouple the input matching from the noise figure, exploiting the simultaneous noise and power matching [10]. Fig. 22 depicts the proposed noise cancelling LNA, which is composed by a common-gate (CG) and a common-source (CS) stage. The noise generated from transistor M_1 is added in phase opposition at the output nodes without impairing the useful signal when $|Z_{CG}| = |Z_{CS}|g_{m2}R_s$, where R_s is the source impedance. In this solution, the combination of the input inductor $L_{in} = 520pH$ and the common-gate input impedance results in a good input matching over almost 4 octaves, from 1.5 to 20GHz. Moreover, it takes advantage of the topology to perform the single-ended to differential conversion without the need of an additional balun. The bias current of the CG and CS is $2mA$ and $7mA$ respectively while the MOS dimensions are $W_1 = 40\mu m/L_1 = 0.06\mu m$ and $W_2 = 80\mu m/L_2 = 0.06\mu m$. This arrangement translates into $|Z_{CG}|/|Z_{CS}| \approx 3$. A good cancelling matching is obtained by implementing resistance R_{CS} as a parallel combination of three resistors of value R_{CG}.
The second and third stage of the LNA are visible in Fig.23 and are, respectively, a differential and a pseudo-differential pair. This choice allows to improve both signal balance and linearity. The bias current is, $6mA$ and $12mA$.
All three stages use shunt-peaked load to widen the bandwidth. The gain of the three stages are 13dB, 7dB and 2dB respectively with an additional 8dB peaking around 17GHz. This is used to equalize the complete LNA response and expand even more the bandwidth. Since each shunt-peaked load has intrinsically a low quality factor, for a compact layout each inductor (except for the input inductor L_{in}) is made by stacked square coils.

3.2.2 *Low 1/f Downconverter*

Resistively-degenerated transconductance (G_m) stages are used in the I/Q paths to convert the LNA output voltage into current, as shown in Fig. 24. Each G_m stage is biased with $8mA$, and makes use of a $R_{deg} = 46\Omega$ degeneration resistor. Self-biased active loads are employed: this configuration avoids the need of an auxiliary common-mode

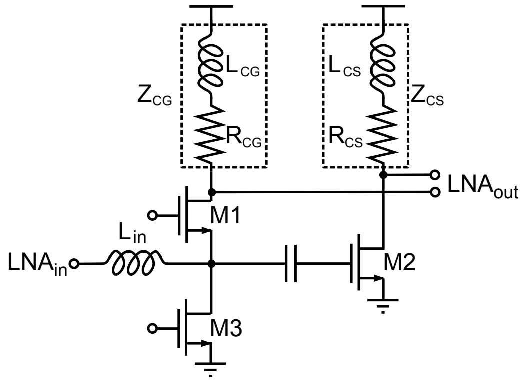

Figure 22: Noise Cancelling LNA. Biasing not shown.

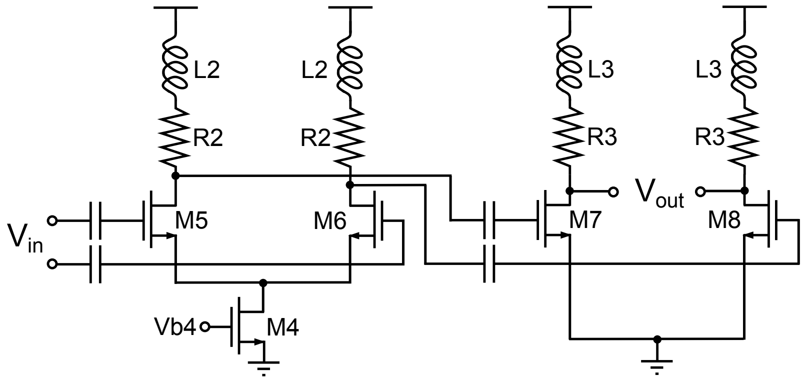

Figure 23: Second and third stage of the LNA. Biasing not shown.

feedback control loop.
Current-mode passive mixers are capacitively coupled to the transconductor outputs. This choice results in both good linearity and good noise performance, preventing the flicker noise of the commutating devices to corrupt the downconverted signal [13]. A large and constant swing of the LO signal across the band is essential to achieve good mixer performance. The proposed DQG plays a key role in this, as discussed in Section 3.2.3.
The use of passive mixers is not sufficient to address the high flicker noise of MOS transistors. Typically, current-mode mixers are loaded by baseband transimpedance amplifiers (TIAs), based either on common-gate stages or on op-amps with resistive feedback. The flicker noise of the devices of the TIAs is not suppressed, ultimately setting the flicker noise corner of the receiver. To overcome this limitation, the chopper stabilization technique is used to reduce the flicker corner below 100 Hz. Chopper stabilization is a widespread technique, usually applied to voltage amplifiers [17, 16, 4, 66]. Its use with TIAs in a downconversion mixer is, however, unprecedented. The combination of passive current-mode switches and chopper stabilized TIAs results in a highly linear, low noise downconversion mixer with a very low flicker noise corner.
The schematic of the proposed TIA is shown in Fig. 25. The amplifier is based on a common-gate stage. Compared to an op-amp with resistive feedback approach, this choice allows to decouple the input and output common-mode voltages. As a consequence, the input common-mode voltage can be kept low, which is beneficial for the mixer switches (nMOS transistors), without impairing the output swing. Local feedback

(transistors M_3 and M_8) is used around the common-gate input stage (transistors M_2 and M_9) to decrease the differential TIA input resistance, $R_{in,TIA}$, as

$$R_{in,TIA} \approx \frac{2}{g_{m2} g_{m3} r_{01}}. \tag{23}$$

The input branches of the TIA are biased with 250µA each, such that a differential input resistance of 35Ω is achieved at a small power consumption. The input currents are mirrored to the output branches where resistors R perform the current-to-voltage conversion.

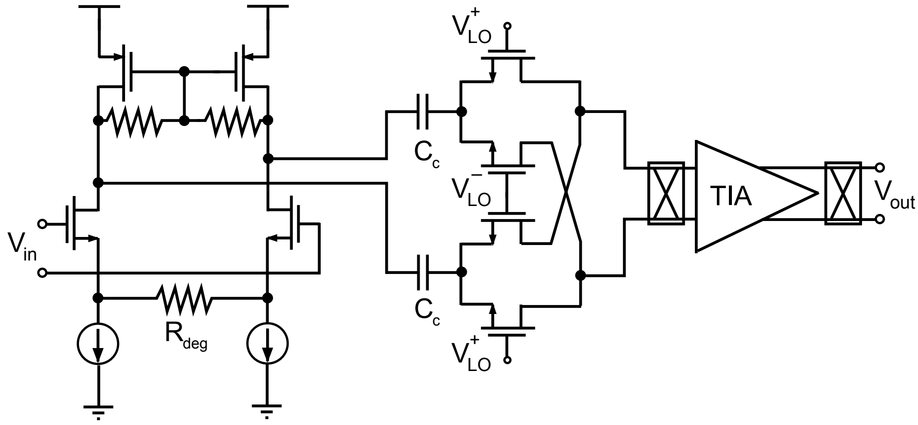

Figure 24: Schematic of one path of the quadrature downconverter.

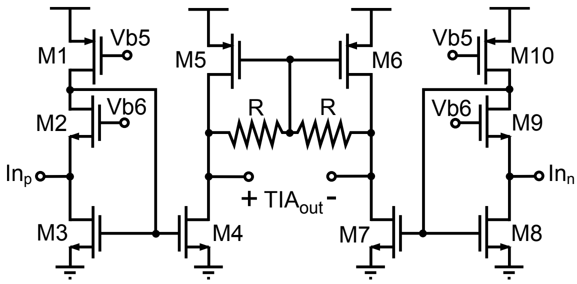

Figure 25: Schematic of the transimpedance amplifier (TIA). Biasing not shown.

3.2.3 *Frequency Divider and Quadrature Generator (DQG)*

As discussed, the local oscillator (LO) quadrature accuracy is the most stringent specification for a receiver tailored for stepped-frequency microwave imaging. The quadrature error must be small, and constant over the entire wide receiver bandwidth. Sudden changes in the I/Q phases cannot be tolerated, even if they occur for few frequencies in the wide covered span.

Accurate generation of quadrature signals over multiple octaves can be achieved by using static frequency dividers by two. However, this technique cannot be used in the proposed radar receiver because of the high frequencies involved. Apart from the power consumption of the divider yielding the frequencies for the higher octave, the generation of the LO signals at twice the frequency, i.e. from 15 to 30GHz, with extremely low phase noise (also a sensitive specification for the system [6]) and large tuning range, would re-

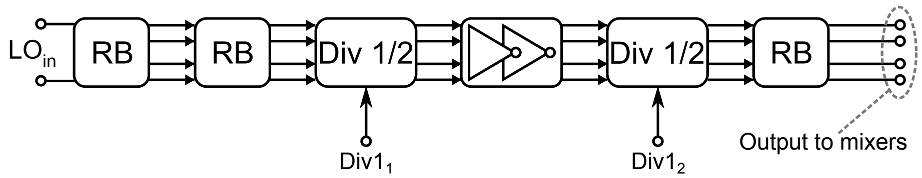

Figure 26: Block diagram of the proposed programmable frequency divider/quadrature generator (DQG).

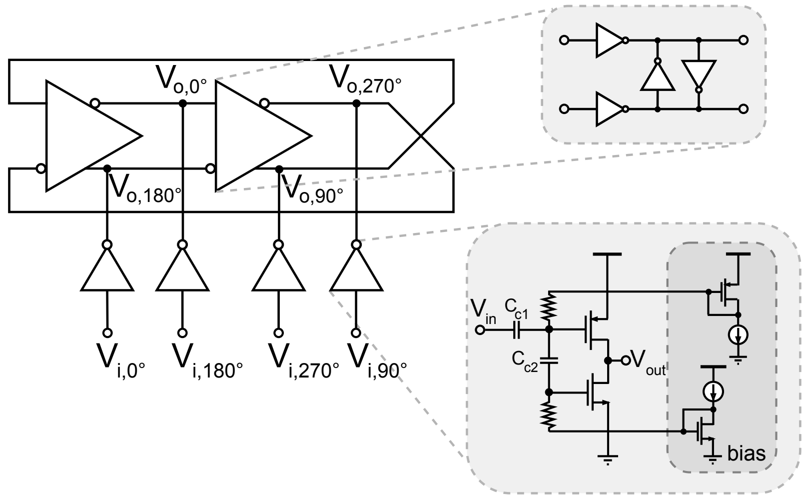

Figure 27: Simplified schematic of the regenerative buffer (RB).

quire many power hungry VCOs to meet the requirements. The use of a polyphase filter to generate the I/Q phases in the higher octave is also a possibility. To meet the required quadrature accuracy over one octave while being robust to process spreads, the filter should feature more than three sections, thus introducing more than 18dB losses. Since a large LO swing is required by the mixer switches, buffers would be needed to drive the polyphase filter and to regenerate the signal after it. Simulations suggest that such buffers would consume as much current as the entire proposed DQG. In addition, the LO signal would be tapped from different points of the circuit to cover the various octaves. As a consequence, the feed to the mixer could be uneven across the band in amplitude and, most importantly, in phase.

The proposed solution is able to address all the aforementioned issues. It is composed by a cascade of two programmable injection-locked dividers. Each divider can divide by 1 (no frequency division) or 2 depending on one configuration bit. A PLL (not implemented in SKuRAD1) is supposed to generate signals over the higher octave, namely from 7.5 to 15GHz. The DQG is then capable of producing quadrature signals over three octaves starting from the PLL output.

The block diagram of the DQG is shown in Fig. 26. Two regenerative buffers (RBs), based on injection locked ring oscillators, drive the first programmable divider. An interstage buffer made of two-stage tapered CMOS inverters interfaces the two programmable dividers. The interstage buffer is AC-coupled to the output of the first programmable divider, and the input inverter is biased at its logical threshold by means of replica biasing. At the end of the chain, another regenerative buffer is used to drive the mixers. The injection locked regenerative buffer intrinsically operates at large output swings, hence providing a large drive to the mixers with minimum amplitude variations

across the band. The interface between the LO distribution and the mixers is the same regardless the DQG is dividing by 1, 2, or 4. This avoids discontinuities in the operation of the DQG due to changes in the loading of the LO distribution chain. The architecture of the DQG, made of a cascade of several injection-locked stages, has the advantage of progressively improving the quadrature accuracy [33], such that every stage contributes to reduce the quadrature error in any used configuration. Moreover, the use of injection locked circuits based on inductorless ring oscillators results in very wide locking ranges [57]. As a consequence, the DQG does not need any calibration nor tuning.
The schematic of the regenerative buffer is shown in Fig. 27. The core of the circuit is a two-stage differential ring oscillator in which the delay cells are differential static CMOS latches with input buffers as injection elements. Although the RB is basically a digital circuit in its structure, a full custom design is needed to guarantee the correct operation up to 15GHz. Analog techniques are also required. An example is given by the injection buffers of the RB, shown in Fig. 27. The buffers are essentially CMOS inverters. However, to make them operate correctly in the required frequency range, even in presence of input signals with less than rail-to-rail swing, AC-coupling through capacitors $C_{C1} = 310\text{fF}$ and $C_{C2} = 120\text{fF}$ is employed, which makes the inverters work as analog amplifiers. This is similar to the approach reported in [39]. Note that two decoupling sections are used in cascade, as opposed to connecting one terminal of both and directly to the input. The chosen arrangement in fact reduces slightly, but effectively, the capacitive loading on the driving stage. Moreover, it allows for a more compact layout since the smaller can be conveniently placed in the neighborhood of the pull-down nMOS, leaving more space for the larger. The bias voltages of the nMOS and pMOS transistors are obtained by means of current mirrors, shared among the buffers.
The schematic of the programmable divider is shown in Fig. 28. Similarly to the RB, the programmable divider is built around a two-stage differential ring oscillator. The topology of the delay cell is also similar (cf. Fig. 28), although the transistor size is differently optimized in each block. The possibility of having a programmable divider is based on the multiphase injection locking concept [14]. Depending on the phase progression of the signals fed to the divider, harmonic or super-harmonic injection locking occurs, enabling either division by 1 (same input and output frequency) or frequency division by 2. Different division ratios are hence obtained by reconfiguring the injection network, as shown in Fig. 29. In the divide-by-one mode, a complete quadrature sequence (0°,90°,180°, and 270°) must be injected at the four nodes of the ring oscillator. Consequently, nodes "A" (cf. Fig. 29) are grounded and quadrature phases are injected into the ring oscillator through pseudo-differential pairs. As shown in Fig. 28, the pull-up transistors of the delay inverters of the ring oscillator are effectively made larger, as compared to the divide-by-two configuration, to counteract the undesired pull-down effect of the injection devices (M_{j1} through M_{j4}) in Fig. 29. The latter would in fact tend to decrease the output common mode voltage of the ring oscillator, and in turn the oscillation amplitude. In the divide-by-two mode, nodes "A" in Fig. 29 are floating. A signal with 0° phase is fed to both injection devices M_{j1} and M_{j2}, that thus operate as a single transistor connected across the output nodes of one of the delay cells of the ring oscillator. Similarly, a signal with 180° phase is fed to injection devices M_{j3} and M_{j4}. Such a direct injection arrangement enables superharmonic injection-locking operation [57], and consequently frequency division by 2. The injection devices M_{j1} through M_{j4} are AC-coupled to the phase distribution multiplexers, which are built out

of tri-state CMOS gates. The DC bias voltage fed to the injection transistors is tailored for divide-by-1 and divide-by-2 operation. It is important to emphasize, however, that these bias voltages are set by design, and that no tuning is required for the DQG to operate over three frequency octaves.

The frequency divider is supposed to be driven by an integrated PLL which generates signals over the higher octave. However, in the first radar prototype (SKuRAD1), the PLL has not been implemented. Thus, an input buffer has been designed to interface the differential frequency divider inputs with an external single-ended signal generator (cf. Fig. 21). This buffer is made by a cascade of three resistively loaded differential and pseudo-differential pairs.

A single common-drain output buffer (cf. Fig. 21) has been designed to verify the locking extrema of the DQG and measure the amplitude mismatch of the four phases. Four pass-transistors are used to connect the four DQG output signals to the single output buffer. Since this buffer is for testing purposes only, a high performance is not needed here. Hence, to avoid to introduce large parasitics to the frequency divider outputs, the pass-transistors are very small and are placed close to the mixers. The bias of the buffer is programmable, such that it can be turned off without corrupting the normal operation of the DQG.

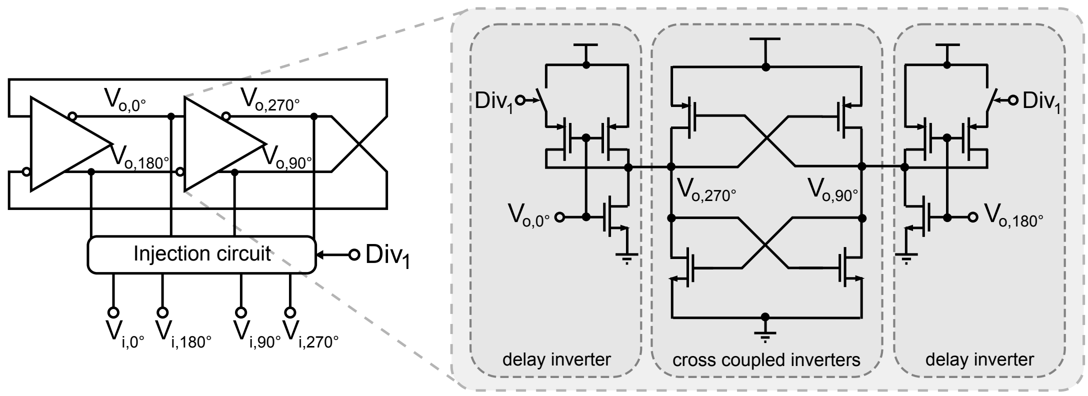

Figure 28: Simplified schematic of the proposed programmable frequency divider by 1 or 2 with a detailed schematic of the delay cell.

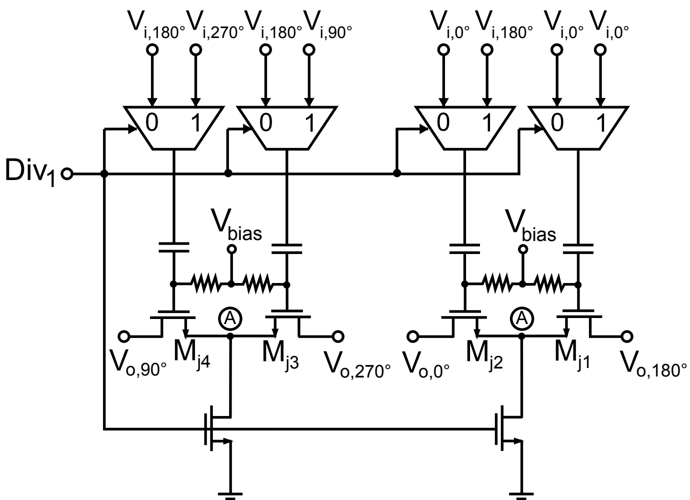

Figure 29: Simplified schematic of the injection network of the programmable divider.

3.3 TRANSCEIVER - SKURAD2

This section describes the design of the second radar prototype, named SKuRAD2, tailored for breast cancer diagnostic imaging. Its block diagram is shown in Fig. 30. Concerning the receiver chain, only small changes have been done with respect to the previous design. These include the LNA biasing circuit and the correction of a mistake in the connections between the mixers and the TIAs (there was a small layout difference in the I and Q connection to the TIAs). The programmable frequency divider is completely new and is capable to work at higher frequencies compared to the previous design while consuming less power. The frequency divider is then fed by an integer-N PLL which generates all the signals in the higher octave (i.e. from 8 to 16GHZ). Finally, a Harmonic Rejection TX buffer drives the TX antenna. Notice that SKuRAD2 represent the complete transceiver and, hence, it can be used to perform some realistic imaging experiments (Sec. 5.2).

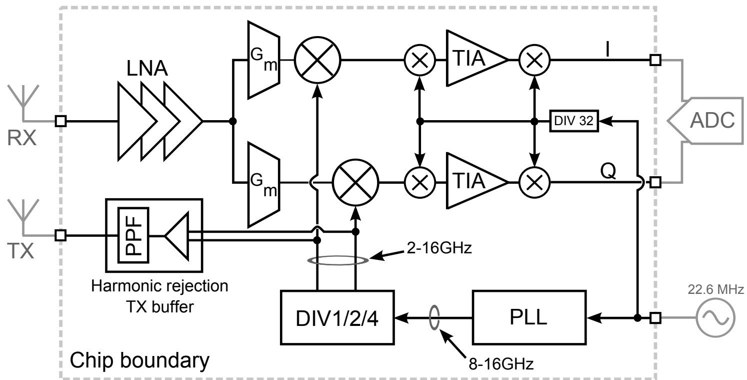

Figure 30: SKuRAD2 block diagram.

3.3.1 *Integer-N Phase Locked Loop (PLL)*

The frequency synthesizer has to generate all the signals in the $8-16\text{GHz}$ range while having good phase noise performance over the entire bandwidth. The proposed solution consists of an integer-N PLL locked to a 22.6MHz reference (Fig. 31). It relies on two VCOs not to trade the phase noise performance for the tuning range. Each VCO is followed by a prescaler by 4, such that multiplexing between the two PLL feedback signals is implemented at a lower frequency. The PLL loop is then closed by means of a current steering Charge Pump (CP) and a third order Loop Filter (LF). Both of them contribute to reduce reference spurs.

3.3.1.1 *Voltage Controlled Oscillator (VCO)*

The two VCOs are differential LC oscillators (Fig. 32) with nMOS cross-coupled pair as negative resistance element and pMOS as tail current generator connected to the center tap of the tank inductor. Each tank is optimized for a correct operation in the lower and higher frequency band. To maximize the quality factor, each inductor is an octagonal single-turn thick-metal coil (this technology does not allow circular shapes). The corresponding inductance value is 350pH and 180pH for the lower and higher band VCO respectively.

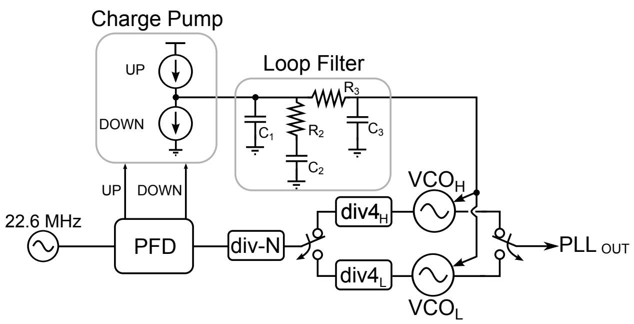

Figure 31: Frequency synthesizer block diagram.

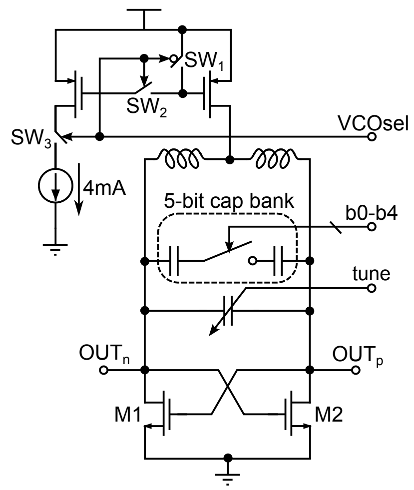

Figure 32: Schematic of one differential LC oscillator.

Tuning is achieved by a 5-bit binary-weighted switched-capacitor bank and a small MOS varactor for continuous tuning. The unity cell of the capacitor bank is visible in Fig. 33. It is composed by a series of 2 MIM capacitors and an nMOS M_{SW}. When the control voltage $V_b = 0V$, the nMOS is OFF and hence the differential capacitance offered by the cell is roughly $C_{par}/2$ (assuming $C \gg C_{par}$), where C_{par} is the parasitic capacitance at nodes A and B. Otherwise, when $V_b = V_{DD}$, the nMOS acts as a closed switch and the differential capacitance become $C/2$. The width of transistor M_{SW} is choosen as a compromise between quality factor and tuning range [56]. The larger the switch, the higher the quality factor but the lower the C_{max}/C_{min} ratio due to the bigger parasitic capacitances. The presence of transistors M_{P1},M_{P2},M_{N1} and M_{N2} ensures the correct DC voltage across the switch. When $V_b = V_{DD}$, they set the source and drain voltage to $0V$, allowing the switch to turn on in a correct way. Otherwise, when $V_b = 0V$, they are used to set the drain and source DC voltage to V_{DD}. This reduces the parasitic capacitance C_{par} by biasing the drain-bulk and source-bulk junction of M_{SW}.
In order to allow to turn on just one VCO at a time, control switches are present in the bias network. When $VCO_{sel} = V_{DD}$, SW_3 and SW_2 are closed while SW_1 is open. In this case the bias current is correctly mirrored with a mirror ratio of 3.5 and 5 for the VCO_L and VCO_H respectively. When $VCO_{sel} = 0V$, SW_3 and SW_2 are open, SW_1 is closed and the VCO is turned OFF.

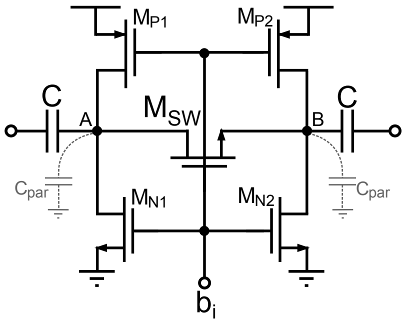

Figure 33: Unity cell of the capacitor bank.

3.3.1.2 *Charge Pump and Loop Filter*

The charge pump is the key element of a PLL design. A simplified diagram is shown in Fig. 34. It is composed by two current sources controlled by the Phase-Frequency Detector (PFD) which inject and remove a charge into the loop filter (LF). The width of UP and $DOWN$ control signals determine whether the net charge is injected or removed from the LF. This causes an increase or decrease of the output voltage V_{LF}. Ideally, when the lock condition is reached, UP and $DOWN$ pulses have the same width resulting in a zero net charge injected in the filter.

However, when implemented at circuit level, both PFD and charge pump show non-idealities that reduce the PLL performance. The main unwanted effect is the presence of reference spurs caused by mismatches between I_{UP} and I_{DOWN} or by charge sharing [12], charge injection and clock feedthrough.

The mismatch between charging and discharging current usually occurs due to the finite output impedance of current sources caused by the channel length modulation of deep submicron devices. This leads a non-zero charge injected in the filter even when the loop is in lock condition. Moreover, the charge stored in the channels of the switch transistors reaches the output node when they are turned ON or OFF, leading to a charge injection error. Finally, charge sharing between parasitic capacitances can occur when the MOSFET are switched ON.

A schematic of the proposed charge pump is depicted in Fig. 35. Various techniques are employed to minimize the generation of reference spurs. A current steering topology is adopted, with a charge pump current equal to $I_{CP} = 500\mu A$. The use of two complementary branches allows the I_{UP} and I_{DOWN} currents to continuously flow through the charge pump. Since the current flowing through transistors M_{P1} and M_{N1} is kept constant, the voltage variations at nodes A and B are minimized. As a consequence, the charge sharing from nodes A and B to the output node V_{LF} is drastically mitigated. A unity gain configuration op-amp is used to force the voltage of node C in the auxiliary branch at the same level of the output node V_{LF}. To minimize the mismatches between the charging and discharging currents I_{UP} and I_{DOWN}, an additional op-amp is used to ensure that nodes C and D are at the same voltage level. The amplifier forces the I_{UP} and I_{DOWN} currents to be equal, in the limit of transistor mismatches. A relatively large capacitor is required to guarantee the stability of the loop. In this design, $C_{stab} = 24.8pF$ ensures a phase margin of 70° across PVT. Transistors M_{P3}, M_{P5}, M_{N2} and M_{N4} are driven by complementary phases and are used as dummy switches to decrease the undesired charge injection at the output node and at node C when devices M_{P2}, M_{P4}, M_{N3} and M_{N5} are turned off.

To achieve an even lower spur level, the PLL loop filter (LF) is a third order design, Fig. 36. It is useful to filter out spurs or noise generated by the PLL at frequencies ten times the loop bandwidth. All the filter components are integrated. The value of capacitors $C_1 = 1.8pF$ and $C_2 = 58.3pF$ and resistor $R_2 = 11k\Omega$ are chosen to set the PLL loop bandwidth (1MHz) and phase margin (60°), while the value of capacitor $C_3 = 660fF$ and resistor $R_3 = 30k\Omega$ are set as a compromise between higher out-of-band attenuation (and thus spur reduction) and lower noise generated by R_3.

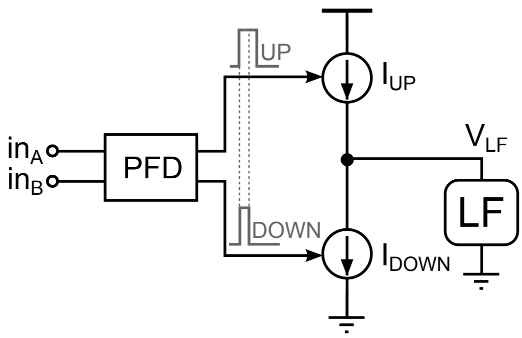

Figure 34: Conceptual block diagram of a simple charge pump.

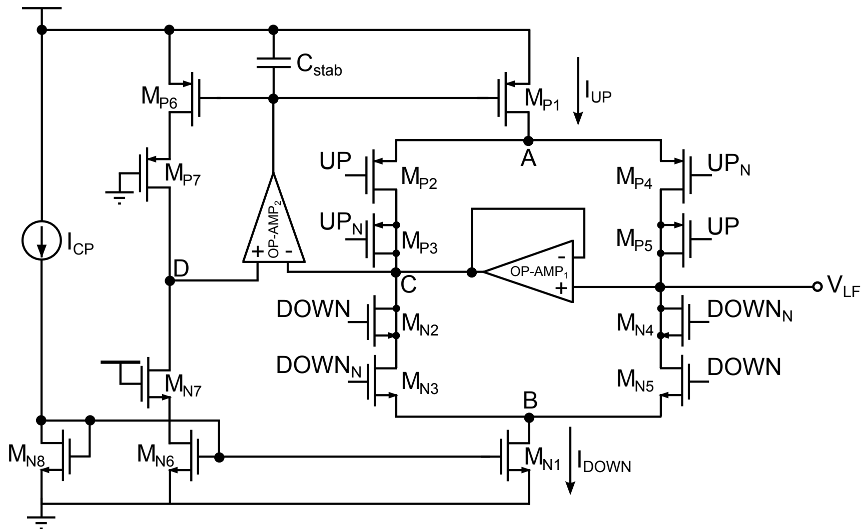

Figure 35: Schematic of the proposed charge pump.

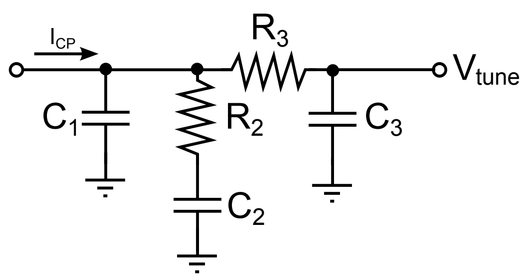

Figure 36: Schematic of the proposed third order loop filter.

3.3.1.3 *Prescaler*

A prescaler by 4 is used to relax the design of the programmable divider and to multiplex between the two feedback path at a lower frequency. It is based on injection locking on a four-cells ring oscillator and is similar to the design presented in [58], as sketched in Fig. 37. Each cell is a differential CMOS inverter having nMOS as pseudo-differential pair and pMOS as cross-coupled load. The injection method is based on the direct injection mechanism [55] enabled by nMOS connected across the output terminals of each cell. To widen the locking range, a multi-phase injection technique is adopted [14]. Concerning this, the use of a 4-cells ring oscillator requests a differential input signal which is simply available at the VCO output nodes.
The size of the transistors of the inverter cell is different in the two prescalers in order to adapt the self oscillation frequency of the ring oscillator to the output frequency of each VCO. It is 5/0.08μm and 5/0.06μm for the low and high band prescaler (inside the same cell, nMOS and pMOS have the same size). The size of the injection transistor M_{inj} is, instead, the same for both designs and is 5/0.06μm. Finally, a switch connects each delay cell to V_{DD} and allows to turn OFF the prescaler when the respective path is not used. Otherwise, without an injection signal the ring oscillator would oscillate at its self-oscillation frequency and this may corrupt the signal in the other path or increment the output spur level.

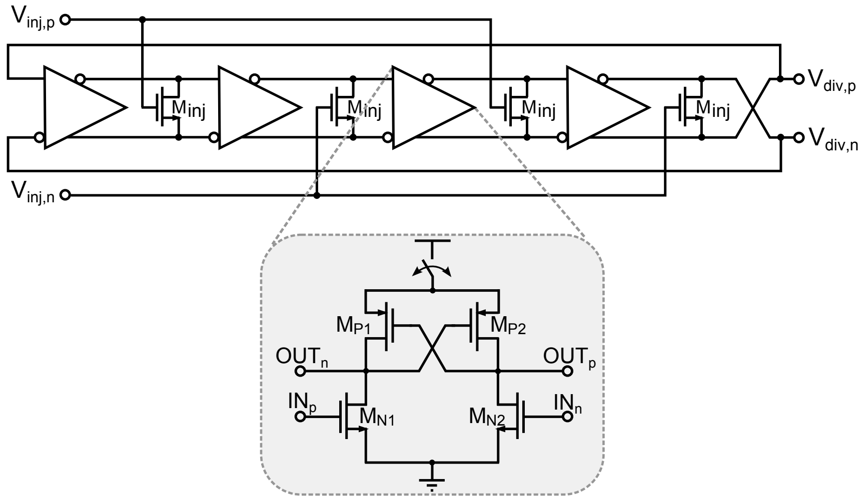

Figure 37: Schematic of the proposed injection-locked prescaler by 4 with a detailed view of the delay cell.

3.3.1.4 *Low-Frequency Programmable Divider*

The programmable divider is based on a modular dual-modulus architecture like in [59] and is composed by a chain of 7 2/3 divider cells. The complete schematic is sketched in Fig. 38. The 2/3 divider cell divides the frequency of the input signal either by 2 or 3 depending on the logic level of signals p_i and M_i. The M_i signal becomes active only once in a division cycle and is propagated back in the chain regardless of the value of p_i input. When M_i becomes high, the state of the input is checked and, if p_i = "1", the 2/3 cell is forced to swallow one extra period of the input signal, thus dividing by 3.
A chain of n 2/3 cells is able to implement a frequency divider of any integer modulo from 2^n to $2^{n+1} - 1$. The division range is thus limited to roughly a factor of two, which

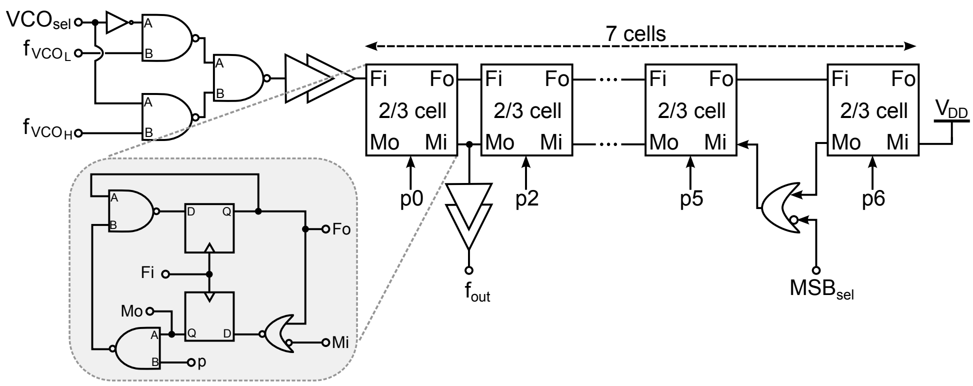

Figure 38: Schematic of the programmable frequency divider used in the PLL loop.

is not enough to cover with margin the 1-octave tuning range of the PLL. In order to extend the division range, a simple OR gate is added to the schematic. When MSB_{sel} = "0" the M_i input of the sixth cell becomes high regardless of the output of the next cell. In this way, the chain behaves like a $n_{min} = 6$ cell frequency divider and hence the minimum and maximum division factors become unrelated [61]. By choosing $n_{min} = 6$ and $n_{max} = 7$ a division factor ranging from $N_{min} = 64$ to $N_{max} = 255$ is obtained. This means that, taking into account the division by 4 introduced by the prescaler, the covered frequency range is $[4f_{REF}N_{min} \quad 4f_{REF}N_{max}] = [5.78GHz \quad 23GHz]$ which is more than enough to cover 1 octave with some margin for PVT variations.
The schematic of the single 2/3 cell is visible in the inset of Fig. 38. It is made of two D-type flip flop implemented in TSPC logic. This allows to avoid additional inverters that would make the design operate at much lower frequencies. A multiplexer realized as a cascade of NAND gates is added in front of the programmable divider in order to choose between the two prescaler outputs, depending on which VCO is turned ON.

3.3.2 *Improved Frequency Divider and Quadrature Generator (IDQG)*

The LO frequency divider is the most critical block of the design. It generates all the quadrature signals from 2 to 16GHz with a small I/Q phase error. SKuRAD1 prototype uses a chain of two injection-locked programmable dividers to achieve the desired performance. Each divider can divide by 1 or 2, obtaining a total maximum frequency division of 4. In this way, the LO chain generates quadrature signals in the range $1.75 - 15GHz$.
The solution proposed in SKuRAD2 is based on the same idea. The VCOs generate differential signals which are fed to an improved version of the programmable frequency divider by means of tri-state gates. A block diagram of the frequency divider is shown in Fig. 39. A chain of 3 regenerative buffers (RB - the same regenerative buffer implemented in SKuRAD1) interfaces the PLL output with the divider core; one more RB is used as buffer to the mixer and the transmitter output. The divider core is the innovative solution of this design. It is based on injection locking on a 4-stage differential ring oscillator (see Fig. 39 and Fig. 40). Leveraging the multi-phase injection technique, and reconfiguring the injection network, the ring oscillator is forced to lock to the fundamental PLL frequency, or to half the fundamental, or to one fourth of it. As a consequence, in a single stage, division by 1, 2, or 4 is achieved. This arrangement proves to be more

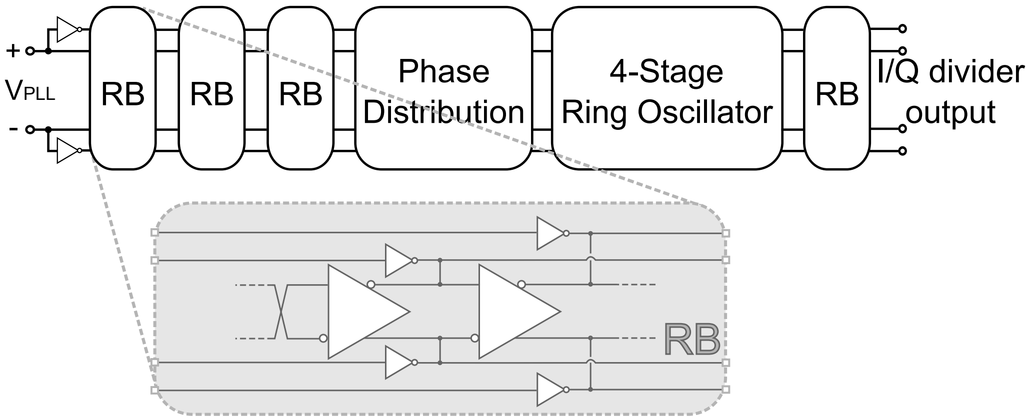

Figure 39: Block diagram of the proposed programmable frequency divider (IDQG).

robust and to be able to operate at higher frequencies with respect to a solution made of a cascade of two dividers by 1 or 2, as proposed in SKuRAD1.
If a correct phase sequence is injected in multiple points of a ring oscillator, the locking range is widened [14]. Conversely, a wrong phase sequence results in a very narrow locking range, and injection locking is unlikely to take place. Therefore, a ring oscillator injected with signals at a given frequency will select, among different possible modes of operation, the one that matches the provided input phase sequence. In the differential 4-stage ring oscillator used in this work, the phase difference between the input of each delay cell and the corresponding non-inverting output is 45°. Hence, the output nodes of the ring oscillator are in an octet-phase sequence. To force locking at the fundamental frequency (divide-by-1 mode), the injection network is configured as a pseudo-differential pair that injects quadrature signals into alternate delay cells, as shown in Fig. 40(a). In divide-by-2 mode, the octet-phase sequence at the output corresponds to a quadrature sequence at the divider input. In this case, the injection network is reconfigured to operate as a single device with drain and source connected between the output nodes of the differential delay cell (direct injection), as shown in Fig. 40)(b). Consequently, the injection network operates as a mixer and super-harmonic injection occurs [57]. Finally, in divide-by-4 mode, the octet-phase sequence at the divider output corresponds to a differential sequence at the divider input (see Fig. 40(c)). Thus, differential phases are fed to the injection networks in a direct injection fashion.
An injection-locked divider based on a ring oscillator is an inductorless circuit. It occupies a small area and features a wide locking range, in excess of several octaves [57]. As a consequence, no tuning or calibration is needed. Nevertheless, the free running oscillation frequency of the ring oscillator must be in the neighborhood of the divider output frequency. To guarantee the oscillation up to the maximum frequency (i.e. 16GHz), the differential delay cell must be carefully designed. A very simple cell is shown in Fig. 41(a). It uses only 4 MOSFETs (except the injection network) and occupies a small area. Its small dimension, with small output capacitances, results in a low power consumption and a very large locking range. However, the output frequency of a ring oscillator made of a cascade of 4 of these cells may be very low. In addition, when loaded with an output buffer, the frequency further decreases. This problem may be attenuated by using the cell of Fig. 41(b), which is the same implemented in the DQG of SKuRAD1. An increase of the output frequency is obtained by an increase of $W_{M_N^*}$ and $W_{M_P^*}$. This results in a larger cell dimension with associated larger power consumption and lower

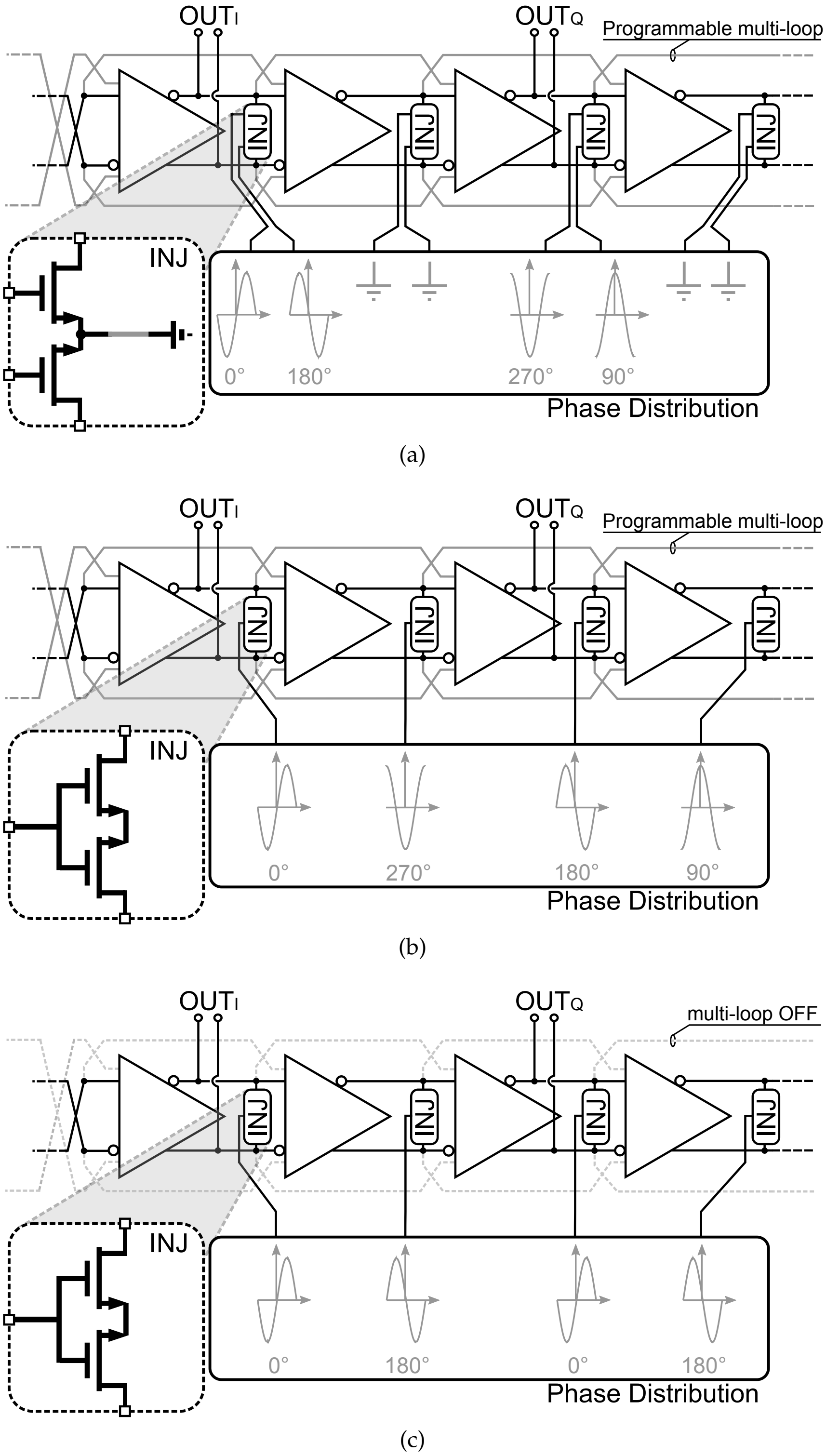

Figure 40: Schematic of the divider core in the three modes of operation: divide-by-1 (a), divide-by-2 (a) and divide-by-4 (a).

locking range with respect to the previous cell. Anyway, a cascade of 4 of these cells results in a frequency well below the target of 16GHz. Forcing a 4-stage CMOS differential ring oscillator to operate at frequencies in excess to 16GHz is, in fact, difficult even in scaled technologies. As a consequence, a multi-loop topology is employed to additionally increase the oscillation frequency of the ring [42]. Fig. 41(c) shows the schematic

of the proposed delay cell. It is substantially a combination of (a) and (b). Hence, it features a large tuning range with a lower power consumption with respect to (b). Most importantly, it allows the multi-loop operation through the secondary inputs $IN_{2_{p,n}}$. In the divide-by-4 operation mode, however, a lower output frequency is needed. In this case, MOSFETs $M_{P_{EN}}$ can be turned off in order to disable the multi-loop feature.
A phase distribution network is used to route the quadrature phases to the injection circuitry, and thus select the desired division ratio. It is implemented by means of multiplexers based on tri-state gates, as shown in Fig. 42. The multiplexers select which of the four possible phases is routed to each injection device, depending on the desired frequency division ratio. Since each injection transistor is fed at most by three different phases (see Fig. 40), the fourth tri-state gate of the multiplexer is a dummy element to balance the capacitive load seen by the RB, while minimizing the fan out of the multiplexers. Each of the four phases is routed to at most seven different injection devices, as shown in Fig. 40. Each signal is AC-coupled to seven different multiplexers by reusing the same biasing network, as illustrated in Fig. 43. This arrangement balances the loading on the RB for the various signals of the phase sequence. In Fig. 43, the schematic of the basic tri-state gate of the multiplexer is also shown.
The RBs, the same as in SKuRAD1, are injection-locked 2-stage differential ring oscillators, as shown in Fig. 39. The principle of operation is similar to the divider core. However, the lack of reconfigurability leads to an even wider locking range. Hence, the same design can be operated both as a buffer at the input of the divider and at its output without the need of any tuning. The RBs show a locking range in excess to 3 octaves.
Quadrature signals are generated by the RBs out of the differential PLL signals. Since a multi-phase injection results in a wider locking range [14], two loaded inverters facilitate the injection locking of the first RB (Fig. 39). It is worth to notice that the quadrature accuracy here is not ultimately important since, along the chain, each injection-locked stage contributes to progressively improve the quadrature accuracy [33]. Thus, even an initial error of some tens of degrees allows to obtain the desired quadrature error of $\leqslant 1.5°$.

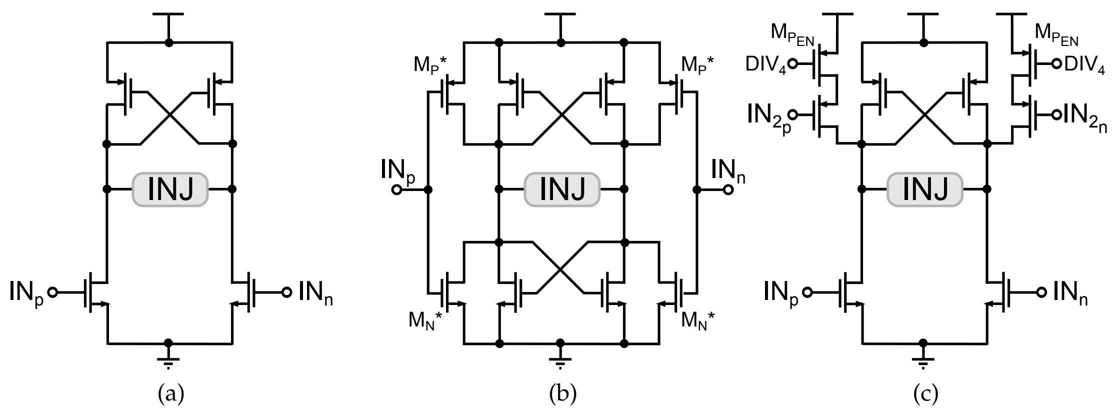

Figure 41: Schematic of various type of delay cells that can be used in a ring oscillator. Simple and without frequency tuning (a), cell used in SKuRAD1 that allows the frequency tuning (b) and the proposed SKuRAD2 cell that allows the multi-loop feature (c).

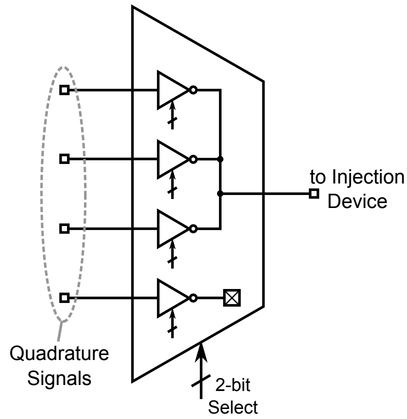

Figure 42: Schematic of the multiplexer used in the phase distribution network.

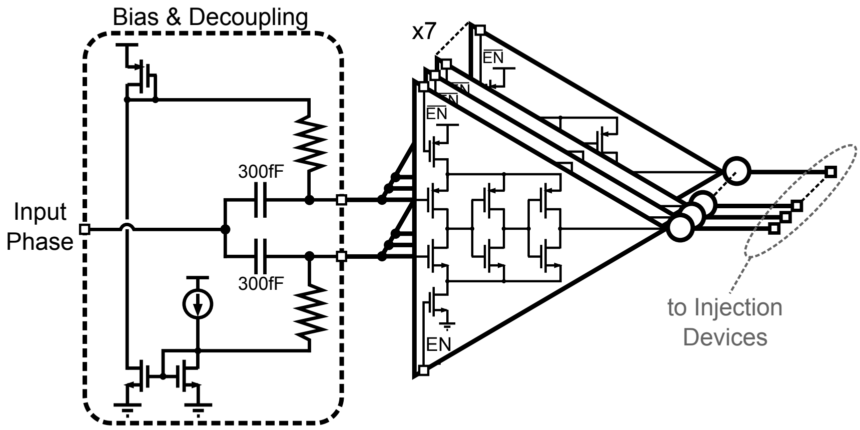

Figure 43: Sketch of the phase distribution network.

3.3.2.1 *Layout Strategies for High Quadrature Accuracy*

To guarantee such a high quadrature accuracy, some efforts have to be spend on the layout of the frequency divider. In fact, the layout of this block took a long time, comparable with the time required for the design.
The first obvious rule that has to be observed is that the layout must be symmetrical. Apart from this, however, other strategies have been put in place. All paths have been made balanced with respect to the capacitive parasitics. Every employed capacitor (for the AC-coupling for example) has been screened with grounded lines to reduce the cross-coupling between paths carrying signals with different phases and to balance the parasitic capacitances.
To guarantee some spacing between AC-coupling capacitors and to ensure symmetric interconnections between IDQG and phase distribution network, the layout of the programmable frequency divider must be stretched, as visible from the concept-layout of Fig. 44. As a result, large parasitic capacitances are associated with the long interconnections between the 4 cells of the multi-loop ring oscillator. To reduce the undesired cross-coupling between paths carrying different phases, every long interconnections has been similarly screened with grounded lines (Fig. 44). This increases the parasitic capacitance to ground, but strongly reduces the Miller effect. As a consequence, each output node of the IDQG results loaded with a smaller parasitic capacitance. This also helps the operation in the higher octave.

Finally, every circuit cell (e.g. the delay cell in the divider and RB) has been also screened, such that every corresponding MOS device in different cell instances is loaded with similar parasitic capacitances.

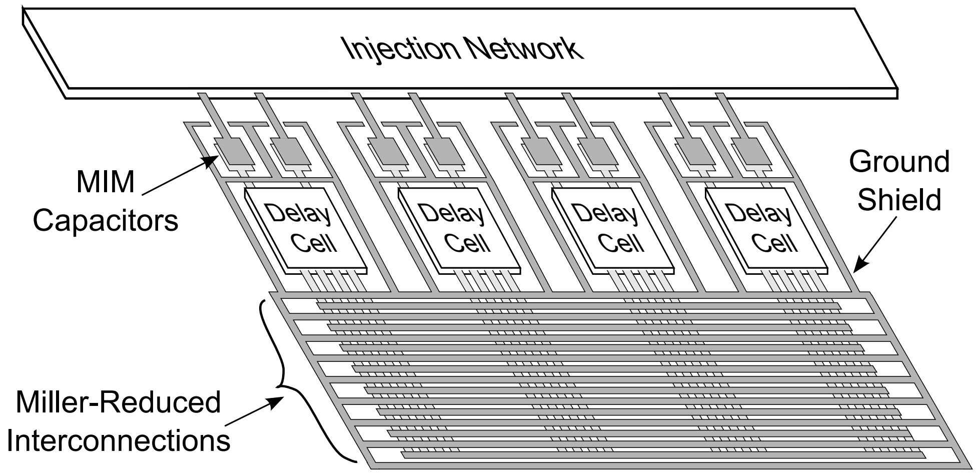

Figure 44: Concept-layout of the IDQG showing the strategies adopted to reduce and balance the total parasitic capacitances.

3.3.2.2 *Quadrature Accuracy and IDQG Performance*

To assess the robustness of the proposed LO generation, a set of 100 Monte Carlo simulations have been done over the extracted layout with respect to process variations and mismatch.

Fig. 45 shows the histograms of the quadrature error in the three different division modes for an input frequency of 16GHz. As shown, the standard deviation is always smaller than 0.35°. The same simulation, made over the entire frequency range, is shown in Fig. 46. Here, the standard deviation of the quadrature error Δ_ψ is shown to be smaller than 0.5° in the total band of $2 - 16$GHz.

The simulated 0-peak amplitude of the fundamental harmonic of the mixer input signals is shown in Fig. 47(a). As visible, the signal amplitude is constant over the entire bandwidth and is always larger than $V_{DD} = 1.2V$. This follows from the fact that the IDQG outputs rail-to-rail square waves. To conclude this section, Fig. 47(b) shows the standard deviation of the amplitude mismatch between any of the quadrature phase signals. In the three modes of operation it is always smaller than 6mV.

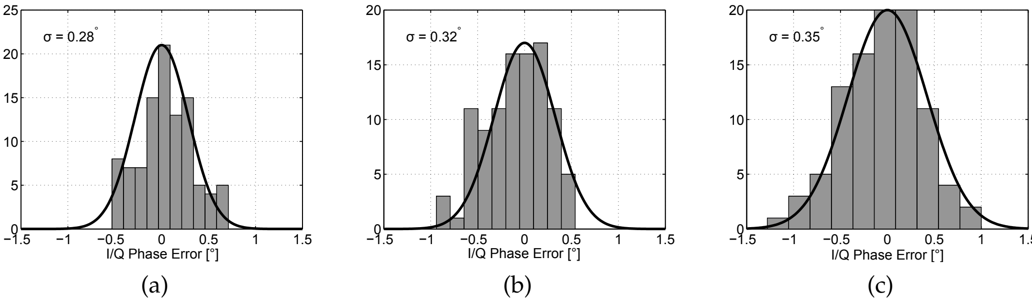

Figure 45: Histograms showing the simulated (100 Monte Carlo iterations) quadrature error in the three modes of operation: divide-by-1(a),divide-by-2(b) and divide-by-4(c).

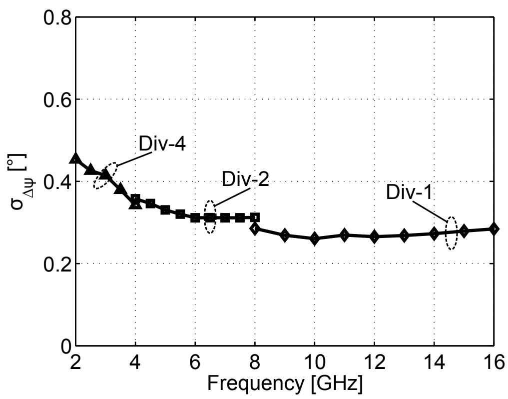

Figure 46: Simulated (100 Monte Carlo iterations) standard deviation of the quadrature error Δ_ψ.

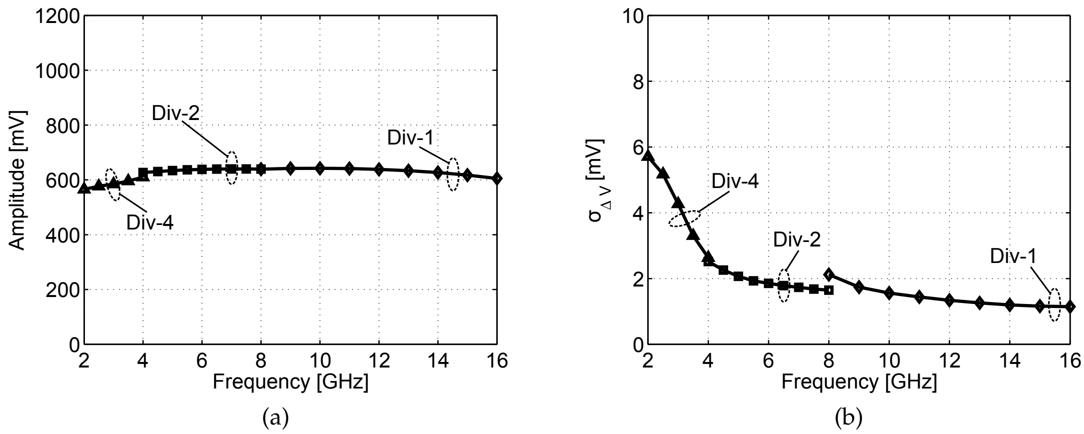

Figure 47: Simulated $0 - peak$ voltage at the mixer inputs (a) and its standard deviation $\sigma_{\Delta V}$ (b).

3.3.3 *Harmonic Rejection TX Buffer*

One of the biggest impairment that may affect a multi-octave transceiver is the presence of the transmitted signal harmonics. These harmonics might fall within the bandwidth of the receiver and corrupt the desired signal. This effect is heavily accentuated in the proposed application, where a very high dynamic range is required to resolve the weak tumor backscatter. In the selected direct conversion architecture, the differential quadrature downconverter inherently suppress even harmonics, but is sensitive to odd ones. to a first-order approximation, a harmonic rejection of 100dB is needed at the TX side to achieve the desired 100dB dynamic range. However, the third harmonic of the transmitted signal is in band ($2 - 16$GHz) only for output frequencies smaller than 5.3GHz. A lower frequency corresponds to a lower attenuation of the antenna-tumor-antenna path (cf. Fig. 12), hence a smaller demanded dynamic range. As an example, at 5.3GHz the required dynamic range is lower than 50dB. Additionally, considering the fact that the third harmonic of a square wave has an amplitude of 10dB less with respect to the fundamental (both transmitted signal and LO signal are square waves), a harmonic rejection of at least 40dBc results adequate.

The output buffer has the task of delivering -14 dBm to the 50Ω antenna load, while isolating the LO port of the receiver downconverter from the output port of the trans-

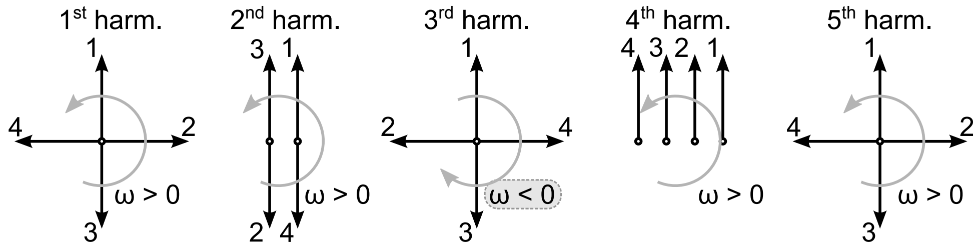

Figure 48: Phasor sequences of the harmonics of quadrature signals.

mitter. Moreover, it must filter out the harmonics of the transmitted signal, with special emphasis to the odd ones, that must be suppressed in excess of 40dBc in a wideband fashion. Achieving such a goal is not trivial at all. Using low-pass or band-pass filtering would require a high-order structure to get a steep roll-off and a high out-of band attenuation. Moreover, such a topology should be made programmable and able to automatically track the position of the harmonics in the frequency spectrum to attenuate them while leaving the desired signal pass through. A tunable notch filter, as the one in [60], could be an alternative solution. However, it would occupy a large silicon area due to the need of reactive components. Moreover, it would be extremely difficult to make it tunable over a multi-octave frequency range, not to mention that a single notch would only solve the issue with one specific harmonic tone. In addition, this solution suffers the overhead due to the need of automatic tuning and calibration.

The proposed harmonic rejection solution is simple, robust, wideband, and inductorless, thus compact. It is based on asymmetric poly-phase filters (PPFs). It leverages the quadrature signal sequence available at the output of the programmable frequency divider as follows. It is well known [8, 22] that PPFs are capable of discriminating between positive and negative frequency components, as they operate on sets of quadrature signals, that can be interpreted as complex signals. A quadrature sequence of phasors is called a forward sequence if each phasor leads the following one in the sequence, and a reverse sequence in case each phasor lags the next one in the sequence [8, 22]. Since the forward and reverse sequences are one the complex conjugate of the other, they can be interpreted as a set of positive frequency phasors and a set of negative frequency phasors, respectively. If the quadrature signals do not have sinusoidal waveforms, and yet they are evenly spaced in time, the fundamental tones make a forward quadrature sequence. Their harmonics, however, do not, in general. As shown in Fig. 48, the second harmonics make a differential sequence, the fourth harmonics make a common-mode sequence, and only the fifth harmonics make another forward quadrature sequence. More importantly, the third harmonics make a reverse quadrature sequence, that is if the fundamental is at the positive frequency $+\omega$, the third harmonic is at a negative frequency: -3ω. A PPF can thus be used to let the fundamental through while notching out the third harmonic.

The schematic of the harmonic rejection buffer is shown in Fig. 49. A three-stage PPF is designed to achieve broadband operation across PVT variations. The frequencies of the transmission zeros of the three RC sections are staggered as discussed in [8]. An attenuation in excess of 40dBc of the third harmonic is consistently achieved in the $6-16$GHz range, as shown in Fig. 50(a). A matrix of switches is embedded between the second and third stage of the PPF. This arrangement results in a double feature. On the one hand, the switches can be used to turn the transmitter off and perform loop-back calibration of

DC offsets, local oscillator feedthrough, and transmitter-receiver leakage, as described in [7]. On the other hand, it allows to reverse the signal phase sequence just before the last filter section. As a consequence of this sequence reversal, the higher frequency transmission zero is moved from the negative frequency axis to the positive frequency one, as shown in Fig. 50(b). This configuration enables the PPF to simultaneously attenuate the third and the fifth harmonics when the fifth harmonic is in-band. The capacitance is designed to be the same ($C = 150\mathrm{fF}$) in the three sections of the PPF. However, it is slightly decreased in the third section to take into account the parasitic capacitances of the switches (see Fig. 49). To make the operation of the switches maximally effective, 1pF coupling capacitors and 10kΩ resistors are used to set the DC bias voltage at the source/drain of the switch transistors to ground.
The PPF is driven by a regenerative buffer, similar to the one described in Sec. 3.3.2,that ensures isolation between the downconverter LO port and the transmitter output port. Since the required output power is not very high, the pass-band losses provided by the three-section wideband PPF can be tolerated. Finally, by connecting together the output terminals associated to quadrature signals, signal currents are summed (see Fig. 49): the fundamental tone is reinforced by 3dB, while the second harmonic is suppressed.

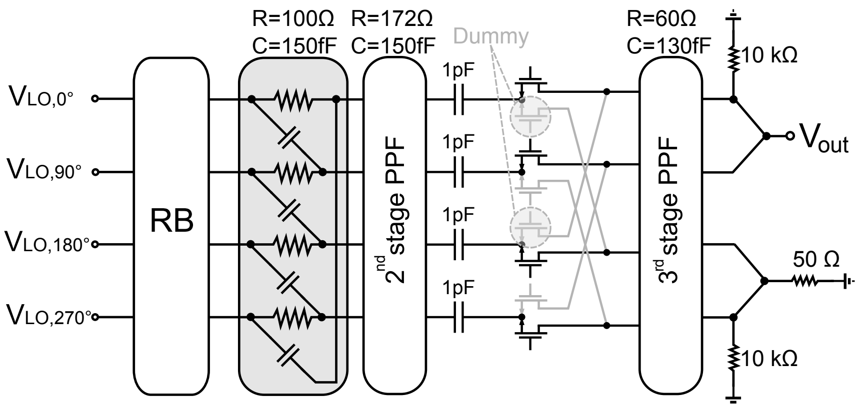

Figure 49: Schematic of the proposed harmonic rejection output buffer.

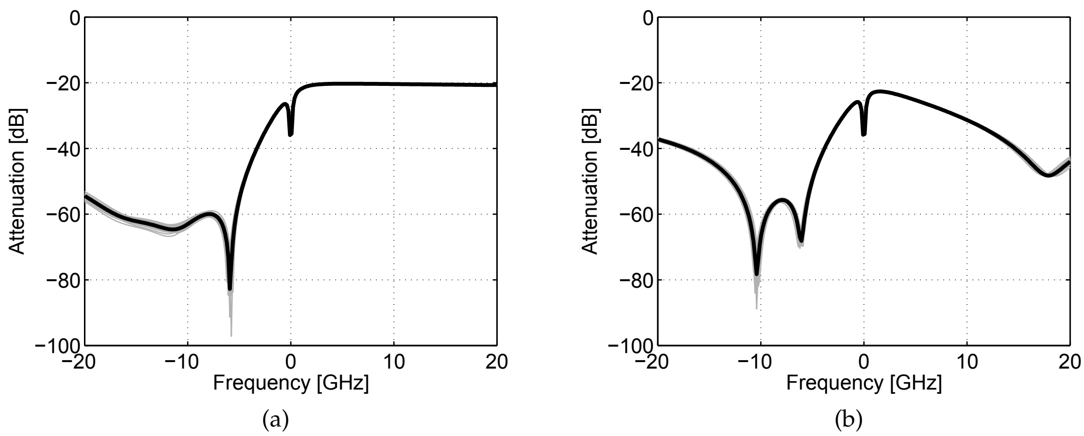

Figure 50: Simulated (nominal along with 50 Monte Carlo instances) transfer function of the reconfigurable PPF: (a) configuration to suppress 3^{rd} harmonic (b) configuration to suppress both 3^{rd} and 5^{th} harmonics (used when 5^{th} harmonic is in-band).

4 MEASUREMENT SETUP

SKuRAD1 and SKuRAD2 are realized in a 65nm CMOS technology. They implement a receiver and a complete transceiver for a Stepped Frequency Continuous Wave Radar, respectively. As a consequence of the system complexity, some control signals need to change during one measurement (for example when the divider has to change the division modulo or when the PLL changes frequency). For this purpose, a shift register of more than 100 bits is implemented in each IC. This allows us to simply set the configuration bits, bias currents and DC voltages of each block. The register programming, the data acquisition and the imaging generation is made possible thanks to a dedicated full-custom measurement setup.

This chapter is organized as follows. Section 4.1 describes the PCB used to program the shift register, measure the TIAs output and transfer the measurement data to a personal computer. Section 4.2 describes the 2-axis mobile frame used during the imaging experiments to move the target and obtain an ISAR configuration. Finally, Section 4.3 describes the dedicated management software and the communication protocol for the PC-μC data exchange.

The author implemented the entire measurement setup, including the design and implementation of any circuit and PCB, as well as any mechanical and firmware/software realization (both for microcontroller and for PC).

4.1 FULL CUSTOM CHIP PROGRAMMING AND ACQUISITION SYSTEM

The complexity of the complete system led to the realization of a full-custom board to simplify the measurements. The proposed board has been extensively used both for the electrical characterization and the imaging experiments. It makes it possible to program the ICs, measure the baseband signal, and move the target through a GUI running on a laptop.

The main feature of the PCB is a commercial 2-channels 31-bit $\Delta\Sigma$ ADC from Texas Instruments (ADS1282). It features a chopped input PGA and a total SNR of 130dB. Due to the high dynamic range of this component, the layout of the PCB is critical. To cope with the co-presence of both the microcontroller and the high accuracy ADC, the analog and digital grounds have been carefully separated. Moreover, no switching traces (with

the exception of the ADC clock and SPI) have been placed near the converter. Even the μC firmware has been optimized, since no data communication is allowed during an ADC conversion. The measured ADC SNR of 130dB demonstrates the effectiveness of the board layout.
Another feature of the board, which is visible in Fig. 51, is the presence of an ATMEGA32 microcontroller used to program the shift register, drive the stepping motors and communicate with the PC through an RS232 interface. An input/output level translator and an programming input connector completes the board.

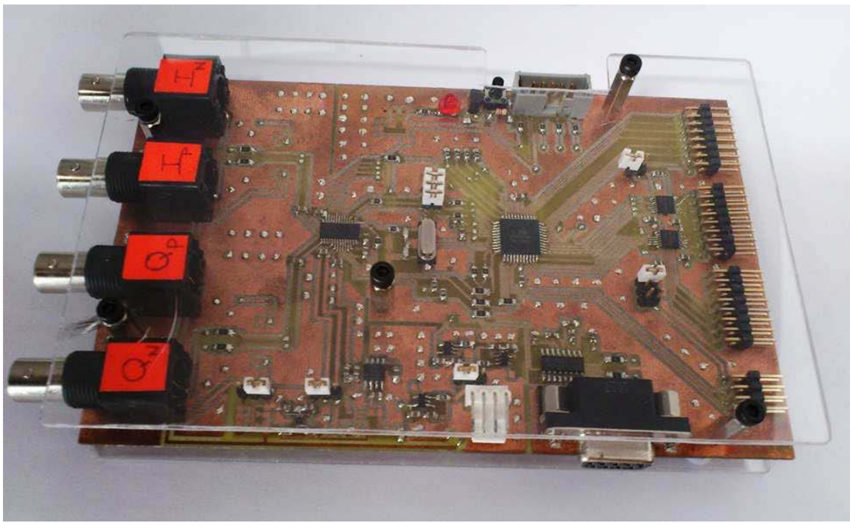

Figure 51: Proposed full custom board containing a μC, an ADC and a serial interface.

4.2 2-AXIS MOBILE FRAME FOR ISAR CONFIGURATION

A synthetic aperture radar (SAR) generates a high resolution image of the illuminated scene by performing a set of measurements at different antenna positions. This increments the effective array dimension, thus increasing the system resolution. In the opposite way, an inverse synthetic aperture radar (ISAR) obtains the same results by moving the target instead of the antenna. However, for both configurations, something able to move accurately either the antenna or the target is needed.
This section presents a 2-axis mobile frame used to move the target in the $x-y$ plane. It is completely made of aluminium with the exception of the wood support which reduces the backscatter near the target. Its dimension is approximately 60x45cm with an effective span of approximately 30x20cm. High accuracy and repeatability are needed to obtain a high resolution image. Hence, the wood support is moved by two high-precision stepper motors through screws and nuts. Due to the screw thread of 1mm/revolution, the ideal accuracy of the system is 2.5μm with a half-step motor driving. Hovewer, the medium-quality of the mechanical parts (not dedicated and expensive lead screws/ball screws have been used) is the main factor that limits the overall accuracy. Hence, a total resolution of $100-200$μm is estimated.
The general purpose I/O pins of the ATMEGA32 cannot drive the motors directly. Thus, a motor driver board has been realized using a TB62206. This PCB is capable to drive the motors with 35V and up to 1.5A/phase, more than enough for the intended applica-

tion. Fig. 53 shows the complete measurement setup including the ADC/µC board, the 2-axis mobile frame and the motors driver board.

4.3 MANAGEMENT SOFTWARE, COMMUNICATION PROTOCOL AND DATA FLOW

The high complexity and reconfigurability of SKuRAD1 and SKuRAD2 requires more than 100 configuration bits. The ADC board presented in Section 4.1 was realized with the intent of simplifying the measurement setup, but, the large number of possible configurations makes it unmanageable if the board is controlled by either a laboratory instrument or a generic software.
To simplify the measurement procedure, a dedicated software has been realized which manages the ADC board and the mobile frame. It is programmed using Visual Basic 6.0 and is fully configurable. Fig. 54 shows the main page of the proposed software. The main features are listed below

- Simple connection with the ADC board through the RS-232 interface
- Fast and simple setting of bias current and voltage of each SKuRAD1/SKuRAD2 block
- ADC control and automatic calibration
- Mobile frame control
- Automatic measurement for the image generation
- VNA control feature, allowing a VNA image generation

To prevent data loss between PC and microcontroller, a simple communication protocol is implemented. Each data exchange must be allowed by the PC and begins with the transmission of a command (CMD) followed by some optional parameters. The µC receives the packet, executes the command and, if required, transmits the result back to the PC. The µC-execution completes with the transmission of the execution-done command (CMD-done). At this point, the PC receives the execution-done command (and some other optional results), executes the requested routine (eg. ADC data visualization, update of the mobile frame coordinates, calculation of the new frequency point, ecc...) and closes the transmission. If no data is received back from the µC within 2/3 seconds from the transmission of CMD, a timeout occurs and the command is transmitted another time. A simple flow-chart of the communication protocol is visible in Fig. 55.

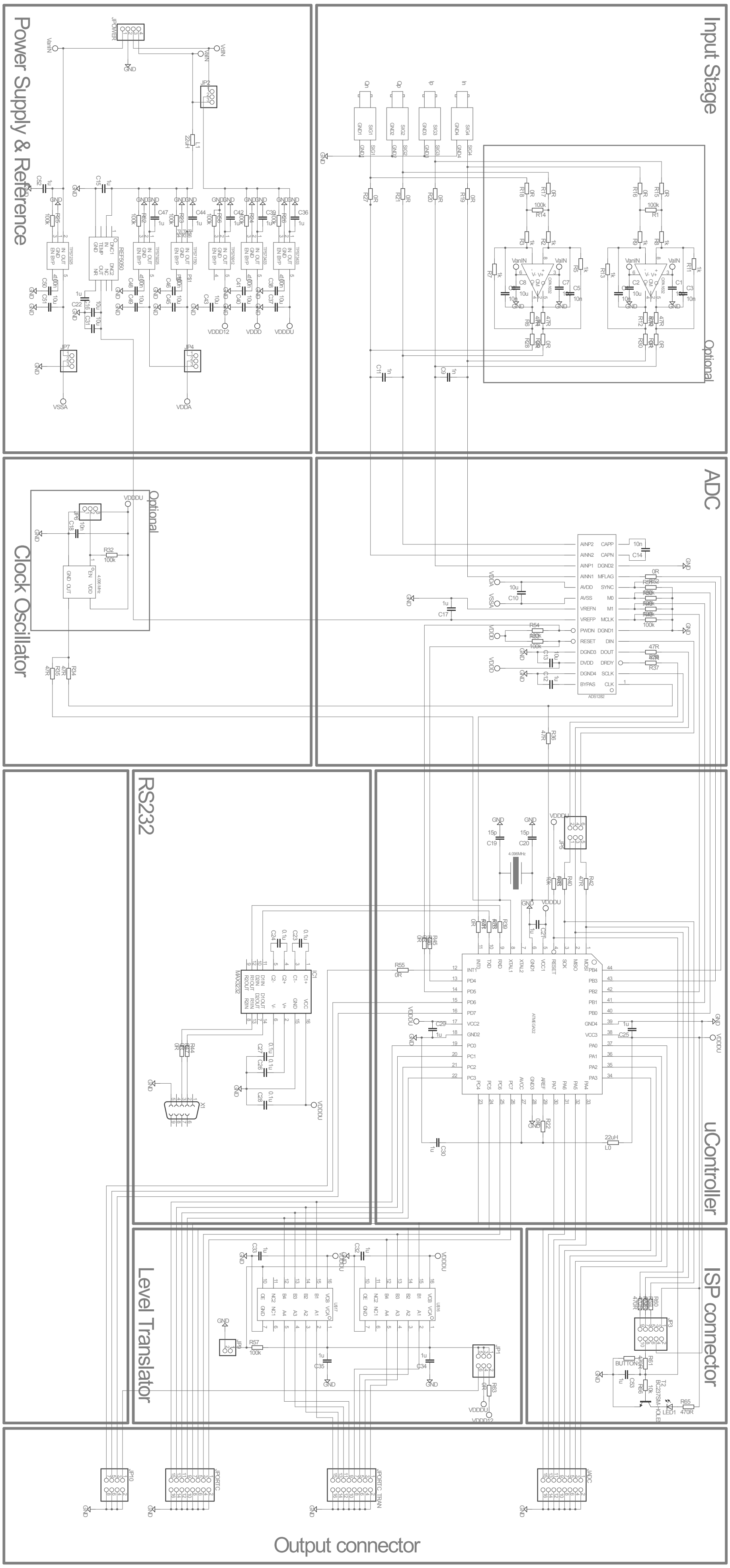

Figure 52: Schematic of the proposed PCB.

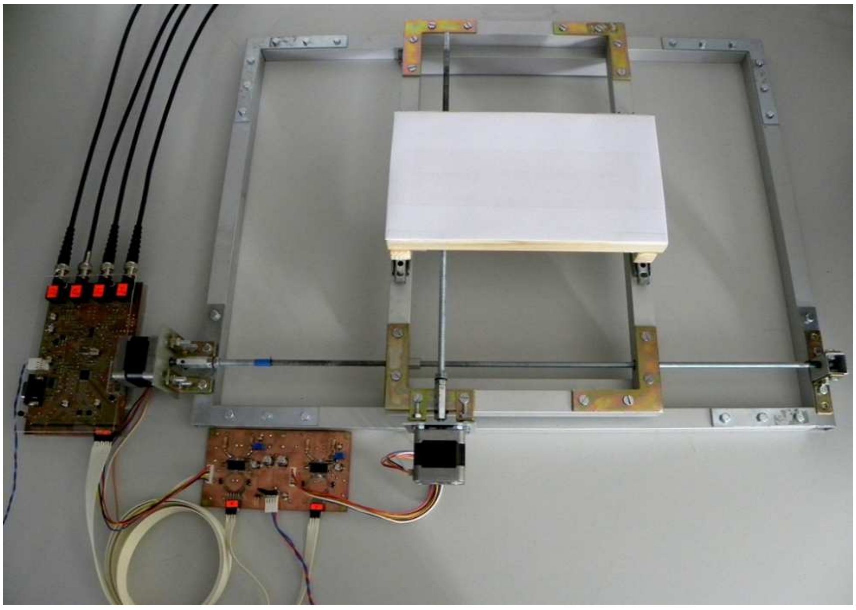

Figure 53: Photograph of the proposed measurement setup.

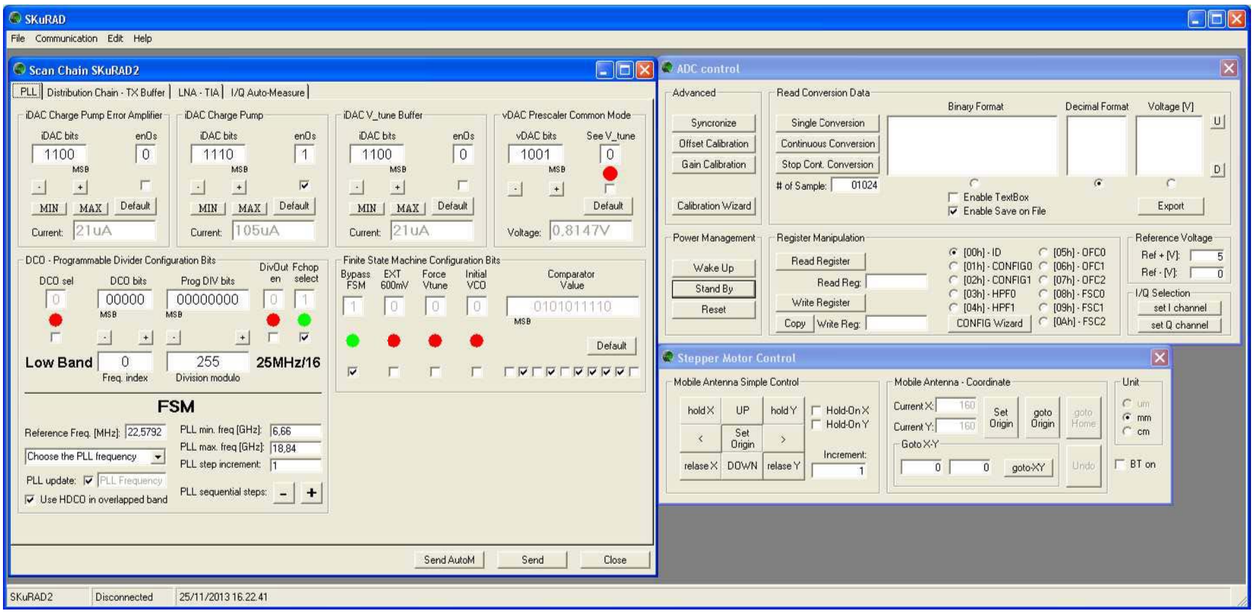

Figure 54: Screenshot of the main page of the measurement software.

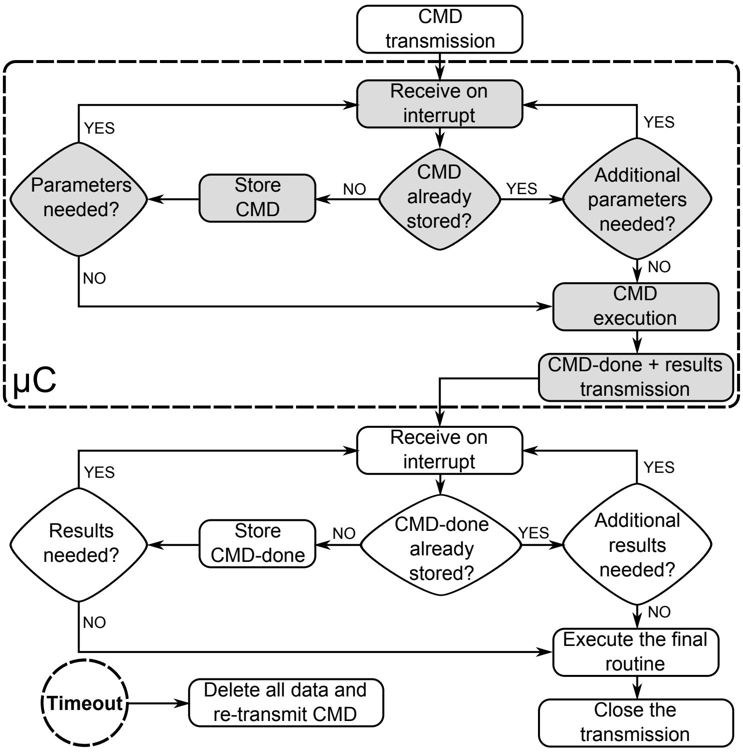

Figure 55: Flow chart of the implemented communication protocol. A gray background refers to μC routines, while a white background refers to PC instructions.

5 MEASUREMENT RESULTS

5.1 ELECTRICAL CHARACTERIZATION

5.1.1 *SKuRAD1 Measurements*

This section presents the electrical characterization of the first prototype of the radar tailored for the breast cancer diagnostic imaging, named SKuRAD1. It is implemented in a $65nm$ CMOS technology from ST Microelectronics and occupies an area of $1x1.2mm^2$ including PADs. It is composed by a wideband 3-stage LNA, a quadrature downconverter, 2 chopper Transimpedance Amplifiers (one for each I/Q path) and a programmable frequency divider which generates the quadrature LO signals from 1.75 to $15GHz$. The prototype includes also other blocks, like input and output test buffers and VCOs, that are implemented only for test purposes. The chip microphotograh is shown in Fig. 56(a). Unless otherwise noted, the main measurement setup is as follows. The chip is mounted with the chip-on-board technology on a Rogers RF PCB. All PADs are bonded, excluding LNA and test buffer inputs. RF measurements have been done with the aid of a RF-probe station capable of measuring up to $18GHz$ (the upper frequency is limited by the cables). GSG probes are manufactured by |Z|PROBE and are characterized up to $40GHz$. TIA's low-frequency outputs have been connected to an external low noise amplifier (LeCroy DA1855A) which performs the differential-to-single ended conversion and is capable of driving the low 50Ω input impedance of the spectrum analyzer.
This section is organized as follows. Sec. 5.1.1.1 presents the biasing condition and the power consumption of each block. Sec. 5.1.1.2 and 5.1.1.3 present the performance of the system in terms of conversion gain and overall noise. Finally, Sec. 5.1.1.4 introduce the linearity measurements followed by Sec. 5.1.1.5 which presents the I/Q imbalance of the receiver.

5.1.1.1 *DC Power Consumption*

SKuRAD1 chip is powered by a 1.2V power supply. Without taking into account the contribution of input and output test buffers, it consumes $124mW$. A detailed breakdown of the power consumption is presented in Tab. 2.

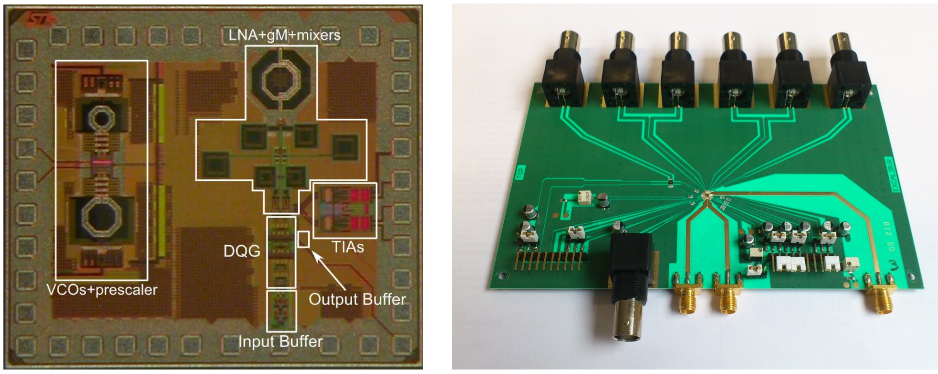

(a) (b)

Figure 56: Microphotograph of SKuRAD1(a) and PCB used to perform the measurements (b).

Table 2: SKuRAD1 DC power consumption

	DC Current [mA]	DC Power [mW]
LNA	34	40.8
G_m	16	19.2
TIAs	2	2.4
DQG	51	61.2
Buffer_{OUT}	3.5	4.2
Buffer_{IN}	58	69.6

5.1.1.2 *Conversion Gain and Noise Figure*

The conversion gain (CG) and noise figure (NF) have been measured with the aid of Agilent E4407B Spectrum Analyzer and Agilent E8257D/N5183A as RF signal generators. The input matching has been measured with an Agilent E8361A Vector Network Analyzer.

Conversion gain, noise figure and LNA input matching are reported in Fig. 57(a) versus the entire frequency range of interest. The CG is as high as 31dB while the $|S_{11}|$ is always lower than -9dB. The NF spans from 6.4dB to 8.6dB with an average value of 7.6dB. A plot of the conversion gain as a function of the intermediate frequency is reported in Fig. 57(b) for the three different modes of operation of the DQG. In any case, the baseband bandwidth, limited by the TIA, is 800kHz.

5.1.1.3 *Flicker Noise*

The $1/f$ noise is a potential show-stopper in this system, due to the extremely narrow baseband bandwidth and the direct-conversion architecture. The $1/f$ noise corner frequency has been measured with the aid of an external ADS1282 ADC. The ADC is an oversampling converter, and it embeds both an anti-alias and a decimation filter. Consequently, it sets the noise bandwidth of the receiver to 1kHz. The chopper frequency has been selected to be 1MHz to avoid any aliasing (the ADC sampling frequency is 4.098MHz), and yet prevent noise folding. A plot of the measured input-referred noise power density is shown in Fig. 58. The flicker noise corner is as low as 40Hz. This un-

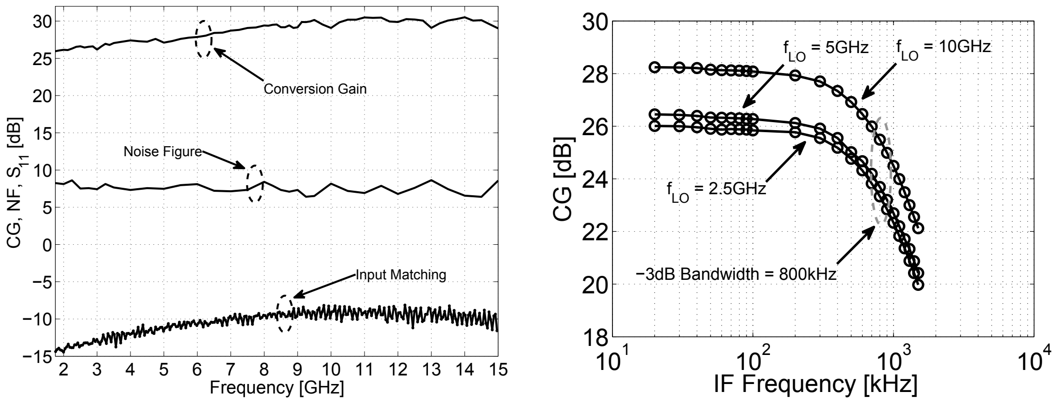

(a) (b)

Figure 57: SKuRAD1 measurement results: (a) conversion gain (CG), noise figure (NF) and LNA input matching ($|S_{11}|$); (b) conversion gain vs. intermediate frequency for the three DQG operation modes.

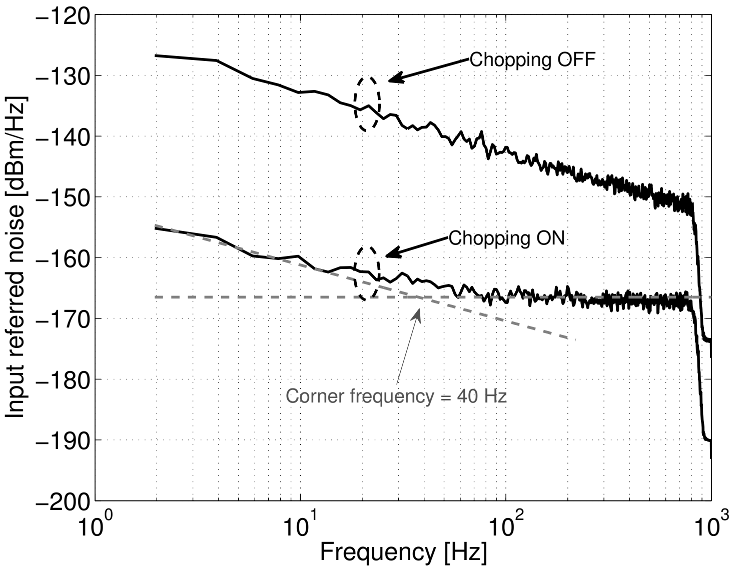

Figure 58: Measured receiver input-referred noise PSD with and without the chopper stabilization of the TIA. The LNA input is closed with a 50Ω load and the DQG is in the divide-by-two operation mode with an input frequency of 10GHz.

precedented result demonstrates the effectiveness of the chopped stabilization technique applied to a wireless direct conversion receiver. The input-referred noise, integrated over the 1kHz ADC band, and combined with the measured P_{1dB}, gives a dynamic range in excess of 106dB, showing that the performance of the proposed receiver is adequate to process simultaneously the strong skin backscatter and the weak echo from the tumor.

5.1.1.4 *Linearity*

Several linearity tests have been carried out. Fig. 59 shows the power of the first harmonic and the third order intermodulation with respect to the input power level. The two input tones have a frequency of $(7\text{GHz} + 60\text{kHz})$ and $(7\text{GHz} + 220\text{kHz})$ respectively and the third order intermodulation has a frequency of 100kHz.
The measured P_{1dB} as a function of the LO frequency is shown in Fig. 60. From 2 to

15GHz it is greater than −28dBm, well above the −34dBm maximum received signal that we expect from the analysis in Section 2.5.4.

Two-tone measurements are performed to assess the intermodulation performance of the receiver. Since medical imaging is performed in a screened environment, the required third-order intermodulation performance of the receiver is quite relaxed. However, although the desired signal is the only one being received, and although it is a purely sinusoidal tone, still there might be some spurious tones associated with it. Assuming the transmitted signal is generated by an integer-N PLL with a reference frequency of some 10MHz, some reference spurs might be there as undesired interferers. The spurious themselves would be out of the TIA band, and thus be filtered out, but their intermodulation product would corrupt the desired signal. To assess this scenario a two-tone test has been carried out with tones at 25 and 50.05MHz offset from the LO, for various LO frequencies. The IIP3 measured in this condition is reported in Fig. 60: it is greater than −12dBm across the LO frequency range. As a consequence, the maximum relative level of the PLL spurs (S_l) that can be tolerated is

$$S_l \leqslant \frac{3P_{RX} - 2IIP3 - P_d}{3} = -19\text{dBc}. \tag{24}$$

where $P_{RX} = -34\text{dBm}$ is the maximum signal we expect to receive, and $P_d = -134\text{dBm}$ is the maximum distortion we can tolerate to have a 100dB dynamic range. Clearly, the third-order intermodulation distortion performance of the proposed radar receiver results in very loose spurious specifications set on the radar transmitter.

As opposed to third-order intermodulation distortion, second order intermodulation is critical for the proposed direct-conversion receiver, as the skin backscatter acts as a strong in-band interferer. IIP2 has been measured setting the two tones such that both the tone frequencies and the intermodulation products fall within the TIA band. The result is shown in Fig. 60 for seven chip samples: the median value is 30dBm while the worst case is 22dBm.

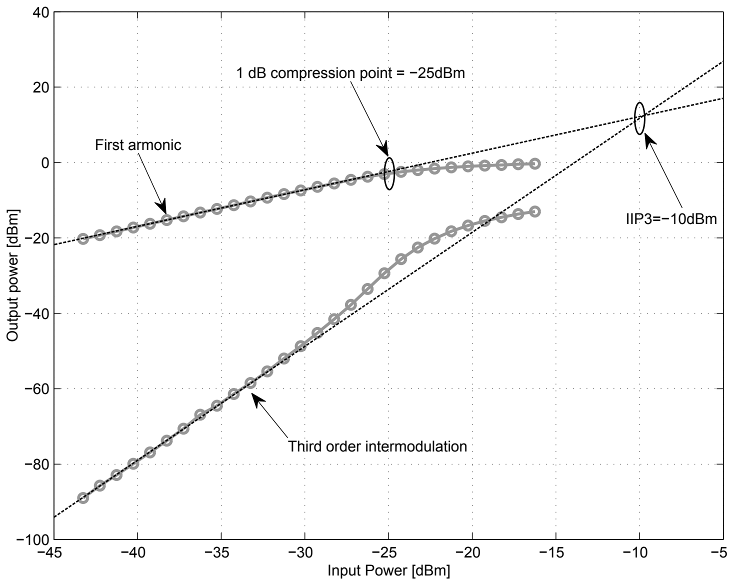

Figure 59: Measured output power of the first harmonic and 3rd order intermodulation versus input power.

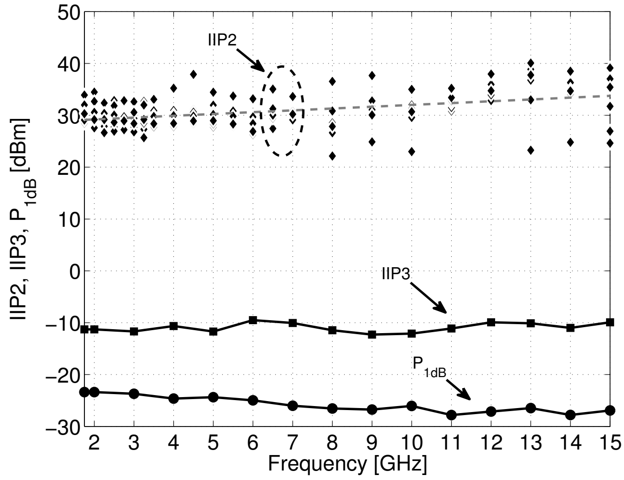

Figure 60: Measured P_{1dB}, IIP3 and IIP2 as a function of the LO frequency.

5.1.1.5 *I/Q Imbalance*

As discussed in Sec. 2.5, in a high-resolution imaging system, the quadrature phase and gain mismatches are very critical impairments. The measured I/Q phase and gain mismatches of seven samples are shown in Fig. 61 and have been measured after the TIAs (hence at IF frequency) with the aid of a high performance oscilloscope. The quadrature error is less than 1.5° across the entire band while the gain imbalance is lower than 0.8dB. In Fig. 61, note that a clear systematic gain mismatch is observed. Such a behaviour was tracked back to a layout error, resulting in a mismatch in the parasitic resistances of the input traces of the TIAs in the in-phase and quadrature paths. Once the systematic gain error is removed from the data in Fig. 61, the residual gain mismatch is limited to few tenths of dB. The good quadrature accuracy achieved over such a wide frequency range confirms that the proposed DQG is capable of excellent performance.

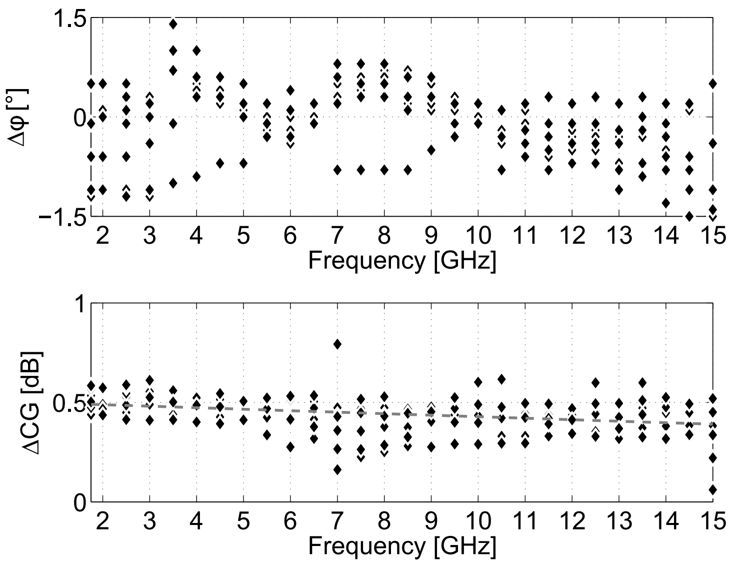

Figure 61: Measured quadrature phase error ($\Delta\phi$) and conversion gain mismatches (ΔCG) for 7 samples.

5.1.2 *SKuRAD2 Measurements*

This section presents the electrical characterization of the second prototype of the radar tailored for the breast cancer diagnostic imaging, named SKuRAD2. Like SKuRAD1, it is also implemented in a $65nm$ CMOS technology from ST Microelectronics and occupies an area of $1x1.3mm^2$ including PADs. It is the complete ultra-wideband transceiver, thus it is composed by the same receiver as in SKuRAD1 (as already discussed, only small changes have been made in the receiver chain), a new and improved version of the programmable frequency divider, an integer-N PLL which generates signals in the $8-16GHz$ range and a harmonic rejection output buffer. The chip microphotograh is shown in Fig. 62(a).

The measurement setup is quite similar to that used for SKuRAD1. This time each chip is mounted with the chip-on-board technology on a small FR4 PCB (Fig. 62(b)) which is then connected to a bigger PCB containing all the components and connectors. This solution allows us to save money since all the expensive components have been bought only once for the bigger board. All PADs are wire-bonded, excluding the LNA input and the TX output. RF measurements have been done with the aid of a RF-probe station capable of measuring up to $18GHz$ (the upper frequency is limited by the cables). GSG probes are manufactured by PICOPROBE and are characterized up to $40GHz$. TIA's low-frequency outputs have been connected to an external low noise amplifier (LeCroy DA1855A) which performs the differential-to-single ended conversion and is capable of driving the low 50Ω input impedance of the spectrum analyzer. Finally, a $22.5792MHz$ high performance crystal oscillator (CCHD-957) has been used as the PLL reference signal.

The section is organized as follows. Sec. 5.1.2.1 presents the biasing condition and the power consumption of each block. Sec. 5.1.1.2 presents the conversion gain and the noise figure of the modified receiver. Sec. 5.1.2.3 introduces the linearity measurements while Sec. 5.1.2.4 and Sec. 5.1.2.5 show the performance of the PLL in terms of tuning range, phase noise and spur level. Finally, Sec. 5.1.2.6 presents the fundamental and harmonic output power of the harmonic rejection TX buffer while Sec. 3.3.2.2 presents some simulations of the improved frequency divider.

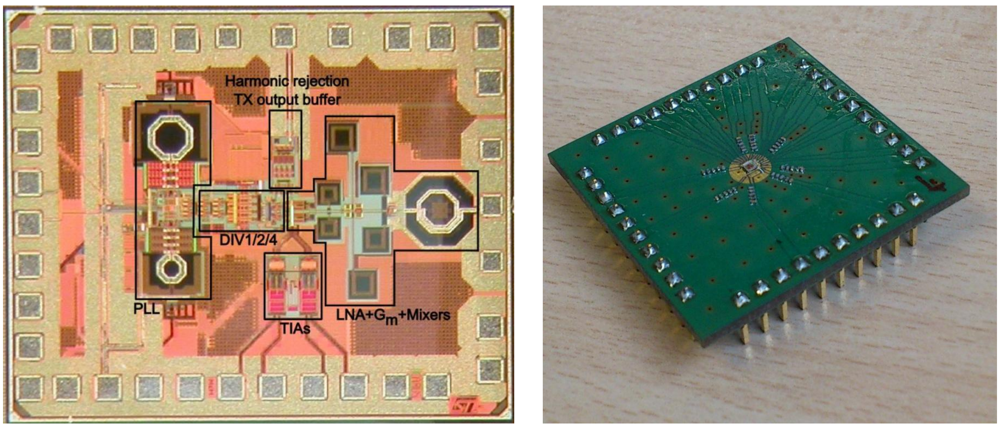

(a) (b)

Figure 62: Microphotograph of SKuRAD2(a) and PCB used to perform the measurements (b).

5.1.2.1 *DC Power Consumption*

SKuRAD2 is powered by a 1.2V power supply. In the worst case condition (i.e. at 16GHz with the frequency divider configured as a divider-by-1) it consumes 204mW. A detailed breakdown of the power consumption is presented in Tab. 3.

Table 3: SKuRAD2 DC power consumption

	DC Current [mA]	DC Power [mW]
LNA	28	33.6
G_m	20	24
TIAs	2	2.4
VCO_L	25	30
VCO_H	33	39.6
Prescaler	2.7	3.24
Div-N+PFD+CP	2.3	2.76
RBs+DIV1/2/4	69	82.8
TX output buffer	13	15.6

5.1.2.2 *Conversion Gain and Noise Figure*

The conversion gain and noise figure have been measured with the aid of Agilent E4407B Spectrum Analyzer and Agilent E8257D as RF signal generator. The input matching has been measured with an Agilent E8361A Vector Signal Analyzer.
Conversion gain, noise figure and LNA input matching are reported in Fig. 63 versus the entire frequency range of interest. The CG is 36dB with a maximum variation of 4.2dB. The −3dB IF bandwidth is 600kHz as depicted in Fig. 64. The variation of the IF bandwidth with respect to SKuRAD1 is related to an increment of the transresistance of the TIAs. The NF spans from 5.5dB to 8.4dB with an average value of 7dB.

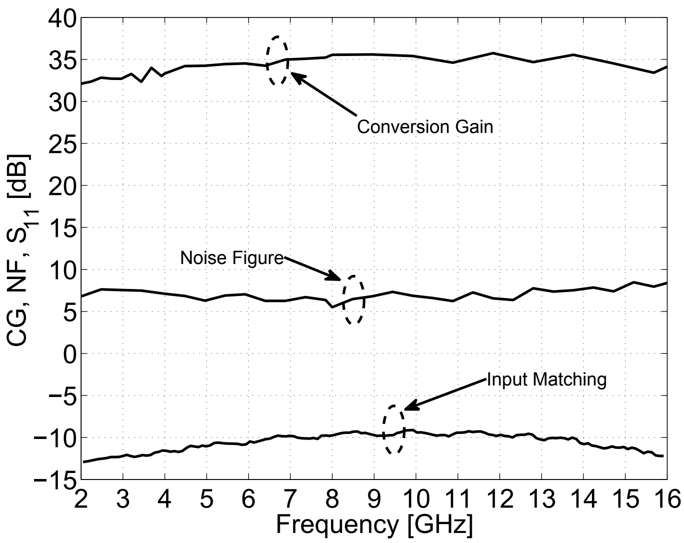

Figure 63: Conversion Gain (CG), Noise Figure (NF) and LNA Input Matching (S_{11}).

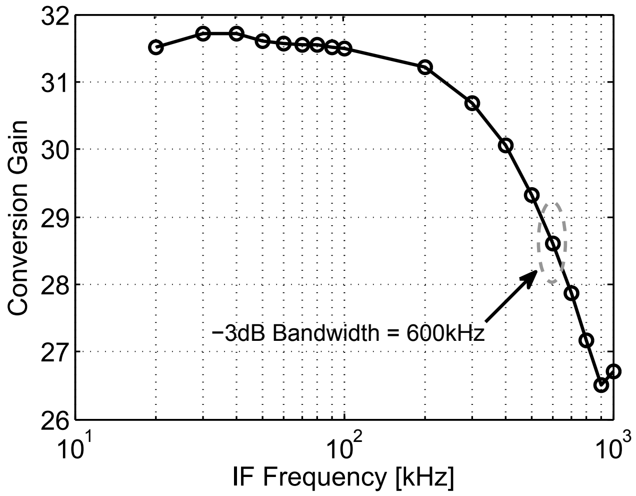

Figure 64: Conversion Gain vs. intermediate frequency @$F_{PLL} = 8GHz$ in the divide-by-4 operation mode.

5.1.2.3 *Linearity*

A two tone test has been carried out to report the linearity performances of the receiver. Fig. 65 shows the P_{1dB} and IIP3. The P_{1dB} is always better than $-28dB$ while the input-referred IP3 is better than $-13dBm$. The two input tones have a frequency of $f_{LO} + 30MHz$ and $f_{LO} + 60.050MHz$, well outside the baseband bandwidth, while their third order intermodulation has a frequency of 50kHz which falls inside the TIAs bandwidth. Additionally, Fig. 66 shows the IM3 as a function of the input power when the two tones are both outside (out-of-band IIP3) or inside (in-band IIP3) the TIAs bandwidth. In the last case, the tone frequencies are $f_{LO} + 60kHz$ and $f_{LO} + 220kHz$ with an intermodulation frequency of 100kHz.

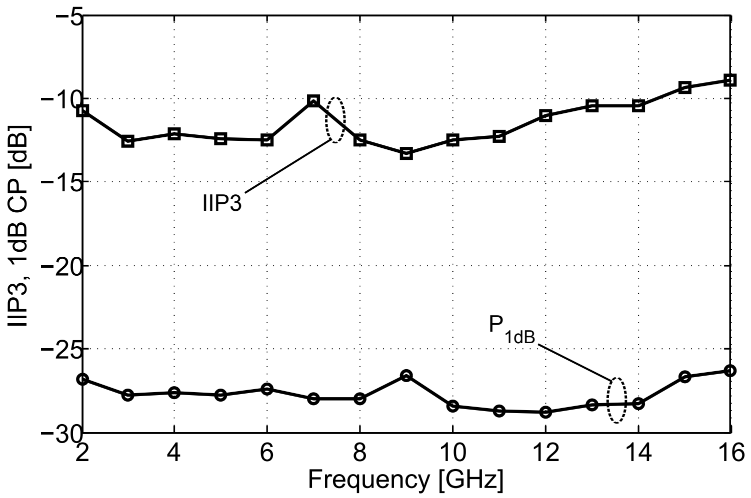

Figure 65: Measured P_{1dB} and out-of-band IIP3 as a function of the LO frequency.

5.1.2.4 *Phase Noise and Tuning Range*

The performance of the PLL have been measured after the programmable divider by 1/2/4 and the harmonic rejection TX buffer with the aid of Agilent E4407B spectrum analyzer. Due to the relatively low output power ($\approx -14dBm$), we used an external

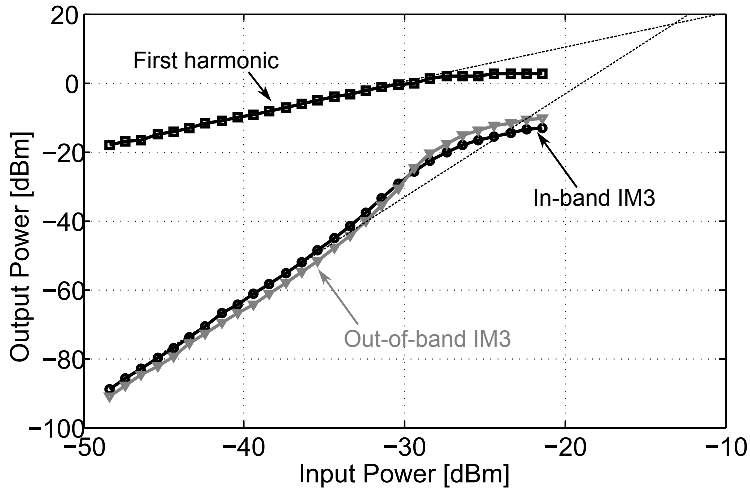

Figure 66: Measured fundamental and third harmonic intermodulation power as a function of the input power.

ZVA-183-S+ wideband amplifier to obtain an accurate measurement. The two VCOs tune from 6.5 to 13GHz and from 11 to 19.3GHz having an overall fractional tuning range of 99%. Fig. 67 shows the measured tuning range of the PLL. It covers with margin the designed bandwidth. Moreover, the 2GHz overlap between the two VCOs makes the design robust against PVT variations.

The VCOs phase noise @10MHz offset is visible in Fig. 68 over the entire frequency

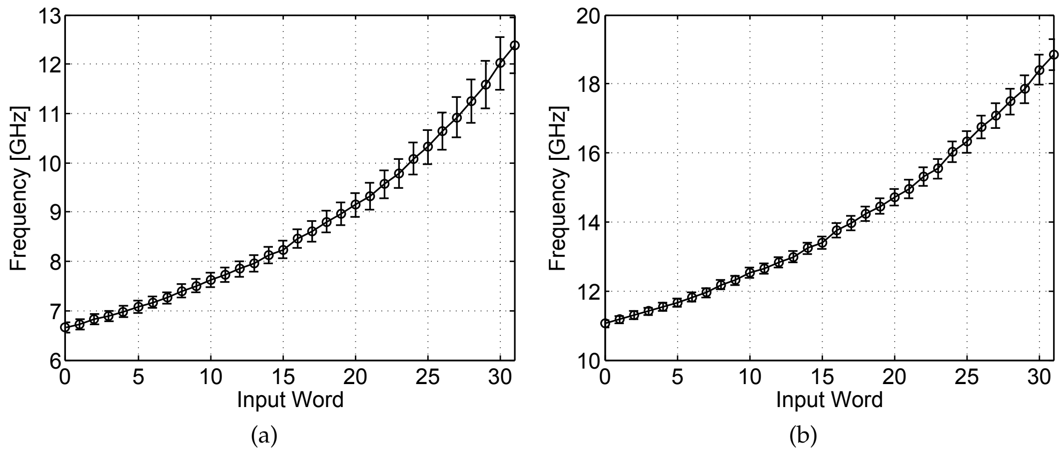

Figure 67: Measured tuning range of VCO_L(a) and VCO_H(b).

range. The offset frequency (10MHz) has been chosen well outside the PLL bandwidth (1MHz) where the VCO is approximately the only contributor to the PLL phase noise. Over the entire frequency range of interests (i.e. $8-16$GHz), the VCOs PN@10MHz offset is always better than -129dBc/Hz.

Fig. 69(a) shows the PLL phase noise for two different carrier frequencies. The RMS jitter integrated from 1kHz to 100MHz is 0.68ps(2.2°) and 0.52ps(2.4°) for the 9 and 13GHz carrier respectively. Fig. 69(b) shows the PLL phase noise for different division ratios. Here, the phase noise reduction of 6 and 12dB in the divide-by-2 and divide-by-4 operation mode is visible.

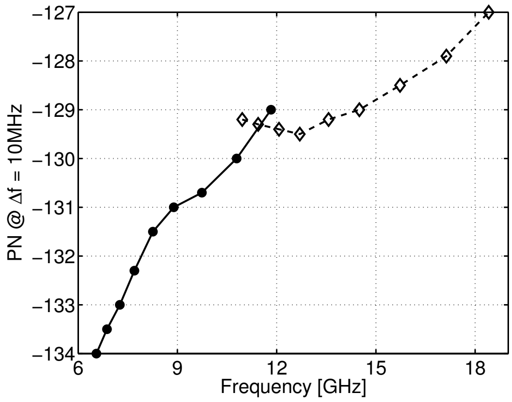

Figure 68: Measured phase noise of VCO_L and VCO_H. at 10MHz offset from the carrier. For this measurement, the chip has been powered with an external battery.

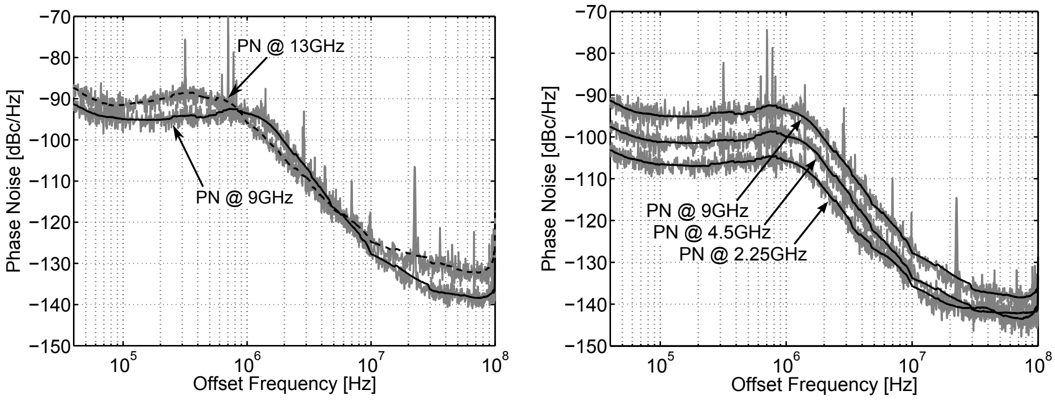

(a) (b)

Figure 69: Measured PLL phase noise for two different carrier frequencies (a) and for three different division ratios (b). For these measurements, the chip has been powered with an external power supply.

5.1.2.5 *Reference Spur and Settling Time*

The PLL spur level at different carrier frequencies and for different division ratios is visible in Fig. 70(a). The reference spur level is always better than −48dBc. An example of the PLL output spectrum is shown in Fig. 70(b). This has been measured for a carrier frequency of 12.7GHz and shows the worst case spur level.
The transient of the PLL tuning voltage is shown in Fig. 71. The PLL reaches the lock condition in approximately 2μs.

5.1.2.6 *Harmonic Rejection TX*

To verify the effective usefulness of the proposed transceiver in a breast cancer imaging tool, the output characteristics have been measured. The average TX output power is −14dBm (Fig. 72(a)) with a harmonic rejection in excess of 40dBc up to the fifth harmonic. Only the 4^{th} harmonic is less attenuated, but this is not an issue since it is intrinsically rejected by the receiver. As a proof, the measured 4^{th}-harmonic conversion gain is shown in Fig. 72(b). Finally, the switches in the TX buffer allow to suppress the first harmonic by more than 55dB, useful for the calibration process.

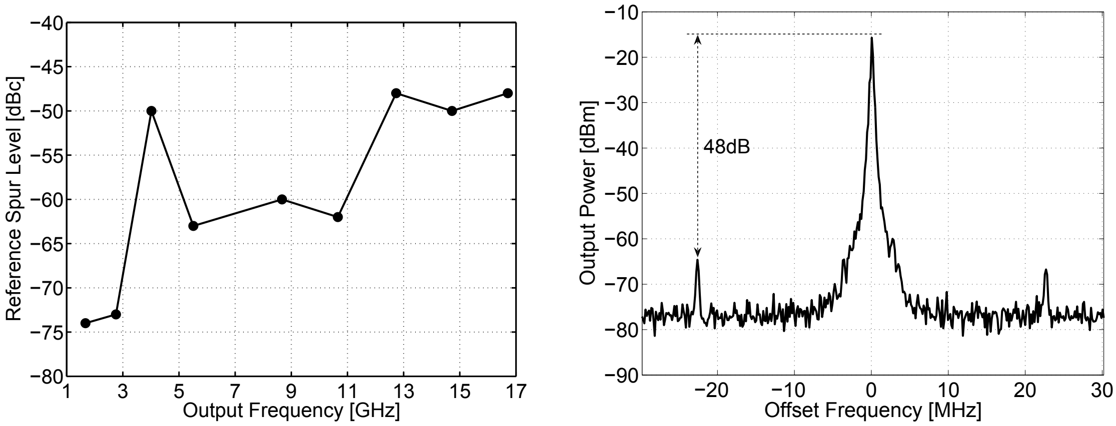

(a) (b)

Figure 70: Measured reference spur level as a function of the LO frequency (a) and Measured LO output spectrum at 12.7GHz (b).

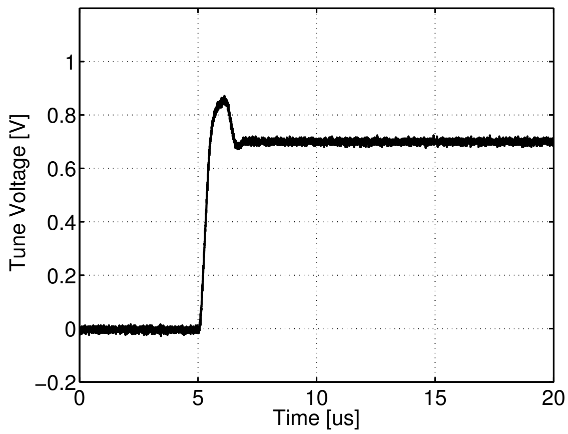

Figure 71: Measured PLL transient tune voltage.

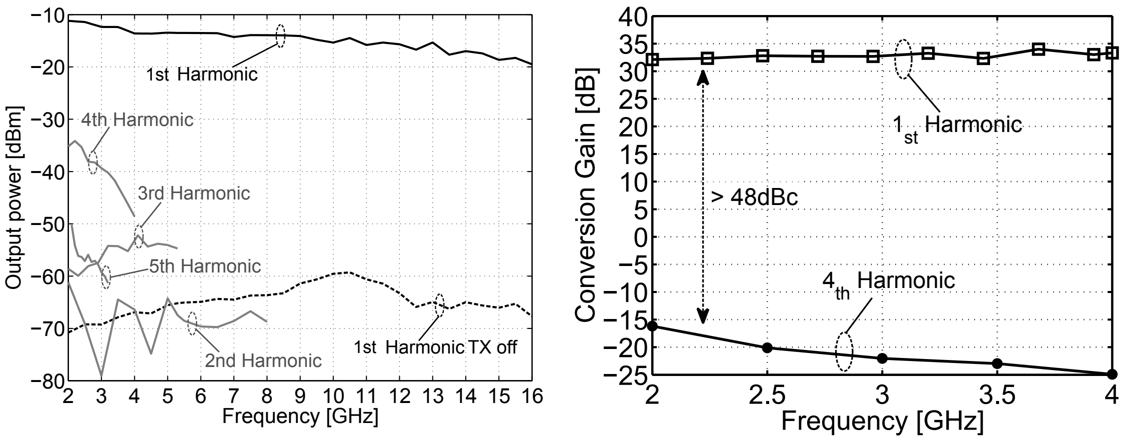

(a) (b)

Figure 72: Measured TX output power and harmonic rejection (a) and measured receiver 4^{th} harmonic conversion gain (b).

5.2 IMAGING EXPERIMENTS

As already described in Chapter 2, the final imaging system consists of an array composed by some elementary modules which can be organized to form different shapes. The single element of the array is made of the realized radar transceiver together with a TX and RX patch antennas. Although measurement results of the electric characterization of SKuRAD2 are in good agreement with the system analysis and constraints for the intended application, nothing has been done (up to now) to verify the effective usefulness of the proposed design in an imaging context.
This chapter proposes some imaging experiments able to proof the operation of the transceiver as an imaging tool. Experiments have been done with SKuRAD2 and a couple of wideband TX/RX patch antennas realized on the same Roger substrate. Due to the fact that RF pads have been probed, it was impossible to realize a real antenna array. As a consequence, we used a full custom 2-axis mobile frame (described in Sec. 4.2) to move the target obtaining an Inverse Synthetic Aperture Radar.
This section is organised as follows. Sec. 5.2.1 reports the design of the proposed wideband path antennas. Sec. 5.2.2 introduces some preliminary imaging experiments while Sec. 5.2.3 shows the imaging results using a realistic breast phantom that mimics the electro-magnetic proprieties of the real breast.

5.2.1 *Patch Antenna*

The design of the antenna structure that complements the integrated radar transceiver is based on two identical printed monopoles for transmission and reception functionality. The requirement for each antenna element of operating on the large wideband from 2 to 16GHz is achieved by means of a combined circular/rectangular shape of the radiating patches, as shown in Fig. 73. In particular, the semicircular part acts as a tapering section for better impedance matching all over the bandwidth to the 50Ω microstrip feeding line. In order to obtain a compact design, the two monopoles are placed very close to each other on the same face of the substrate. To minimize the unavoidable mutual coupling between the antennas, a T-shaped decoupling structure is introduced on the back of the laminate. The geometric parameters wd_1 and ld_1 control the isolation between the two radiating patches in the lower part of the operating band, namely, from 2 to 9GHz, while the geometric parameters wd_2 and ld_2 control the isolation in the upper part of the spectrum, for frequencies higher than 9GHz. Optimization of all the parameters was performed through simulation employing the CST Microwave Studio software.

A prototype of the antenna is shown in Figs. 73(b-d). The prototype was fabricated on a Roger RO4003c laminate, featuring a thickness of 1.524 mm, a dielectric constant of 3.55, and a loss tangent of 0.0027.

The antenna structure was experimentally characterized by using a two-port Agilent N5230A PNA-L network analyzer. The measured reflection and transmission coefficients of the two-element antenna are shown in Fig. 74 and compared to simulation results. The agreement between measurement and simulation is very good for frequencies below 8.5GHz, while at higher frequencies, discrepancies due to soldering and fabrication imperfections are clearly visible. In any case, the measured input matching is lower than -10dB over the entire frequency range of operation with the exception of a small hump at 2.9GHz ($|S_{11}| = -5$dB). Moreover, the antenna-to-antenna isolation is greater than 20 dB for frequencies higher than 3.3GHz, a performance that allows to directly connect the antenna structure to the integrated transceiver.

The simulated antenna radiation pattern on the magnetic plane ($x - z$ plane in Fig. 73, the plane facing the illuminated target) is shown in Fig. 75 for several frequencies. The radiation pattern is fairly omnidirectional, as required by the operation of the antenna within the array.

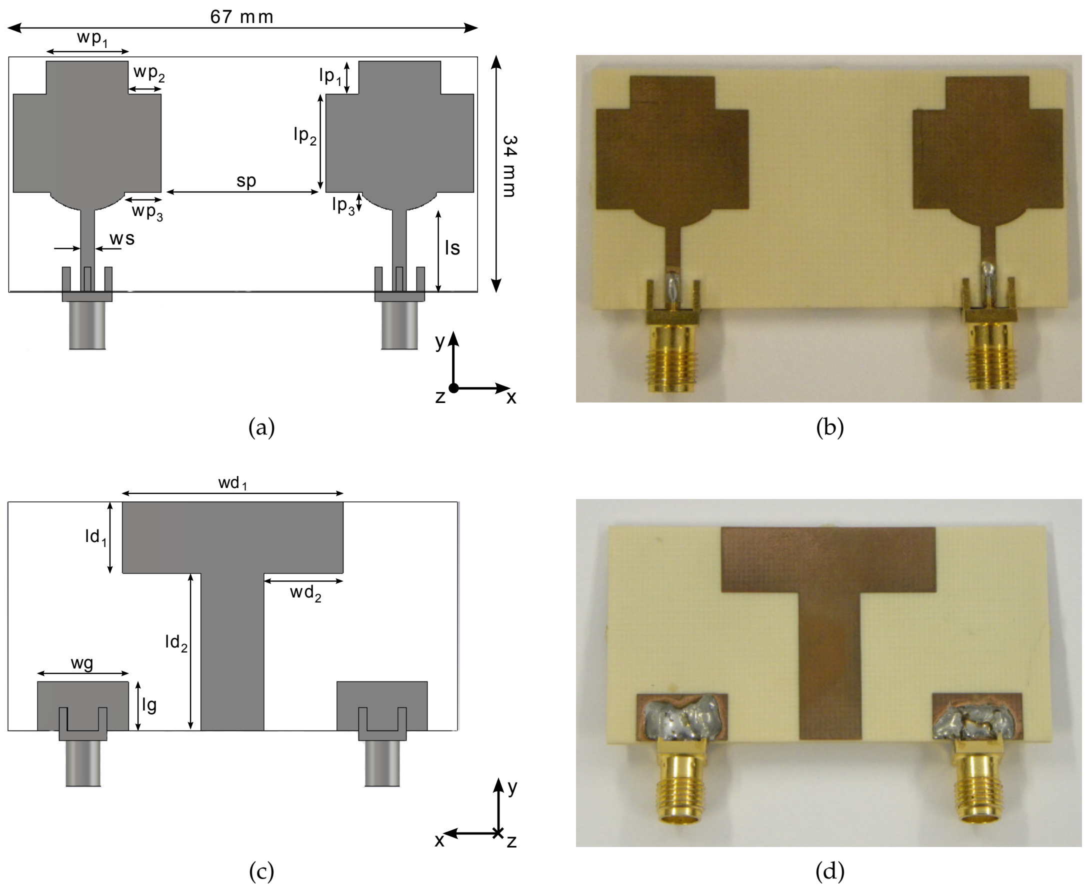

Figure 73: Layout of the antenna structure. Top layer with transmitting and receiving radiating elements (a-b) and Bottom layer with decoupling structure and partial ground plane (c-d). Dimensions are: $wp_1 = 10$ mm, $wp_2 = 4$ mm, $wp_3 = 4$ mm, $lp_1 = 4$ mm, $lp_2 = 12$ mm, $lp_3 = 2.1$ mm, $ws = 1.7$ mm, $ls = 9.9$ mm, $sp = 20$ mm, $wg = 11.5$ mm, $lg = 6.25$ mm, $wd_1 = 28$ mm, $wd_2 = 10$ mm, $ld_1 = 9$ mm, $ld_2 = 20$ mm.

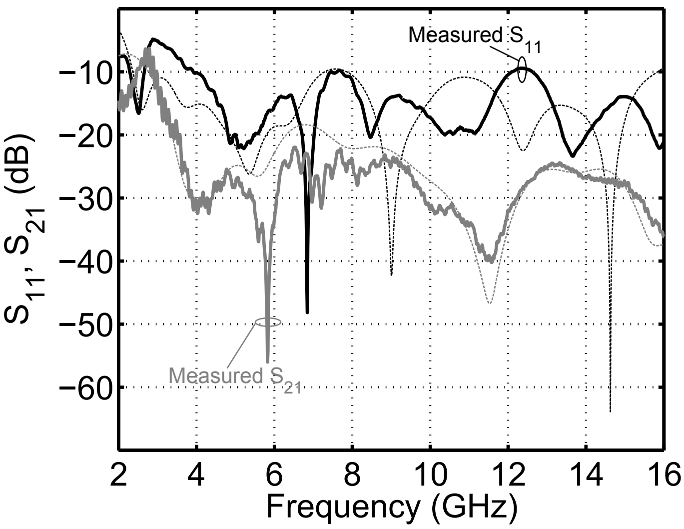

Figure 74: Measured (solid line) and simulated (dashed line) magnitude of reflection (S_{11}) and transmission (S_{21}) coefficients.

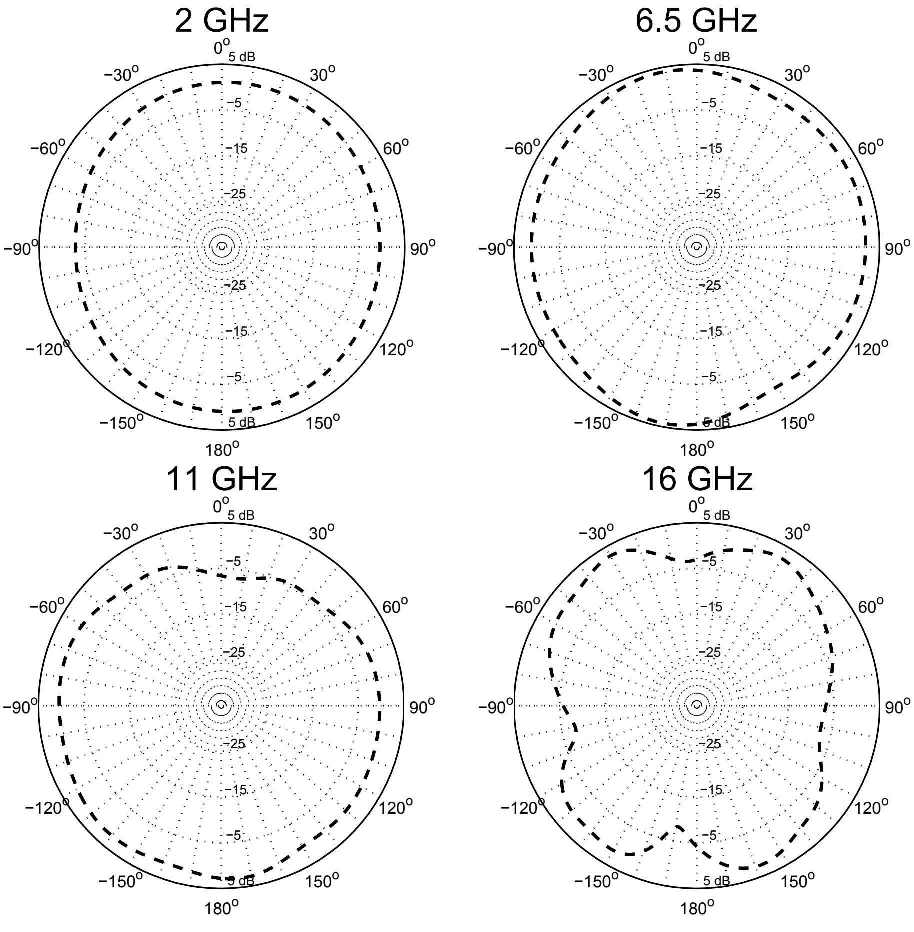

Figure 75: Simulated antenna radiation pattern on the $x-z$ plane (cf. Fig. 73).

5.2.2 *Preliminary Imaging Experiments*

Several tests have been carried out to assess the functionality of the presented integrated radar transceiver together with the planar antenna structure as an effective imaging tool.

As a first test of the correct operation of the system, the backscatter off a metallic plane is measured. The plane is displaced 4.1cm from the antennas and a full-span measurement, consisting of 155 frequency points, is performed. Fig. 76 shows the normalized synthetic time domain pulse obtained after an Inverse Fast Fourier Transform. The pulse duration of 63ps corresponds to a resolution of 9mm in the air and 3mm inside the body due to the reduced phase velocity [38]. Moreover, the peak centered at 275ps indicates the correct distance (two times the distance) between the antennas and the metal plane.
The metallic plane is then placed at different distances from the antennas to characterize the ability of the system to properly detect the distance. The measured displacement from a reference plane placed at 4.6cm away from antennas are shown in Fig. 77(a) and compared to ideal positions. The measurement accuracy is always better than 5mm, as highlighted in Fig. 77(b).
To complete the preliminary tests, a 3.5mm metallic bead has been used as a point scatterer to assess the ability of the radar to detect even small objects. The measurement setup used for this test is the same as in a real imaging context and therefore it will be explained in detail in the next section. The resulting point spread function is shown in Fig. 78. The absence of artifacts makes the transceiver suitable for the detection of small objects.

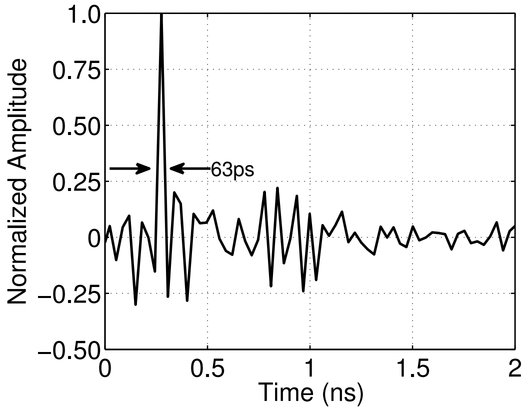

Figure 76: Measured synthetic time-domain pulse scattered off a metallic plane.

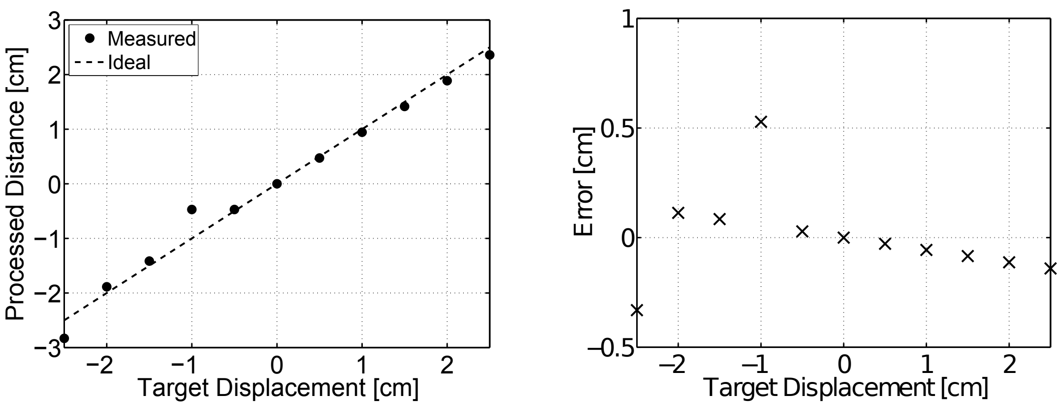

(a) (b)

Figure 77: Measured displacement of a metallic plane with respect to the reference plane (a) and measurement accuracy (b).

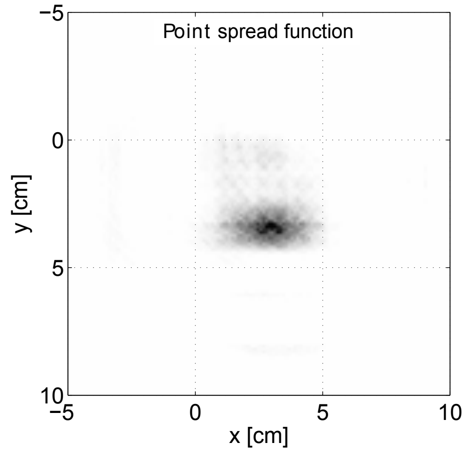

Figure 78: Measured radar image of a 3.5mm metallic bead. The $x - y$ plane is the same plane as the antennas.

5.2.3 *Breast Cancer Imaging Experiments*

This section describes in detail the procedures and results of a realistic breast cancer imaging experiment. For this purpose, a phantom mimicking the actual breast electrical proprieties is realized. It contains two small water-targets which emulate the neoplastic tissue. Results presented in Section 5.2.3.3 assert that the proposed radar transceiver can be effectively used as a breast cancer imaging tool.

5.2.3.1 *Breast Phantom*

Microwave imaging for breast cancer detection seeks to identify the presence and location of relevant tumor targets [20]. Accordingly, a physical breast phantom is realized to conduct experiments on breast cancer detection (Fig. 79). The phantom mimics the electrical properties of the breast tissues and tumors over a wide range of frequencies.
The material modeling the healthy tissue is a mixture of glycerine, double distilled/deionized water, ethylene glycol, polyethylene powder, and agar [5]. The recipe is easy to make, consistent, non-toxic and has been extensively tested over more than two years [5]. The absence of biological materials (pork fat, rabbit muscle, etc.) increments the lifetime of the phantom. Additionally, a bactericide can be used to prevent bacterial contamination.
Two enclosures of different diameters filled with tap water mimicking two tumor targets are buried inside the breast phantom. Tumor target "A" and "B" have a diameter of 6 and 9mm, respectively. With respect to the origin of the measurement setup, which is placed at the center of the phantom in the same $x - y$ plane of the antennas, tumor "A" and "B" are placed at coordinates ($x = -45$mm; $y = 30$mm; $z = 70$mm) and ($x = 15$mm; $y = 10$mm; $z = 70$mm) respectively.
The breast phantom is completely placed into a plastic container and its dimensions are, approximately, 11x11x3cm.

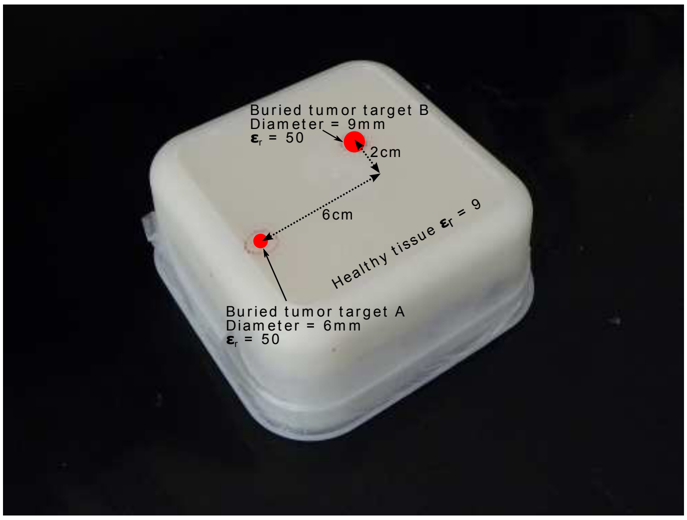

Figure 79: Photograph of the breast phantom placed in a plastic container.

5.2.3.2 *Measurement Setup and Calibration Technique*

A high resolution radar image is performed by transmitting a wideband pulse and receive the backscatter signal. In a stepped frequency continuous wave approach, however, a very short pulse is obtained by means of an IFFT over a set of narrowband measurements. The measurements accuracy is the key factor in determining the final resolution of the image. In this context, the measurement setup and data handling play a fundamental role.

In the proposed system, the transceiver is assembled in a chip-on-board fashion on a small FR4 PCB connected to a bigger board containing all the needed components and connectors. All pads are bonded, with the exception of RF pads, which are probed (Fig. 80(a)). The transceiver input (LNA) and output (TX buffer) GSG pads are connected through RF cables to the RX/TX antennas placed outside the shielded RF probe station and connected to a solid support. The breast phantom is placed on a wood plane support and moved by high-precision stepped motors over a custom metal frame, allowing an ISAR configuration. The higher the synthetic array dimension and number of measured points, the higher the cross-range resolution and processing gain [6] [28]. As a trade-off between accuracy and measurement time, we choose a synthetic array of $22\mathrm{cm}$ by $15\mathrm{cm}$ at $1\mathrm{cm}$ steps. For each of the $23\text{x}16 = 368$ positions, a set of 155 narrowband measurements, from 2 to $16\mathrm{GHz}$, are performed. The core of the measurement setup is the full-custom PCB described in Sec. 4.1. It is used to move the phantom in the $x-y$ plane, program the transceiver, measure the differential TIAs outputs and transmit the data to a laptop for the imaging generation. Notice that no data transfer occurs while the ADC is measuring. This avoids possible data corruption caused by the serial interface clock. Fig. 80(b) shows all the components here described while Fig. 81 shows the measurement setup during one imaging experiment.

In order to cope with the receiver and ADC offset, which are critical impairments for a direct conversion architecture, the measurement is made of two parts. First, the switch embedded in the transmitter polyphase filter is turned off. This allows to measure all the offsets due to components mismatch, local oscillator feedthrough, self mixing, and transmitter-to-receiver leakage through the substrate of the integrated circuit, as well as the ADC intrinsic offset. Second, the transmitter output buffer is turned on and the

scene is effectively illuminated. The first measurement is then subtracted from the second one to obtain a calibrated response.
A further calibration procedure is required to be able to discriminate the reflections due to the measurement setup and the surrounding environment. The procedure is similar to the "match/short" calibration usually performed on VNAs. A background acquisition (corresponding to the "match" measurement) is first carried out by performing a measurement with no target on the support. This data will be subtracted by the raw data obtained when the target is present. A metallic plane is then placed 4.6cm away from the antenna structure. This corresponds to a "short" measurement, and allows to identify the reference plane of the radar system [2].
Before obtaining a final image, a last calibration step is required. In fact, since the output of each antenna of the array is dominated by the large skin backscatter, it needs to be removed without corrupting the useful tumor signal. To do that, a calibration signal can be generated for each antenna by averaging the time response of any other antenna [40]. This signal is then subtracted from the raw data as explained in Sec. 2.4.

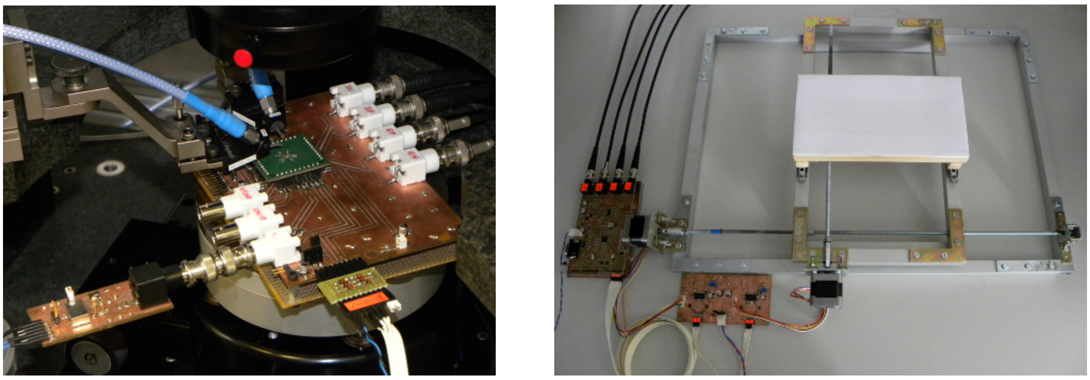

(a) (b)

Figure 80: SKuRAD2 housed in the RF probe station (a) and all the components of the measurement setup (b).

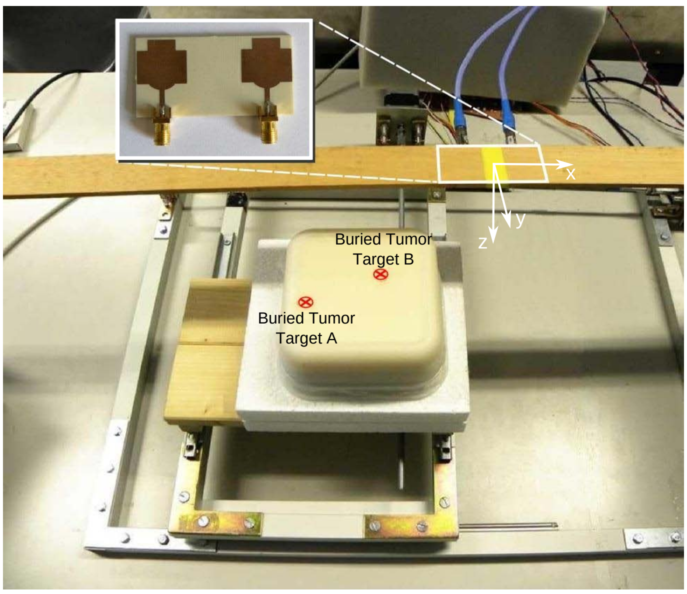

Figure 81: Photograph of the measurement setup during one imaging experiment.

5.2.3.3 *Imaging Results*

Using the measurement setup described in the previous section, a realistic breast cancer imaging experiment has been performed on the realized breast phantom. The target is placed on a wood plane moved by high-precision stepped motors and the antennas are installed on a rigid support over it. For each target position, the transceiver makes a full span measurement of the backscattered signals. Results are then transmitted to a personal computer and elaborated with Matlab.
A selection of significant images extracted by post-processing the raw data and corresponding to different planes are reported in Fig. 82. Fig. 82(a) shows the image of the $x-y$ plane at a distance $z = 7cm$ from the antennas. Dashed circles indicate the correct tumors positions. As shown, the two tumors are successfully detected, well confined and located at the correct position.
An image of the same plane obtained by using a commercial VNA in place of SKuRAD2 is reported in Fig. 82(b). The comparison between the obtained images shows that the last one is less confined and the tumors are not correctly located. This result may be affected by the lower dynamic range of the VNA with respect to SKuRAD2. In fact, taking into account the system dynamic range specification [1] together with the IF bandwidth and the transmitted power, the instantaneous VNA dynamic range results more than $20dB$ lower than SKuRAD2.
Fig. 83(a) shows the resulting phantom image over the $x-z$ cross section at $y = 10mm$. It clearly highlights the presence of tumor "B" while a shadow of tumor "A" is still visible due to its proximity in the y dimension. The measured radar image on the $y-z$ cross section for $x = 15mm$ is shown in Fig. 83(b). Only tumor "B" is visible in this case as tumor "A" is located $60mm$ away from the selected plane. However, a spurious trail of tumor "B" is also visible.
These results suggests that a dedicated high-dynamic range transceiver like SKuRAD2 can significantly improve the quality of the obtained image with respect to commercial VNAs, which are currently used in breast imaging system prototypes.

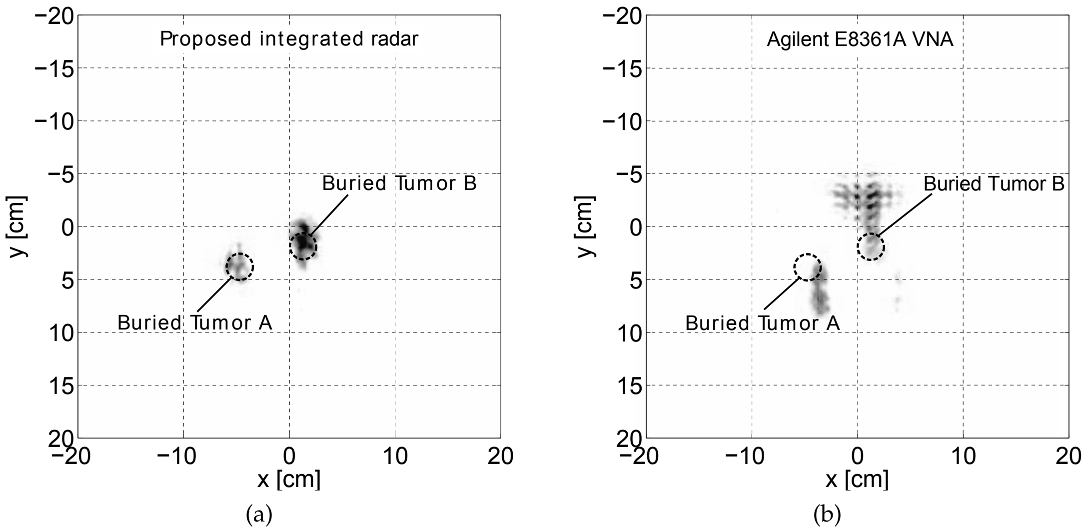

Figure 82: Measured radar image of the breast phantom with two buried tumors on the $x - y$ plane at a distance of 7cm from the antennas. (a) Image obtained with the proposed microwave radar. (b) Image obtained with a commercial VNA. The real A and B tumors location is indicated by dashed circles and is ($x = -45\text{mm}$; $y = 30\text{mm}$) and ($x = 15\text{mm}$; $y = 10\text{mm}$), respectively.

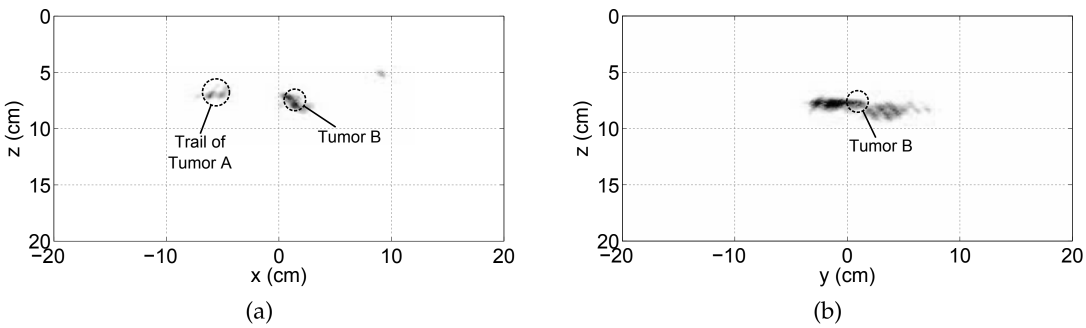

Figure 83: Measured radar image on the $x - z$ plane for $y = 1\text{cm}$ (a) and measured radar image on the $y - z$ plane for $x = 1.5\text{cm}$.

Part III

CONCLUSIONS

6 CONCLUSIONS

This PhD thesis presents the design of fully-integrated high-resolution radars. The work is focused on two different, but related, topics. The first concentrates on the feasibility study together with the design of an integrated UWB radar tailored for breast cancer diagnostic imaging. The second one, instead, focuses on the design of alternative building blocks for phased array radar able to improve the total system performance while reducing the area consumption.
This PhD thesis also focuses on the design of an IC capable of replacing the expensive laboratory instrument in a microwave imaging setup. The system specifications are obtained after a thorough system analysis. To achieve a resolution of $3mm$ inside the breast, the transceiver operates over 3 octaves, from 2 to $16GHz$. To be able to resolve the tumor backscatter, even in presence of the large skin reflection, it must feature a dynamic range in excess of $100dB$. Finally, since the imaging process is based on phase measurements, the I/Q phase error must be kept below $1.5°$ over the entire bandwidth. The transceiver is realized in a $65nm$ CMOS technology. The chip occupies an area of $1x1.3mm^2$ and consumes $204mW$ from a $1.2V$ power supply. The receiver features a conversion gain of $36dB$ with an average noise figure (NF) of $7dB$, a $1dB$ compression point $\geqslant -29dBm$ and a flicker noise corner of $30Hz$. The transmitter features an average output power of $-14dBm$, a minimum harmonic rejection $\geqslant 40dBc$ up to the fifth harmonic, a phase noise $\leqslant -109dBc/Hz@1MHz$ offset and an I/Q phase error lower than $1.5°$. Overall, the radar covers a bandwidth from 2 to $16GHz$ and achieves a resolution of $3mm$ inside the human body with a dynamic range of $107dB$.
Apart from the standard electrical characterization, several experiments have been carried out to assess the imaging performance of the system. The most important one consists of a real imaging experiment on a breast phantom containing two small targets. As a result, the system correctly detects the two targets and locates them in the correct position. This demonstrates that the proposed integrated radar can effectively replace the expensive laboratory instrument in a medical imaging context. To the best of my knowledge, the presented radar imager is the first full-custom integrated circuit dedicated to microwave imaging systems for medical applications, in particular for the breast cancer diagnostic imaging.
To conclude, this work presents the design of state-of-the-art integrated circuits for

fully-integrated high resolution radars. I hope that these efforts can effectively contribute to the design of systems able to improve the life quality and the health of people.

LIST OF PUBLICATIONS

CONFERENCE

1. Bassi, M.; Caruso, M.; Bevilacqua, A.; Neviani, A., "A $1.75 - 15GHz$ Stepped Frequency Receiver for Breast Cancer Imaging in $65nm$ CMOS", European Solid-State Circuits Conference (ESSCIRC), 2012 Proceedings of the

2. Caruso, M.; Bassi, M.; Bevilacqua, A.; Neviani, A., "A 2-to-16GHz $204mW$ $3mm$-resolution stepped-frequency radar for breast cancer diagnostic imaging in $65nm$ CMOS", Solid-State Circuits Conference Digest of Technical Papers (ISSCC), 2013 IEEE

3. Caruso, M.; Bassi, M.; Bevilacqua, A.; Neviani, A., "Wideband $2 - 16GHz$ Local Oscillator Generation for Short-Range Radar Applications", ESSCIRC (ESSCIRC), 2013 Proceedings of the

JOURNAL

1. Bassi, M.; Caruso, M.; Kahn, M.S.; Bevilacqua, A.; Capobianco, A.; Neviani, A., "An Integrated Microwave Imaging Radar With Planar Antennas for Breast Cancer Detection", Microwave Theory and Techniques, IEEE Transactions on (Volume:61 , Issue: 5), May 2013

2. Bassi, M.; Caruso, M.; Bevilacqua, A.; Neviani, A., "A $65 - nm$ CMOS $1.75 - 15GHz$ Stepped Frequency Radar Receiver for Early Diagnosis of Breast Cancer", Solid-State Circuits, IEEE Journal of (Volume:48 , Issue: 7), July 2013

BIBLIOGRAPHY

[1] *Agilent PNA Microwave Network Analyzers Data Sheet*. Agilent Technologies, 2009. URL "http://na.tm.agilent.com/pna".

[2] S.S. Ahmed, A. Schiessl, and L. Schmidt. A novel fully electronic active real-time imager based on a planar multistatic sparse array. *Microwave Theory and Techniques, IEEE Transactions on*, 59(12):3567–3576, 2011. ISSN 0018-9480. doi: 10.1109/TMTT.2011.2172812.

[3] Borivoje Nikolic A.M. Niknejad, Elad Alon and Jan Rabaey. Wafer scale distributed radio. Technical report, University of California, Berkeley, July 2009.

[4] A. Bakker, K. Thiele, and J.H. Huijsing. A cmos nested-chopper instrumentation amplifier with 100-nv offset. *Solid-State Circuits, IEEE Journal of*, 35(12):1877–1883, 2000. ISSN 0018-9200. doi: 10.1109/4.890300.

[5] Y. Baskharoun, A. Trehan, N.K. Nikolova, and M.D. Noseworthy. Physical phantoms for microwave imaging of the breast. In *Biomedical Wireless Technologies, Networks, and Sensing Systems (BioWireleSS), 2012 IEEE Topical Conference on*, pages 73–76, 2012. doi: 10.1109/BioWireless.2012.6172736.

[6] M. Bassi, A. Bevilacqua, A. Gerosa, and A. Neviani. Integrated sfcw transceivers for uwb breast cancer imaging: Architectures and circuit constraints. *Circuits and Systems I: Regular Papers, IEEE Transactions on*, 59(6):1228–1241, 2012. ISSN 1549-8328. doi: 10.1109/TCSI.2011.2173400.

[7] M. Bassi, M. Caruso, M.S. Khan, A. Bevilacqua, A. Capobianco, and A. Neviani. An integrated microwave imaging radar with planar antennas for breast cancer detection. *Microwave Theory and Techniques, IEEE Transactions on*, 61(5):2108–2118, 2013. ISSN 0018-9480. doi: 10.1109/TMTT.2013.2247052.

[8] F. Behbahani, Y. Kishigami, J. Leete, and A.A. Abidi. Cmos mixers and polyphase filters for large image rejection. *Solid-State Circuits, IEEE Journal of*, 36(6):873–887, 2001. ISSN 0018-9200. doi: 10.1109/4.924850.

[9] Essex J. Bond, Xu Li, S.C. Hagness, and B.D. Van Veen. Microwave imaging via space-time beamforming for early detection of breast cancer. *Antennas and Propagation, IEEE Transactions on*, 51(8):1690–1705, 2003. ISSN 0018-926X. doi: 10.1109/TAP.2003.815446.

[10] F. Bruccoleri, E.A.M. Klumperink, and B. Nauta. Wide-band cmos low-noise amplifier exploiting thermal noise canceling. *Solid-State Circuits, IEEE Journal of*, 39(2): 275–282, 2004. ISSN 0018-9200. doi: 10.1109/JSSC.2003.821786.

[11] M. Caruso, M. Bassi, A. Bevilacqua, and A. Neviani. A 2-to-16ghz 204mw 3mm-resolution stepped-frequency radar for breast-cancer diagnostic imaging in 65nm cmos. In *Solid-State Circuits Conference Digest of Technical Papers (ISSCC), 2013 IEEE International*, pages 240–241, 2013. doi: 10.1109/ISSCC.2013.6487717.

[12] C.T. Charles and D.J. Allstot. A buffered charge pump with zero charge sharing. In *Circuits and Systems, 2008. ISCAS 2008. IEEE International Symposium on*, pages 2633–2636, 2008. doi: 10.1109/ISCAS.2008.4541997.

[13] S. Chehrazi, A. Mirzaei, and A.A. Abidi. Noise in current-commutating passive FET mixers. *IEEE Transactions on Circuits and Systems I: Regular Papers*, 57(2):332 –344, feb. 2010. ISSN 1549-8328. doi: 10.1109/TCSI.2009.2023762.

[14] Jun-Chau Chien and Liang-Hung Lu. Analysis and design of wideband injection-locked ring oscillators with multiple-input injection. *Solid-State Circuits, IEEE Journal of*, 42(9):1906–1915, 2007. ISSN 0018-9200. doi: 10.1109/JSSC.2007.903058.

[15] C. Clemente. *Gray's Anatomy of the Human Body*. Lea and Febiger, 1985.

[16] C.C. Enz and G.C. Temes. Circuit techniques for reducing the effects of op-amp imperfections: autozeroing, correlated double sampling, and chopper stabilization. *Proceeding of the IEEE*, 84(11):1584 –1614, November 1996. ISSN 0018-9219. doi: 10.1109/5.542410.

[17] C.C. Enz, E.A. Vittoz, and F. Krummenacher. A cmos chopper amplifier. *Solid-State Circuits, IEEE Journal of*, 22(3):335–342, 1987. ISSN 0018-9200. doi: 10.1109/JSSC.1987.1052730.

[18] Shinichi Yamano et al. 76ghz millimeter wave automobile radar using single chip mmic. Technical report, Fujitsu Ten, 2004. URL `"http://www.fujitsu-ten.com/business/technicaljournal/pdf/23-2.pdf"`.

[19] E.C. Fear and M.A. Stuchly. Microwave detection of breast cancer. *Microwave Theory and Techniques, IEEE Transactions on*, 48(11):1854–1863, 2000. ISSN 0018-9480. doi: 10.1109/22.883862.

[20] E.C. Fear, Xu Li, S.C. Hagness, and M.A. Stuchly. Confocal microwave imaging for breast cancer detection: localization of tumors in three dimensions. *Biomedical Engineering, IEEE Transactions on*, 49(8):812–822, 2002. ISSN 0018-9294. doi: 10.1109/TBME.2002.800759.

[21] E.C. Fear, P.M. Meaney, and M.A. Stuchly. Microwaves for breast cancer detection? *Potentials, IEEE*, 22(1):12–18, 2003. ISSN 0278-6648. doi: 10.1109/MP.2003.1180933.

[22] M. J. Gingell. *The synthesis and application of polyphase filters with sequence asymmetric properties*. PhD thesis, University of London, London, 1975.

[23] A.H. Golnabi, P.M. Meaney, S. Geimer, and K.D. Paulsen. Microwave imaging for breast cancer detection and therapy monitoring. In *Biomedical Wireless Technologies, Networks, and Sensing Systems (BioWireleSS), 2011 IEEE Topical Conference on*, pages 59–62, 2011. doi: 10.1109/BIOWIRELESS.2011.5724347.

[24] D.M. Grimes and T.O. Jones. Automotive radar: A brief review. *Proceedings of the IEEE*, 62(6):804–822, 1974. ISSN 0018-9219. doi: 10.1109/PROC.1974.9520.

[25] T.M. Grzegorczyk, P.M. Meaney, P.A. Kaufman, R.M. di Florio-Alexander, and K.D. Paulsen. Fast 3-d tomographic microwave imaging for breast cancer detection.

Medical Imaging, IEEE Transactions on, 31(8):1584–1592, 2012. ISSN 0278-0062. doi: 10.1109/TMI.2012.2197218.

[26] T. Henriksson, M. Klemm, D. Gibbins, J. Leendertz, T. Horseman, A.W. Preece, R. Benjamin, and I.J. Craddock. Clinical trials of a multistatic uwb radar for breast imaging. In *Antennas and Propagation Conference (LAPC), 2011 Loughborough*, pages 1–4, 2011. doi: 10.1109/LAPC.2011.6114004.

[27] M.G.M. Hussain. Ultra-wideband impulse radar-an overview of the principles. *Aerospace and Electronic Systems Magazine, IEEE*, 13(9):9–14, 1998. ISSN 0885-8985. doi: 10.1109/62.715515.

[28] M.G.M. Hussain. Principles of space-time array processing for ultrawide-band impulse radar and radio communications. *Vehicular Technology, IEEE Transactions on*, 51(3):393–403, 2002. ISSN 0018-9545. doi: 10.1109/TVT.2002.1002490.

[29] National Cancer Institute. Surveillance, epidemiology, and end results (SEER) program research data (1975-2010), 2013. URL `http://www.seer.cancer.gov`.

[30] Y. Wo J. Effect of very small tumor size on cancer-specific mortality in node-positive breast cancer. *Journal of Clinical Oncology*, 2011. doi: 10.1200/JCO.2010.29.5907.

[31] W.D. Jones. Keeping cars from crashing. *Spectrum, IEEE*, 38(9):40–45, 2001. ISSN 0018-9235. doi: 10.1109/6.946636.

[32] Jung-Mu Kim, Donghoon Oh, Jeonghoon Yoon, Sungjoon Cho, Namgon Kim, Jeiwon Cho, Youngwoo Kwon, Changyul-Cheon, and Yong-Kweon Kim. In vitro and in vivo measurement for biological applications using micromachined probe. *Microwave Theory and Techniques, IEEE Transactions on*, 53(11):3415–3421, 2005. ISSN 0018-9480. doi: 10.1109/TMTT.2005.857116.

[33] P. Kinget, R. Melville, D. Long, and V. Gopinathan. An injection-locking scheme for precision quadrature generation. *Solid-State Circuits, IEEE Journal of*, 37(7):845–851, 2002. ISSN 0018-9200. doi: 10.1109/JSSC.2002.1015681.

[34] M. Klemm, I. Craddock, J. Leendertz, A. Preece, and R. Benjamin. Experimental and clinical results of breast cancer detection using uwb microwave radar. In *Antennas and Propagation Society International Symposium, 2008. AP-S 2008. IEEE*, pages 1–4, 2008. doi: 10.1109/APS.2008.4619673.

[35] M. Klemm, J.A. Leendertz, D. Gibbins, I. J. Craddock, A. Preece, and R. Benjamin. Microwave radar-based breast cancer detection: Imaging in inhomogeneous breast phantoms. *Antennas and Wireless Propagation Letters, IEEE*, 8:1349–1352, 2009. ISSN 1536-1225. doi: 10.1109/LAWP.2009.2036748.

[36] M. Klemm, D. Gibbins, J. Leendertz, T. Horseman, A.W. Preece, R. Benjamin, and I.J. Craddock. Development and testing of a 60-element uwb conformal array for breast cancer imaging. In *Antennas and Propagation (EUCAP), Proceedings of the 5th European Conference on*, pages 3077–3079, 2011.

[37] M. Lazebnik, M. Okoniewski, J.H. Booske, and S.C. Hagness. Highly accurate debye models for normal and malignant breast tissue dielectric properties at microwave

frequencies. *Microwave and Wireless Components Letters, IEEE*, 17(12):822–824, 2007. ISSN 1531-1309. doi: 10.1109/LMWC.2007.910465.

[38] Mariya Lazebnik, Dijana Popovic, Leah McCartney, Cynthia B Watkins, Mary J Lindstrom, Josephine Harter, Sarah Sewall, Travis Ogilvie, Anthony Magliocco, Tara M Breslin, Walley Temple, Daphne Mew, John H Booske, Michal Okoniewski, and Susan C Hagness. A large-scale study of the ultrawideband microwave dielectric properties of normal, benign and malignant breast tissues obtained from cancer surgeries. *Physics in Medicine and Biology*, 52(20):6093, 2007.

[39] D. Leenaerts, R. van de Beek, J. Bergervoet, H. Kundur, G. Van Der Weide, A. Kapoor, Tian Yan Pu, Yu Fang, Yu Juan Wang, B.J. Mukkada, Hong Sair Lim, V.M. Kiran, Chun Swee Lim, S. Badiu, and A. Chang. A 65 nm cmos inductorless triple band group wimedia uwb phy. *Solid-State Circuits, IEEE Journal of*, 44(12): 3499–3510, 2009. ISSN 0018-9200. doi: 10.1109/JSSC.2009.2032588.

[40] Xu Li and S.C. Hagness. A confocal microwave imaging algorithm for breast cancer detection. *Microwave and Wireless Components Letters, IEEE*, 11(3):130–132, 2001. ISSN 1531-1309. doi: 10.1109/7260.915627.

[41] Hooi Been Lim, Nguyen Thi Tuyet Nhung, Er-Ping Li, and Nguyen Duc Thang. Confocal microwave imaging for breast cancer detection: Delay-multiply-and-sum image reconstruction algorithm. *Biomedical Engineering, IEEE Transactions on*, 55(6): 1697–1704, 2008. ISSN 0018-9294. doi: 10.1109/TBME.2008.919716.

[42] Hai Qi Liu, Wang-Ling Goh, L. Siek, Wei Meng Lim, and Yue Ping Zhang. A low-noise multi-ghz cmos multiloop ring oscillator with coarse and fine frequency tuning. *Very Large Scale Integration (VLSI) Systems, IEEE Transactions on*, 17(4):571–577, 2009. ISSN 1063-8210. doi: 10.1109/TVLSI.2008.2011206.

[43] P.M. Meaney, M.W. Fanning, Dun Li, Steven P. Poplack, and K.D. Paulsen. A clinical prototype for active microwave imaging of the breast. *Microwave Theory and Techniques, IEEE Transactions on*, 48(11):1841–1853, 2000. ISSN 0018-9480. doi: 10.1109/22.883861.

[44] P.M. Meaney, M.W. Fanning, T. Zhou, A. Golnabi, S.D. Geimer, and K.D. Paulsen. Clinical microwave breast imaging - 2d results and the evolution to 3d. In *Electromagnetics in Advanced Applications, 2009. ICEAA '09. International Conference on*, pages 881–884, 2009. doi: 10.1109/ICEAA.2009.5297356.

[45] J. S. Michaelson, M. Silverstein, Wyatt J., G. Weber, R. Moore, E. Halpern, D.B. Kopans, and K. Hughes. Predicting the survival of patients with breast carcinoma using tumor size. *J Cancer*, Aug 2002.

[46] Sharyl J. Nass, I. Craig Henderson, and Joyce C. Lashof. *Mammography and beyond: developing technologies for the early detection of breast cancer*. National Cancer Policy Board, Institute of Medicine, Division of Earth and Life Studies, National Research Council, 2001.

[47] N.K. Nikolova. Microwave imaging for breast cancer. *Microwave Magazine, IEEE*, 12 (7):78–94, 2011. ISSN 1527-3342. doi: 10.1109/MMM.2011.942702.

[48] W. H. Parson. *Cancer of the Breast*. Springfield,IL:Thomas, 1959.

[49] B. Razavi. Design considerations for direct-conversion receivers. *Circuits and Systems II: Analog and Digital Signal Processing, IEEE Transactions on*, 44(6):428–435, 1997. ISSN 1057-7130. doi: 10.1109/82.592569.

[50] T. Rubaek and V. Zhurbenko. Prototype of microwave imaging system for breast-cancer screening. In *Antenna Technology and Applied Electromagnetics and the Canadian Radio Science Meeting, 2009. ANTEM/URSI 2009. 13th International Symposium on*, pages 1–4, 2009. doi: 10.1109/ANTEMURSI.2009.4805106.

[51] T. Rubaek and V. Zhurbenko. Phantom experiments with a microwave imaging system for breast-cancer screening. In *Antennas and Propagation, 2009. EuCAP 2009. 3rd European Conference on*, pages 2950–2954, 2009.

[52] M.A. Shahira Banu, S. Vanaja, and S. Poonguzhali. Uwb microwave detection of breast cancer using sar. In *Energy Efficient Technologies for Sustainability (ICEETS), 2013 International Conference on*, pages 113–118, 2013. doi: 10.1109/ICEETS.2013.6533366.

[53] Merrill I. Skolnik. *Radar Handbook*. Mc Graw Hill, 1990.

[54] S.G. Tanyer. High-resolution radar in inhomogeneous media. In *Signal Processing Proceedings, 1998. ICSP '98. 1998 Fourth International Conference on*, pages 381–384 vol.1, 1998. doi: 10.1109/ICOSP.1998.770231.

[55] M. Tiebout. A cmos direct injection-locked oscillator topology as high-frequency low-power frequency divider. *Solid-State Circuits, IEEE Journal of*, 39(7):1170–1174, 2004. ISSN 0018-9200. doi: 10.1109/JSSC.2004.829937.

[56] S.D. Toso, A. Bevilacqua, A. Gerosa, and A. Neviani. A thorough analysis of the tank quality factor in lc oscillators with switched capacitor banks. In *Circuits and Systems (ISCAS), Proceedings of 2010 IEEE International Symposium on*, pages 1903–1906, 2010. doi: 10.1109/ISCAS.2010.5537949.

[57] S.D. Toso, A. Bevilacqua, M. Tiebout, N. Da Dalt, A. Gerosa, and A. Neviani. An integrated divide-by-two direct injection-locking frequency divider for bands s through k_u. *Microwave Theory and Techniques, IEEE Transactions on*, 58(7):1686–1695, 2010. ISSN 0018-9480. doi: 10.1109/TMTT.2010.2049680.

[58] S.D. Toso, A. Bevilacqua, M. Tiebout, N. Da Dalt, A. Gerosa, and A. Neviani. A 0.06 mm2 11mw local oscillator for the gsm standard in 65 nm cmos. *Solid-State Circuits, IEEE Journal of*, 45(7):1295–1304, 2010. ISSN 0018-9200. doi: 10.1109/JSSC.2010.2049457.

[59] Stefano Dal Toso. *Analysis and Design of Injection-Locked Building Blocks for RF Frequency Generation in Ultra-Scaled CMOS Technologies*. PhD thesis, University of Padova, Italy, 2010.

[60] A. Vallese, A. Bevilacqua, C. Sandner, M. Tiebout, A. Gerosa, and A. Neviani. Analysis and design of an integrated notch filter for the rejection of interference in uwb systems. *Solid-State Circuits, IEEE Journal of*, 44(2):331–343, 2009. ISSN 0018-9200. doi: 10.1109/JSSC.2008.2010984.

[61] C.S. Vaucher, I. Ferencic, M. Locher, S. Sedvallson, U. Voegeli, and Zhenhua Wang. A family of low-power truly modular programmable dividers in standard 0.35-/spl mu/m cmos technology. *Solid-State Circuits, IEEE Journal of*, 35(7):1039–1045, 2000. ISSN 0018-9200. doi: 10.1109/4.848214.

[62] Donald R. Wehner. *High-Resolution Radar*. Artech House Publishers, 1994.

[63] J. Wernehag and H. Sjoland. A 24ghz automotive radar transmitter with digital beam steering in 130nm cmos. In *Research in Microelectronics and Electronics 2006, Ph. D.*, pages 481–484, 2006. doi: 10.1109/RME.2006.1689998.

[64] T. Williams, E.C. Fear, and D.W. Westwick. Tissue sensing adaptive radar for breast cancer detection: investigations of reflections from the skin. In *Antennas and Propagation Society International Symposium, 2004. IEEE*, volume 3, pages 2436–2439 Vol.3, 2004. doi: 10.1109/APS.2004.1331865.

[65] D.W. Winters, B.D. Van Veen, and S.C. Hagness. Uwb microwave imaging for breast cancer detection: an algorithm for estimating the breast surface. In *Antennas and Propagation Society International Symposium 2006, IEEE*, pages 267–270, 2006. doi: 10.1109/APS.2006.1710507.

[66] Rong Wu, K.A.A. Makinwa, and J.H. Huijsing. A chopper current-feedback instrumentation amplifier with a 1 mhz 1/f noise corner and an ac-coupled ripple reduction loop. *Solid-State Circuits, IEEE Journal of*, 44(12):3232–3243, 2009. ISSN 0018-9200. doi: 10.1109/JSSC.2009.2032710.

[67] Lei Yan, V. Krozer, S. Delcourt, V. Zhurbenko, T.K. Johansen, and C. Jiang. Gaas wideband low noise amplifier design for breast cancer detection system. In *Microwave Conference, 2009. APMC 2009. Asia Pacific*, pages 357–360, 2009. doi: 10.1109/APMC.2009.5385381.